SANDIA REPORT

SAND2004-3405
Unlimited Release
Printed August 2004

SENSOR FUSION FOR INTELLIGENT PROCESS CONTROL

Mehran Arbab, Bruce W. Binion, John J. Connors, Craig Dodge,
Mark A. DeYoung, Arthur R. Farrar, Craig P. Gowin, William F. Haley,
David Hanekamp, Kevin Hill, Yu Jiao, Raymond M. Mayer, Richard W. Michael,
Alan J. Miller, Michael R. Stokes, Rajiv Tiwary, Padmabhushana R. Desam,
Philip J. Smith, Lee A. Bertram, Robert J. Gallagher, Robert G. Hillaire,
William G. Houf, Donald A. Sheaffer, Jr., and Peter M. Walsh

Approved for public release; further dissemination unlimited.

⊞ **Sandia National Laboratories**

2

SANDIA REPORT

SENSOR FUSION FOR INTELLIGENT PROCESS CONTROL

Mehran Arbab, Bruce W. Binion, John J. Connors, Craig Dodge,
Mark A. DeYoung, Arthur R. Farrar, Craig P. Gowin, William F. Haley,
David Hanekamp, Kevin Hill, Yu Jiao, Raymond M. Mayer, Richard W. Michael,
Alan J. Miller, Michael R. Stokes, and Rajiv Tiwary
PPG Industries, Inc.
Mt. Zion, IL, Pittsburgh, PA, and Wichita Falls, TX

Padmabhushana R. Desam and Philip J. Smith
The University of Utah
Salt Lake City, UT

Lee A. Bertram, Robert J. Gallagher, Robert G. Hillaire,
William G. Houf, Donald A. Sheaffer, Jr., and Peter M. Walsh
Sandia National Laboratories
Livermore, CA

ABSTRACT

An integrated system for the fusion of product and process sensors and controls for production of flat glass was envisioned, having as its objective the maximization of throughput and product quality subject to emission limits, furnace refractory wear, and other constraints. Although the project was prematurely terminated, stopping the work short of its goal, the tasks that were completed show the value of the approach and objectives. Though the demonstration was to have been done on a flat glass production line, the approach is applicable to control of production in the other sectors of the glass industry. Furthermore, the system architecture is also applicable in other industries utilizing processes in which product uniformity is determined by ability to control feed composition, mixing, heating and cooling, chemical reactions, and physical processes such as distillation, crystallization, drying, etc.

The first phase of the project, with Visteon Automotive Systems as industrial partner, was focused on simulation and control of the glass annealing lehr. That work produced the analysis and computer code that provide the foundation for model-based control of annealing lehrs during steady state operation and through color and thickness

changes. In the second phase of the work, with PPG Industries as the industrial partner, the emphasis was on control of temperature and combustion stoichiometry in the melting furnace, to provide a wider operating window, improve product yield, and increase energy efficiency. A program of experiments with the furnace, CFD modeling and simulation, flow measurements, and sensor fusion was undertaken to provide the experimental and theoretical basis for an integrated, model-based control system utilizing the new infrastructure installed at the demonstration site for the purpose. In spite of the fact that the project was terminated during the first year of the second phase of the work, the results of these first steps toward implementation of model-based control were sufficient to demonstrate the value of the approach to improving the productivity of glass manufacture.

End-to-End Control System Infrastructure

Equipment and software were acquired to implement end-to-end hierarchical control on Line 2 at PPG's Mt. Zion, IL plant, from the batch house to the ware room. The portions of the system controlling combustion and crown temperature were installed, brought on line, and performed as expected. The frequency of unexpected excursions in crown temperature was reduced to near zero. The means to integrate glass quality measures with production control are to be implemented in the near future. The results of the work described below are components of the control system to be developed using the infrastructure now in place.

NO_X Control Experiments

At plants in locations where emissions limits are low, NO_X formation can become the principal factor limiting glass production, especially of highly-colored automotive products having poor transmission of infrared radiation through the molten glass and requiring high furnace temperatures. The response of NO_X to furnace conditions and behavior of the existing NO_X control system were investigated in a series of experiments in the production furnace. Open loop tests showed that the variability in NO_X sensor output due to sensor noise and other process controls was generally small. Static changes in control value determined the extent of control that is possible using the present control strategy. The NO_X production time constant, gain, and transport delay were measured. Port-to-port changes in air-to-gas ratio identified the ports whose stoichiometric ratios have the greatest influence on NO_X emission. Finally, by changing the NO_X control variable midway through a firing cycle, the dynamics between the control variable and NO_X response were determined.

Control loop interactions and sensor dynamics were identified that were not previously known, or had not been well understood, prior to the tests. Interaction was observed between the NO_X and furnace pressure control loops. An anomalous peak in NO_X was seen during the reversal from right firing to left firing. The NO_X control loop exhibited a different transport delay during the steady portion of the reversal cycle than at the start of the cycle. It is believed that some of these effects and other undesirable

characteristics of the control system can be explained by differing responses of the continuous emission monitor to abrupt changes in exhaust gas flow rate and composition. As a result of this work, similar NO_x tests can be performed for other glasses in a much shorter time. The results suggested possible improvements in the NO_x control system that should be pursued in the near-term and more complex approaches that might be incorporated in the system to be based on the combustion model, whose development is described below.

Furnace Simulation for Model-Based Control

The ultimate goals of the furnace simulation are to provide the basis for model-based control of combustion space and glass conditions, fundamental understanding of process behavior, identification of control variables and their parameters (gains), and a tool that will assist in the evolution and evaluation of furnace designs. In the phase of the work that was completed, the objectives were: 1. to use Computational Fluid Dynamics (CFD) simulations to understand port-to-port interaction of the flows in the glass furnace, and 2. to identify and make recommendations regarding the experimental data that would be most useful for model validation. Since few experimental measurements were available from inside the PPG Line 14-2 furnace, an existing database (Newbold et al., 1997) was chosen to address the first objective. The furnace examined by Newbold and coworkers was a side-port, regenerative, flat glass furnace similar to the PPG furnace chosen for the present study. Three separate simulations and an extensive sensitivity analysis were performed:

1. A single-port simulation to compare the velocity, temperature, and species concentration fields with the experimental data.

2. A three-port simulation to identify the influence of nearest neighbor ports on the middle port.

3. A full furnace simulation to identify the influence of all other ports on a single port.

4. A sensitivity study to identify the influence of:

    a. Glass surface temperature boundary conditions on the burner plane and on the whole domain.

    b. Inlet air flow rates on the gas velocity, temperature and major species concentration distributions in the furnace.

    c. Inlet air velocity profiles on the gas velocity, temperature, and major species concentration distributions in the furnace.

    d. Computational resolution of mixing in a port neck on gas velocity, temperature, and major species concentration distributions in the furnace.

    e. The crown temperature profile on properties in the burner plane and on the whole furnace domain.

The three different glass furnace models were chosen to establish the effects of boundary conditions and port-to-port interactions. All three models produced similar results for all variables in the region from a distance of about one meter above the glass surface to the crown. However, in the flame region, where the gradients in scalar properties are steep, the simulation results were sensitive to mesh resolution and to conditions such as inlet air flow rates. Gas velocity distributions and, in some cases, the gaseous species concentrations, were calculated by the models with good accuracy, but the simulations were not able to reproduce the temperature measurements or the species concentrations, in most cases. The simulations did successfully establish that port-to-port interactions have only minimal influence on flame chemistry, but a significant effect on exhaust gas flow rates.

In order to obtain reliable predictions of temperature and major species under all conditions and at all locations in the flames and furnace, the following combination of experimental measurements and improvements to the calculations was proposed:

1. Port-by-port air and fuel flow rates and velocity and temperature distributions in the combustion air at the inlets should be measured with good accuracy.

2. An accurate mean glass surface temperature, the crown temperature, and the crown refractory emissivity should be obtained.

3. Mixing should be resolved more accurately in the near burner region, which acts as a boundary condition for the full furnace model, in order to capture port-to-port interactions.

4. Large eddy simulations to resolve more physics in the flames.

5. For NO_x model validation, measurements of NO_x concentrations in the combustion space and, preferably, within the flames, along with measurements of the inlet and boundary conditions described above.

Fusion of Temperature Measurements for Furnace Control

Rider arch temperatures were proposed as attractive candidates for monitoring of conditions in the furnace and regenerators. The behavior of rider arch temperatures can be monitored with little effort, and great stability, by imposing a template such as an exponential fit, or an even better approximation in the form of a wavelet, extracting and tracking average values over whole cycles, and monitoring incoming data for departure from the predictive template. Fusion of sensor output in this way can stabilize control loops that have used single-input signals and are thus vulnerable to outliers in the data. The template can reject outliers with great confidence. The proposed exponential template for the time dependence of the rider arch temperatures would achieve a 2500:1 compression of the temperature data and produce output whose significance could be immediately interpreted and acted upon by the control system or engineers, depending upon the nature of the disturbance.

Modeling and Control of Annealing Lehrs

A fully coupled 3-dimensional model of heat transfer in a float glass annealing lehr was developed. The model executes rapidly on a small computer workstation and has practical application for use by process engineers in determining optimum set points for annealing lehr operation. The model treats heat conduction and advection in the moving glass ribbon and considers the semitransparent nature of radiative heat transfer in the glass. It also accounts for mass flow of air and heat transfer in the cooling ducts and surface-to-surface radiative exchange between the exterior walls of the ducts and the glass ribbon. The model computes a complete energy balance on the lehr as part of each simulation.

Results show the effects of operating conditions on the glass temperature distribution in a typical lehr and illustrate the use of mathematical modeling to improve design, operation, and control. The model has also been used to perform inverse problems, where the changes in lehr operating conditions required to compensate for changes in lehr inlet glass temperature, load, and other perturbations, are computed. This capability, coupled with the model's fast execution on a small workstation indicates that it may be suitable for use in real-time model-based control of a float glass annealing lehr. As an alternative, a lehr temperature control algorithm based a rapid linear projection control scheme was developed and demonstrated by application to successful control of the lehr simulation model. The uniformity of the temperature of the glass ribbon at the exit from the lehr was controlled to the extent that a temperature difference of only 0.25 K (0.45 °F) existed between the centerline and edge at the center plane of the ribbon.

Conclusions

The implementation of end-to-end control was approached on various fronts and at several levels, as it must be if the goal of integrated control is to be reached in time to have the greatest possible benefit to industry. The various fronts and levels included: 1. installation of the requisite computers, equipment, and software, 2. basic flow measurements, 3. experimental definition of NO_X control system performance and the response of NO_X to process variables, 4. a proposal for fusion of temperature sensors to achieve a robust indicator of the state of the furnace, 5. furnace simulations, including evaluation of alternative approaches and sensitivity, and 6. annealing lehr simulation, including development and testing of an annealing lehr control algorithm. This work, along with additional modeling and simulation of the furnace by the University of Utah and analysis of forming and heat transfer in the tin bath by PPG Industries, will provide the foundation for model-based control of three of the most important processes in glass manufacturing: combustion, forming, and annealing. At the same time that these longer-range objectives were being pursued, the shorter-range objectives of improvement in control of furnace temperature, combustion stoichiometry, and NO_X were approached through their individual control loops. That work resulted in immediate improvements in performance and provided valuable data to be used in the development of the model-based control system.

ACKNOWLEDGMENTS

DEDICATION

We dedicate this work to the memory of our colleague and friend, Lee A. Bertram, the member of the team who had the fullest understanding of what needed to be done to realize the goals of the project and make a lasting contribution to the advancement of continuous process industries in the United States.

CONTENTS

CONTENTS (continued)

CONTENTS (continued)

1. INTRODUCTION

To remain competitive in today's market, U.S. manufacturers must continue to increase utilization of energy and raw materials, maximize the productivity of labor and capital, minimize pollutant emissions and waste, and improve product uniformity. As progress is made in each of these areas, further improvement becomes increasingly difficult. The Technology Vision Statements and Roadmaps drawn by the participants in the Industries of the Future Program reflect the belief that a promising route to continued improvement is through better manufacturing process control. The work undertaken in the present project was the development of the computer architecture that will integrate the information from on-line process and product quality sensors to achieve end-to-end digital control of production. The approach is well-suited for application to any industry in which raw materials are beneficiated or converted to finished products in complex multi-step processes having widely varying conditions, nonlinear behavior, and slow output response to changing input conditions.

Glass was the Industry of the Future chosen for the demonstration of the control system, not because the application to glass production was thought to be particularly simple or straightforward, but because the potential benefits to the glass industry were great, and because members of the team assembled for the project were specialists in measurement, modeling, and control of combustion, one of the critical processes in glass manufacturing. The original project team, led by Visteon Glass Systems, and the subsequent team led by PPG Industries, with Sandia National Laboratories and the University of Utah as partners, made significant progress toward end-to-end control of glass manufacturing. Although the collaborative project was terminated prematurely, ending the team's work far short of its ultimate goal, implementation of advanced control systems by PPG Industries on its float glass production lines will, of course, continue. The objective is a hierarchy of control software managing a combination of existing feedback loops, high level product quality parameter measurement systems, and stand-alone sensors whose output has traditionally been interpreted and acted upon by expert human operators.

The control system envisioned is new and innovative in spanning the full range and length of the production facility, from the input of raw and recycled materials to the output end of the production line. In many float glass manufacturing plants, this span is covered by independent, non-communicating sets of sensors and control subsystems, including human operators stationed at the furnace, the tweel, and the annealing lehr, along the glass production line. The tools with which these diverse sensor signals will be fused include correlation functions connecting inputs and outputs of subsystems (sometimes embodied in neural networks, as appropriate), expert systems for the capture of human skills, and physics-based high-fidelity digital simulations, when these are the

most cost-effective and robust tools with which to connect input and output. The approach is readily adaptable to manufacturing processes in other OIT Industries of the Future, who are operating under similar sets of conditions and constraints.

The beginning of the modern era in glass manufacturing process control might well be identified with the 1973 symposium, Automatic Control in Glass, organized by Raymond J. Mouly of PPG Industries on behalf of the International Federation of Automatic Control (Mouly, 1973). Application of control theory in glass production has been discussed by Staahl et al. (1977), Farmer et al. (1992), Bauer et al. (1996, 1998), Pirovolou et al. (1996), Smith et al. (1996), Carvalho et al. (1998), Huber (1998), and Koenig (1998, 1999). Implementation, to date, has been limited to control of a subset of the parameters influencing glass quality, without input from quality indicators themselves. A review of this work is given by Carvalho et al. (1998). Farmer et al. (1992) installed a video viewing system in the combustion space of a 100 ton/day container glass tank and used a knowledge-based controller for heat input, air/fuel ratio, and the firing rates of individual burners. Kimura et al. (1996) and Nakagawa et al. (1996) processed video images of batch coverage to control firing rate and tank bottom temperature. Bauer et al. (1996) developed a control system for an 80 ton/day soda-lime glass melting tank, incorporating a detailed three-dimensional physical simulation, a reduced-order model, and an adaptive neuro-fuzzy inference system which was capable of optimizing color and other set point changes. Duffus (1996), at PPG Industries, developed a model-based controller using canal temperature, refiner pressure, glass level, lehr speed, and glass ribbon width and thickness at the exit from the tin bath to control the tweel opening and maintain the desired production rate from a float glass tank. Heitor and Correia (1996) used flame images to control fuel oil spray quality and pollutant emissions from a 38 ton/day regenerative, end-fired, soda-lime glass furnace. The proposed system was a major advance over previous work, in its connection of product defects to process conditions and consideration of a wider range of impacts on operating and maintenance costs.

A simplified schematic diagram of a flat glass production line and the proposed control system are shown in Figure 1-1. The objective of the present project was the linkage of glass quality to batch preparation, melting, fining, conditioning, forming, and annealing processes, and the reduction of defects arising from less-than-optimum control of glass composition, combustion space atmosphere, temperatures, melt circulation, oxidation/reduction state, viscosity, and thickness. Batch preparation, melting, fining, conditioning, forming, and annealing are basic operations found in other sectors of the glass industry, so the principal features of the control system are applicable, with straightforward changes in product quality criteria, to containers, fiber glass, and some specialty glass products.

An integrated system was to be assembled, in which the information gathered by sensors is linked through a dynamic simulation to control of the process conditions. The inputs are derived from conventional sensors and from prototype and advanced sensors where needed. No single control methodology is expected to be able to cope with the

Melting Furnace **Tin Bath** **Annealing Lehr**

Batch
Feed
Product

Fuel and Air Flows
Bottom Temperatures
Crown Temperatures
Bubble Flowrate
Stirrer Speed
Tweel Position
Glass Temperature
Heat Input
Glass Thickness
Blowers
Pyrometers
Line Scanner
Stress Analyzer
Distortion Analyzer
Defect Analyzer

Distributed Regulatory Control Layer - Parallel Operation

Product Quality Sensors

Advanced Control Layer
Multivariable Model Predictive Control
Neural Network Nonlinear Mapping
Reduced Order Analytical Models

Empirical Models and Models Based on First Principles

Supervisory Control and Scheduling Layer

Figure 1-1. Distributed and hierarchical control of flat glass production
(control scheme by D. A. Sheaffer, Jr., Sandia National Labs., 1998;
float glass line schematic after P. Sewell, 1997).

entire range of challenges presented by this complex manufacturing process, which has long dead times, is multivariable, and nonlinear. The methodology found to be most appropriate in each part of the process should be applied there and integrated with the rest of the system. The hierarchical control system envisioned has three layers: (1) distributed parallel regulatory controllers, (2) advanced model-based and neural network controllers, and (3) supervisory control and scheduling. The plan was to treat each of the major sections of the production line in turn. The first phase of the work, by Visteon and Sandia, was focused on the annealing lehr. The second phase of the work, by PPG, the University of Utah, and Sandia, was focused on the melting furnace. The purpose of the present section is to describe the structure of the end-to-end control system that was the ultimate goal, to provide the context for the work that was done, before the project was prematurely terminated.

Distributed System of Regulatory Controls

The distributed control system has two important functions, data acquisition and regulatory control. The sensors and actuators indicated in Figure 1-1 by the vertical lines below the melting tank (which, in the figure, includes the refining zone and working

end), tin bath, and annealing lehr are directly connected to regulatory controls, typically proportional, integral, and derivative (PID) controllers. The data from the sensors and actuators is first collected in localized computer systems near the measurement points and used for localized feedback control strategies, then sent on to the advanced control and process simulation systems where all the data are fused together and used as input to the model-based control algorithm. The data log allows the control and modeling experts to observe statistical trends in the data over time. This information is also needed for development of the empirical models used in the portion of the system shown underneath the product sensors in Figure 1-1. Regulatory controls are used for inner loop high speed dynamic control, where the dynamics of the process are well understood. These controllers execute at high sample rates giving them the ability to reject high frequency disturbances. They linearize the process variables, easing the way for implementation of high level advanced control algorithms.

Advanced Model-Based, Neural Network, and Fuzzy Logic Controls

The advanced control layer utilizes the methods of multivariable model predictive control based on analytical nonlinear modeling, which does a good job of dealing with process interactions, constraints, dead time, and other control problems. Built into the controller are dynamic models, developed using data obtained during normal operation and during step tests, for the effects of all of the manipulated variables and measured disturbance variables. The controller makes moves in a feed forward fashion. Feedback is proportional to the difference between the value of a process variable predicted by the model and the actual value. If the model prediction and actual value are in agreement, then there is no feedback. This feed forward attribute is important for controlling processes with large amounts of dead time. A traditional feedback control system (e.g. PID) waits until defects are observed in the product to make changes in manipulated variables. The model-based controller, on the other hand, anticipates the appearance of defects and moves to prevent their occurrence.

Where processes are found to be highly nonlinear, and the computations using analytical models would be too slow, neural networks are used to compute the input/output relationships for real-time control. An advantage of having a neural network perform the nonlinear mapping is that it can be trained, tested, and verified off-line. Once trained and tested, neural networks are computationally efficient. The feed forward neural network algorithm can be run in real time with advanced control algorithms using standard computer resources. However, it is important to test the neural network over the entire multidimensional mapping space, to guarantee that the output is always predictable and stable.

The advanced control layer uses inputs from the hot end regulatory control systems, as well as statistical information from the sensors recording defects at the end of the production line. There is a good opportunity here to take advantage of the properties of fuzzy inference functions to combine the various measures of distortion, stress, defects, and optical properties of the glass. The advanced controller and supervisory

control blocks can then apply these measures of quality in evaluating the performance of the control system.

Supervisory Control and Scheduling Block

The highest layer in the control system is the supervisory control and scheduling block. The supervisory control section takes inputs from all components of the distributed control system. One of its purposes is to allow experts to monitor operational trends over time. Feedback to the system from this layer requires human intervention. A collection of plotting and graphics tools in the control room and engineers' offices provides visual aids with which to analyze trends in furnace performance.

Role and Importance of High Fidelity Simulations

The performance goals driving the implementation of advanced control systems include improved energy efficiency, improved productivity, longer furnace campaigns, and the reduction of combustion-generated pollutants. Since satisfaction of these constraints often leads to conflicting conclusions regarding the operation of the plant, it is important to have accurate glass melting, forming, and annealing models. Models serve several important functions: (1) they are an efficient means for developing and testing control algorithms and determining the optimum placement of sensors, serving as a cost-effective substitute for the real system, (2) they allow one to map a greater region of the parameter space than would be possible in actual tests on real furnaces because of the high cost of the production that would be lost during tests under extreme conditions, (3) simulation linked with closed-loop control is a powerful tool for the optimization of furnace performance, and (4) as computing power increases, more and more detailed and accurate models will be used in model-predictive control.

2. INDUSTRY PERSPECTIVE

Raymond M. Mayer
Glass Technology Center
PPG Industries, Inc., Pittsburgh, PA

The goal of the *Sensor Fusion for Intelligent Process Control* project is to integrate many individual Single In/Single Out control loops into a system of advanced process control, which allows not only control, but also optimization of a process. In continuous process industries, the task of controlling a process from end to end is an expensive multi-year endeavor and beyond the scope of a single project's timetable and funding. However, the development of a combustion control scheme represents an important step toward that goal. To have cross-industry applicability, we need to demonstrate the ability to interface a model-based control scheme and resulting supervisory level control algorithm to a process with a number of independent control loops. We do not believe the choice of a specific focus area is as important as the knowledge and experience to be gained from attempting to develop supervisory level control based upon a highly complex first principles model.

As background, PPG uses computer equipment from two different suppliers to control the glass melting and forming operations. All ten of its glass production lines utilize similar control schemes based upon our understanding of the process and operations. This understanding is, in turn, based upon physical and mathematical modeling and our empirical knowledge of glass-making processes. Yields are generally stable and are affected most by product mix. The largest losses are from Trim and Layout, Defects, Thickness and Width Changes, and Mechanical Downtime.

The structure of PPG's process control is based upon the four-tier system depicted in Table 2-1. Development of process control systems has been focused on melting, annealing, and ware room operations. Tier 2 and 3 control systems for the float bath are currently in development. Most of the Tier 2 work is by its nature process and equipment specific. We believe, as others do, that process control technology is a source of competitive advantage and hold it to be highly proprietary.

Table 2-1. PPG Industries' Process Control Scheme.

Tier 4 (*Future*)	Business System and Database Information Rule-Based Control	Multiple In/Multiple Out
Tier 3	Supervisory or Model-Based Control	Multiple In/Single Out
Tier 2	Process Variable Control	Single In/Single Out
Tier 1	Sensor Measurement and Machine Control	Single In/Single Out

Refinement of existing control algorithms and completion of the float bath Tier 2 and 3 control systems is thought to be worth an additional 2-3% in yield, *a major achievement in a commodity industry like glass*. However, other gains in energy efficiency, furnace life, scheduling flexibility, and quality improvement could also be realized through the development of additional Tier 3 and 4 systems. We, therefore, proposed that we focus on the development of a Tier 3 system for temperature control in the melter that would interact with existing Tier 2 and 3 control algorithms, thus allowing transfer of these algorithms without disclosure of existing proprietary technology.

The Tier 3 melter control system requires development of a first principles-based mathematical model, the verification of the model via new sensors, and the integration of this model with existing control loops. The particular plant location was selected because it requires a constrained optimization of combustion parameters to maximize throughput while meeting NO_x emission requirements. Time constants in the combustion process are more than three orders of magnitude smaller than they are in the melter convective flow system, which makes this an extremely interesting optimization problem.

We believe that this project is typical of what other manufacturers in the glass industry, as well as other industries will face in moving from control to optimization. The specific process parameters and optimization criteria will vary by manufacturer and industry, but the process of developing supervisory control based upon a first principles model will be applicable to all. Completion of this project will move us one step closer to the ultimate goal of end-to-end process control.

3. CORRELATION WITH INDUSTRIES OF THE FUTURE ROADMAPS

All of the available Industry Vision Statements and Roadmaps consider large scale integrated process control to be a high priority. The sensors for process conditions and product quality are quite different from one industry to another, as are the physical models for the individual processes that will provide the basis for model-predictive control. However, the architecture of the control system and its software components are generic and adaptable to hierarchical control of a wide range of types of manufacturing processes. A control system should be able to accept inputs from sensors and distributed control system components supplied by all equipment manufacturers.

Aluminum

The *Aluminum Industry Technology Roadmap* (Aluminum Association, 1997, p. 8) says: "The inability to accurately model, measure, and control many key parameters and phenomena during refining and smelting presents a significant barrier to several of the performance targets, particularly improved Bayer process productivity and improved reduction cell performance." Removal of the inability to accurately control such processes was an objective of the present project.

Chemicals

The *Technology Vision of the U.S. Chemical Industry* (American Chemical Society et al., 1996) contains an extensive discussion of the importance of improvements in process control to that industry. The following statement is typical (p. 68):

"Advanced process control technology can be developed to handle the full operating range of a plant, from start-up to shut-down. Advanced control can run all the time to ensure meeting product specifications all the time. The plant must be able to eliminate as many process disturbances as possible and to handle the nonlinear behavior of process units. Advanced process control technologies can continue to develop until very specialized methods typically associated with off-line use become on-line parts of everyday operation. These techniques will enable plants to run optimally."

This is virtually a summary of the requirements and objectives for the advanced control system envisioned under the present project. Especially pertinent is the statement in the next-to-last sentence, to the effect that methods now associated with off-line operation will become part of the real-time control system.

At a workshop convened by the National Science Foundation and the National Institute of Standards and Technology (NSF/NIST, 1998), representatives of the chemical industry and the chemical engineering research community developed a roadmap exclusively devoted to process measurement and control. A section entitled, "Needs and Challenges," (p. 3) opens with the following statement: "The potential for improved operational performance offered by the integration of measurement, control, and information systems needs to be exploited to maintain and improve the competitiveness of the U.S. chemical industry." It is exactly this feature, i.e. integration, which was the central objective of the present work.

Forest Products

One of the six task groups that contributed to *Agenda 2020 - The Path Forward - An Implementation Plan* (American Forest & Paper Association, 1999), the technology vision and research agenda for America's forest, wood, and paper industry, was charged with identifying industry needs in sensors and controls. In the table prepared by the Sensors and Controls Task Group outlining the pathway for addressing needs related to measurement and diagnostics (p. 27) is the entry: "The complexity of processes and the need for maximum efficiency and low cost require the need for ever-increasingly sophisticated real-time measurement and control systems." The table of needs related to control system effectiveness (p. 29) calls for a number of the advances anticipated by the present project: "mill-wide control optimization, multi-variable and non-linear control, self-regulating and adaptive control systems, and process variability minimized or eliminated."

Glass

At the Glass Technology Roadmap Workshop held in Alexandria, VA, on April 24-25, 1997, experts from the glass industry and related organizations identified the research priorities emphasized in the Roadmap that outlines the strategy for achieving the goals specified in the Industry Vision Statement, *Glass: A Clear Vision for a Bright Future*. In the Executive Summary of the Report of the Workshop (Eisenhauer et al., 1997), Exhibit 1-2 summarizes near-, mid-, and long-term research needs for the industry. In the mid-term (3 to 10 year) time frame, under the heading "Production Efficiency," there are only two entries: (1) Develop intelligent control of production and fabrication processes and (2) Develop integrated process control strategies. In Chapter 3, containing the report from the Production Efficiency Work Group, is the following: "The lack of effective in-process sensors and control systems is the most serious barrier to better production efficiency. Accurate process control is the most effective way to optimize production within existing furnaces and production lines." Exhibit 3-2 in the Report (p. 13), entitled: "Technology Barriers to Achieving Production Efficiency Goals," contains the entry, "Lack of better in-process sensors and process control systems," underlined by 5 bullets, indicating its relative importance compared with the other items in the table, none of which has more than 2 bullets.

At the summary session of the Roadmap Workshop, a set of research needs was identified that had emerged as important in all of the Work Groups and common to all segments of the glass industry. Among these were (Eisenhauer et al., 1997, p. 54): (1) Improve defect detection, measurement, and control, and (2) Design intelligent model-based control and process optimization systems. There is no question that the glass industry considers the improvement of process control to be one of its highest priorities. The model-based control system advocated in the first research need is exactly the approach that was adopted in the present project.

Metal Casting

The Metal Casting Industry Technology Roadmap (Cast Metal Coalition, 1998) identified its industry's high priority research needs in Exhibit 1-1 (p. 3). Under the heading, "Manufacturing," are these objectives: "Develop smart controls and sensors for automation supervision," "Develop a systems approach to scheduling and tracking," and "Develop a mathematical model that describes process control and can control the machine." The smart controls, systems approach, and mathematical control scheme are all objectives of the present work.

Mining

The Mineral Processing Technology Roadmap of the Mining Industry of the Future (National Mining Association and U.S. DOE, 2000) outlines some of the most exciting opportunities for control of any of the industries of the future (p. 11):

"Improvements in process design and control offer opportunities for large energy and cost savings in the mining industry. Improved sensors, systems, and empirical models can allow the industry to exert more control over processes and increase the unit capacity and extend the operating range of existing equipment.

"Industry hopes that improvements in sensor analysis systems and automation of critical decisions will reduce the cost of system design by 90 percent over the long term. This will not only allow industry to better utilize existing systems, it will help them to integrate and prove advanced design systems in physical separation activities.

An important point here, and the aspect that connects the mining industry application to the work in progress at PPG, Sandia, and the University of Utah, is the emphasis on improving the performance of existing equipment, i.e. introducing hierarchical control utilizing sensors already in place, adding new sensors where needed at critical points, and without major new investment in capital equipment.

Petroleum

As one would expect, controls and advanced control systems figure prominently in the Technology Roadmap for the Petroleum Industry (U.S. DOE, 2000). Here, as in the other industries, the emphasis is on integration of existing information through supervisory, model-based, control. In a summary of the characteristics of the refinery of the future (p. 7) we find:

"Energy efficiency and process controls are integrated."
"Plants are tightly controlled, and rely on intelligent controls."

Simulation of heat transfer in petroleum process heaters is an area in which the University of Utah group has made valuable contributions to the industry.

Steel

The Steel Industry Technology Roadmap (American Iron and Steel Institute and Steel Manufacturers' Association, 1998) contains numerous references to the need for better controls. Sandia has developed non-contact sensors for refractory profiling, off-gas composition, and monitoring of metal surface temperature in basic oxygen furnaces. The following are some of the research and development needs listed under the heading, "Process Development," in the Steel Industry Roadmap: under Cokemaking - "Develop improved process control, including on-line data collection," "Develop plant simulations and sophisticated control algorithms;" under Ironmaking - "Develop control models for reduction, char control, foaming, and post combustion/heat transfer for smelting systems;" under Basic Oxygen Furnace Steelmaking - "Compare process parameters versus results of models for fluxing and oxygen blowing;" under Electric Arc Furnace Steelmaking - "Apply and evaluate artificial intelligence techniques for electric arc furnaces;" and under Rolling and Finishing - "Develop methods for effective communication of the interrelationship between end properties, production route, microstructure, and cost." These require an integrated, hierarchical control system such as the one envisioned in the present project.

4. NO$_X$ CONTROL EXPERIMENTS

Robert G. Hillaire,* David Hanekamp,† Yu Jiao,† and John J. Connors†

*Sandia National Laboratories
Livermore, CA

†Glass Technology Center
PPG Industries, Inc., Pittsburgh, PA

Introduction

NO$_X$ tests were performed to help characterize the NO$_X$ production process in the glass-melting furnace in Line 2 at PPG Industries', Mt. Zion, IL facility. This characterization exposed the process controls that affect NO$_X$ production and that will permit the design of a better control strategy to reduce NO$_X$ without reducing production throughput. Several precautions were taken to ensure that the experiments did not adversely affect glass quality, nor produce unacceptable levels of NO$_X$. The primary precaution was embedded in the design of the test itself; the control variables were manipulated to produce a static balance that ensured long-term stability. The process variables measured during the test were those typically measured during production and are available for feedback control. However, an ENERAC sensor was also used to verify data from other sensors.

The plan for the four tests that were conducted (Open Loop, Port-to-Port, Magnitude, and Trend) is located in Appendix B. The Open Loop test was used to determine how much process variation could be expected when no control variables are manipulated. The Port-to-Port test determined the sensitivity to gas distribution in each port compared to the overall NO$_X$ production. The Magnitude test provided a first order understanding of how much NO$_X$ could be affected by the combustion air-to-gas ratio. The Trend test revealed dynamic information about how NO$_X$ changed when the air-to-gas ratio was manipulated during a firing cycle. The tests exposed four things: (1) NO$_X$ is strongly related to the furnace air-to-gas ratio, (2) NO$_X$ production is linear with respect to air-to-gas ratio within the normal operating limits of the furnace, (3) Other control loops confound the NO$_X$ control loop, and (4) NO$_X$ is most sensitive to gas distribution to ports near the hottest part of the furnace.

Method

Test Precautions

The experiment was designed so the average process condition was maintained. During the test, a control variable might be set high for a few minutes, then set low for an equal amount of time, thus providing a balance between the high and low settings. For instance, if one part of an experiment produced more NO_x than is typical, the next part of the experiment was designed to produce less NO_x than typical, to maintain the usual average NO_x production.

If, under any of the conditions chosen, the average NO_x production had not been within acceptable limits, the experiment would have been terminated, redesigned, and continued at a later time. Similarly, if the melting process had started to produce unacceptable yield loss, glass defects (bubble, stone, color, transmittance), too high a crown temperature, or excessive furnace pressure, the experiment would have been terminated, redesigned, and continued later.

Control Variables

For satisfactory characterization of the process, significant process perturbations were necessary. In order to significantly perturb the process, the control variables needed to be changed by more than what is commonly done during production. For instance, the feedback controller can adjust the air-to-gas ratio by only a few percent. While this may be sufficient to stabilize the process during production, it was not enough to excite the process sufficiently to determine its dynamics.

Measured Process Variables

The process controls that affect NO_x also affect several other process variables. We needed to measure these other process variables to more completely understand the NO_x production process. The measured process variables were:

- NO_x
- Crown temperature (all crown thermocouples)
- Regenerator temperature (rider arch and regenerator crown thermocouples)
- Combustion air flow
- Port natural gas flows
- Melter pressure
- Furnace oxygen (existing oxygen sensors)
- ENERAC measurement at the center of connecting flue for NO_x and other parameters

Experiments

Four tests were conducted: Open Loop, Port-to-Port, Magnitude, and Trend. The Open Loop test was used to determine how much process variation could be expected when no control variables were manipulated. The Port-to-Port test determined the sensitivity to gas distribution to each port, compared to the overall NO_X production. The Magnitude test provided a first order understanding of how much NO_X could be affected by the furnace combustion air-to-gas ratio. The Trend test exposed dynamic information about how NO_X changes when the air-to-gas ratio was manipulated during a firing cycle.

Furnace Open Loop Control Test. This test indicated the amount of variance one could expect in the NO_X production when not changing any process controls. We simply set the controls at constant values and monitored the process for several cycles. This test is also known as the Cap Test or Furnace Off test.

Port-to-Port NO_X Source Identification Test. The objective of this test was to identify the individual port sensitivity to natural gas flow in relation to NO_X production. The hypothesis of this test was that a significant source of the NO_X generated in the furnace was from less than optimum fuel distribution and that the majority of NO_X was generated in the down-tank region of the furnace. To test this hypothesis and determine the potential for improvement of the gas distribution, we conducted the test as follows:

> Beginning with the downstream port on the left side, reduce the gas flow on each port by a fixed amount, one at a time, for one firing cycle. Then move upstream to the next port. Complete all of the left ports before moving to the right ports.

Magnitude test. The objective of this test was to verify the magnitude of NO_X production related to the current NO_X control scheme, for the purpose of future improvements to the NO_X control loop. This test showed how much the NO_X was affected by a static change in the control value. We were also able to determine to what extent the control settings from the previous firing and reversal influence NO_X production. The prescribed firing order allowed us to determine the effects of the previous cycle and the preceding two cycles in several combinations. The duration of the test was sufficiently long that parasitic perturbations in the process could be filtered out from the results.

The experimental procedure was simple. We alternated the NO_X control loop's output in a predefined pattern and maintained a constant control value for an entire firing cycle. Each firing cycle had either a "high" setting or "low" setting in a prescribed order. The prescribed order exercised several combinations of previous firing cycle conditions. To reduce the effects of confounding loop interactions, the Crown Temperature control loop was turned off and the total natural gas flow was fixed.

NO$_X$ Control Trend Test. The Trend test is often referred to, in the control world, as a Reaction Curve test. The objective was to verify the controllability of NO$_X$ using the existing control scheme. The test would determine if there were "irrevocable" process characteristics that cannot be manipulated after the firing sequence has begun (i.e. once the NO$_X$ production passes a certain level, it would not come back down during the present cycle regardless of changes in control). The test sequence also revealed non-linear effects in NO$_X$ production. The prescribed cycles exercised several combinations of conditions to expose not only the single cycle results, but also whether the firing conditions during the previous cycle affect NO$_X$ production.

The control setting for a firing cycle was either "high" or "low" at the beginning of the cycle, then at the halfway point in the cycle, the control setting was changed to its complement. The NO$_X$ control loop's output was changed in a predefined pattern. For this test, the Crown Temperature control loop and Melter Pressure control loop were in auto.

Results

The four NO$_X$ experiments were conducted on Line 14-2 during the week of March 25, 2002. The production line was producing Solex glass at its nominal rate and with various ribbon thicknesses during the week.

Open Loop Control Test

The experiment was conducted on March 28, 2002 from 08:10 to 10:07. The Crown A temperature control loop was in manual and the NO$_X$ control loop was in manual with the air-to-gas ratio fixed at its nominal value in each firing direction. Since the performance in the two firing directions is not exactly the same, the nominal air-to-gas ratios on the left and right sides of the furnace are different. The raw data from this experiment are shown in Figure 4-1, with the scales omitted in order not to disclose confidential information.

The analysis was performed on each firing cycle independently. The NO$_X$ data for individual firing cycles are shown superimposed in Figure 4-2. These individual firing cycle data were extracted from the raw data by first finding the lowest NO$_X$ point in a firing cycle then using the time corresponding to the lowest point as the starting point for the duration of the cycle. The valleys in the NO$_X$ record correspond to the periods when the gas is off, and the lowest points correspond to the times just before the gas is turned back on.

A first order transfer function, relating the air-to-gas ratio to the NO$_X$ production rate, was fit to each curve. Figure 4-3 shows two typical curve fits. The curve fitting routine was an Auto Regressive with Extra Input (ARX). The model for the curve fit was a first order transfer function with one pole and no zeros. The data transport delay was determined by comparing the rising edge in the gas flow rate to the rising edge in NO$_X$.
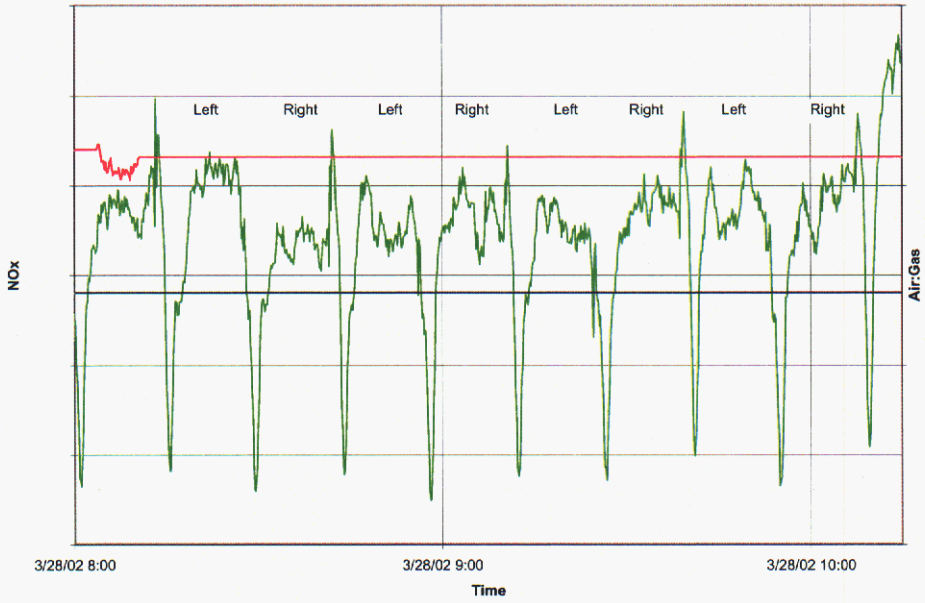
Figure 4-1. Open loop test results.
Green = NO$_X$. Pink = left air-to-gas ratio. Blue = right air-to-gas ratio.

Figure 4-2. Open loop extracted NO$_X$ curves. NO$_X$ versus time.

Measured Output and Simulated Model Output   Measured Output and Simulated Model Output

a. Typical right firing cycle.   b. Typical left firing cycle.

Figure 4-3. Open loop transfer function curve fit. NO_X versus time.

This transport delay was removed from the data before the fit. The resulting curves illustrate the exponential increase in NO_X (with gain and time constant). The gain correlates to the excess air-to-gas ratio, which was calculated from the total air-to-gas ratio by subtracting the stoichiometric air-to-gas ratio and air in-leakage from the total.

Port-to-Port NO_x Source Identification Test

This experiment was conducted on March 27, 2002 from 11:29 to 20:33. Figures 4-4, 4-5, and 4-6 show the raw data from the test. Again, as with all of the plots in this Section, the numerical scales have been removed in order not to disclose confidential information. Port-Right 6, begun at 12:03, was aborted because the control input was changed too late. This test cycle was repeated at 15:18. Port-Right 2, started at 13:51, was also aborted because the control input was changed too late. This test cycle was immediately rerun at 14:20.

During the preliminary analysis of the data collected on March 27, an anomaly was detected in Port-Left 3. The change in NO_X seemed to be too small for the amount of change in gas. The Port-Left 3 test cycle was rerun on March 28, 2002 starting at 10:07 (Figure 4-7). The initial conditions for this retest were different from those for the tests conducted on March 27. However, the analysis of these data (presented later in this section) will normalize the data to account for the differences.

The analysis was performed on each firing cycle independently. A first order transfer function, relating the port gas to the NO_X production rate, was fit to each curve. Figure 4-8 shows two typical curve fits. The curve fitting routine was, as for the open loop control test data, an Auto Regressive with Extra Input (ARX). The model for the

curve fit was a first order transfer function with one pole and no zeros. The data transport delay was determined by comparing the ris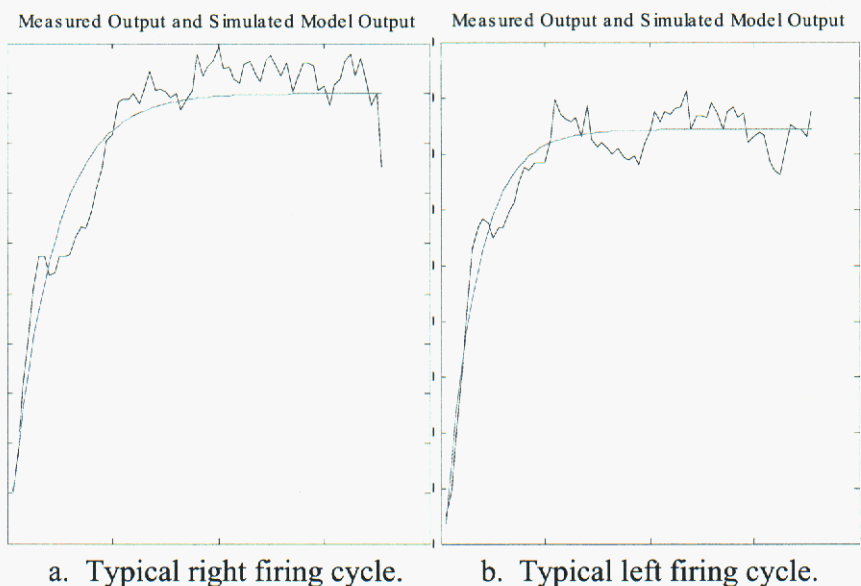ing edge in the gas flow rate to the rising edge in NO_X and was removed from the data before the fit. The resulting curves illustrate the exponential rise in NO_X with time through a firing cycle (with gain and time constant). The gain is correlated with the port gas flow rate.

Figure 4-4. Port-to-port NO_X source identification (11:00-14:00). Green = NO_X. Other traces can by identified by correlating their shifts with the port labels.

Figure 4-5. Port-to-port NO_X source identification (14:00-17:00). Green = NO_X. Other traces can by identified by correlating their shifts with the port labels.
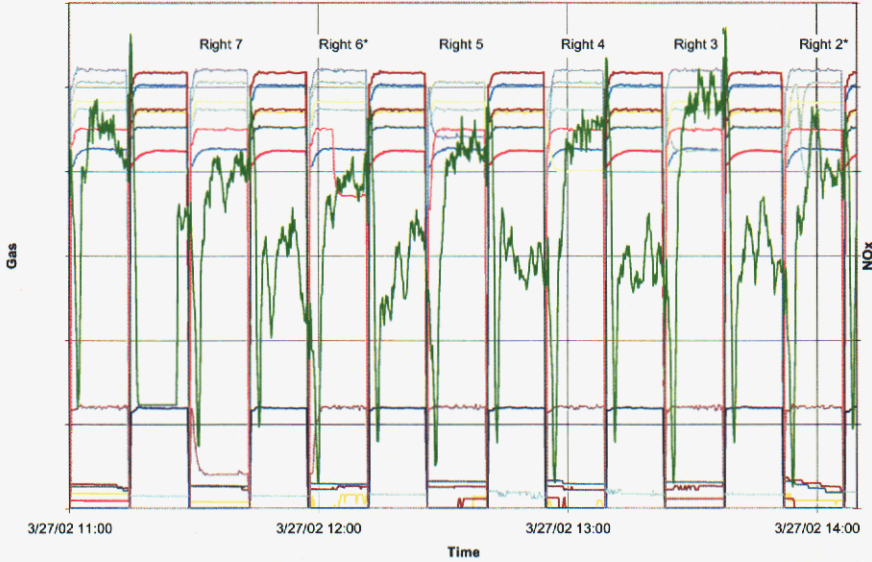
Figure 4-6. Port-to-port NO_X source identification (17:00-20:00). Green = NO_X. Other traces can be identified by correlating their shifts with the port labels.
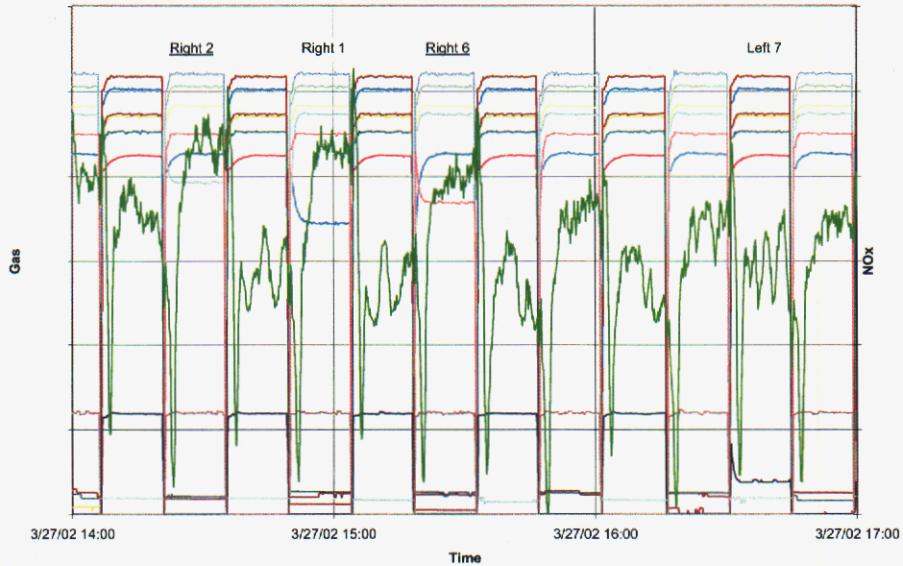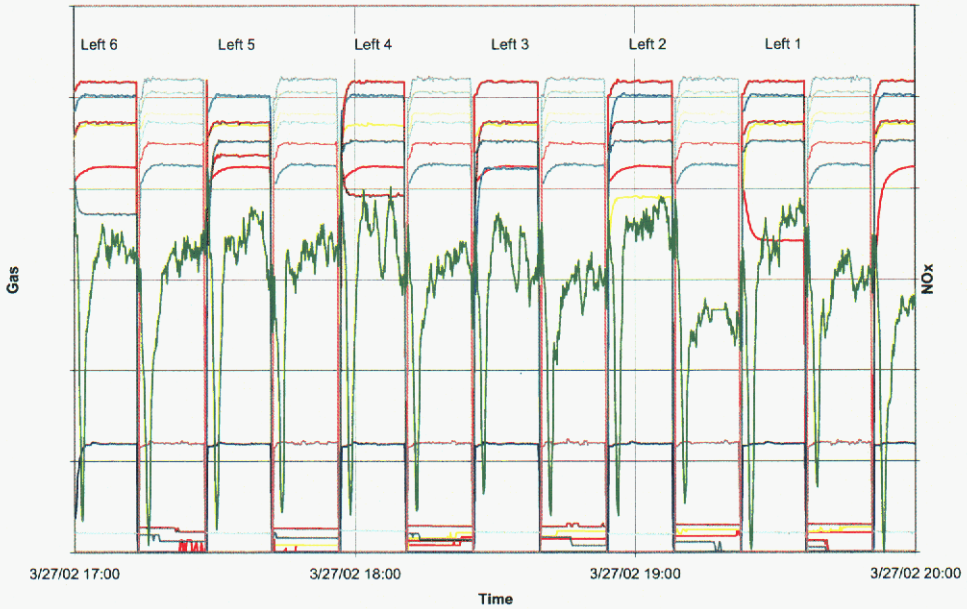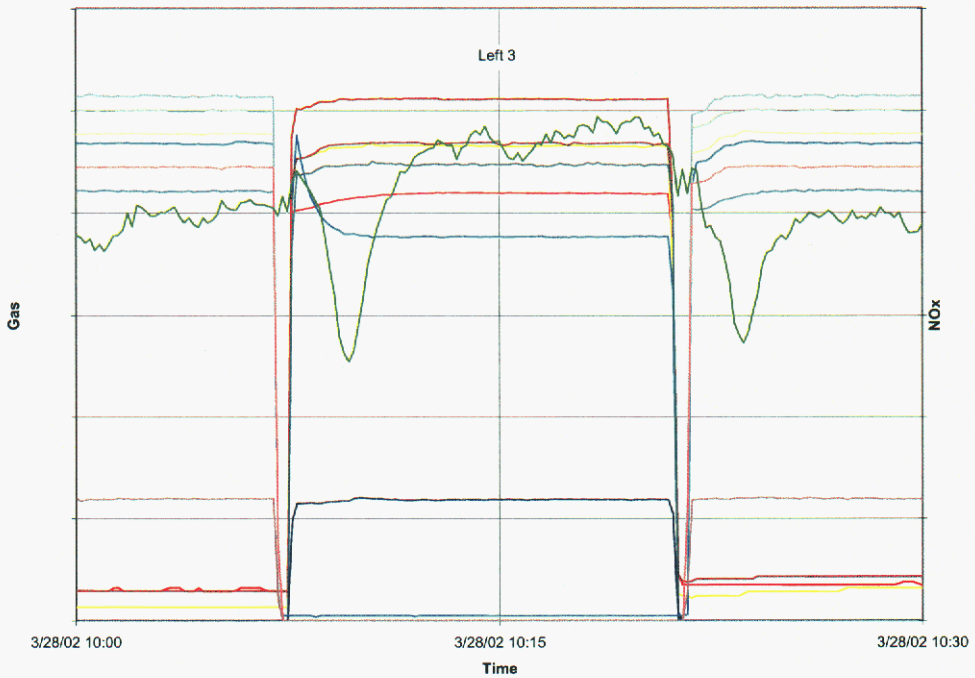

Figure 4-7. Port-to-port NO_X source identification. Port-Left 3 retest. Green = NO_X. Other traces can by identified by correlating their shifts with the port labels.

a. Typical Right Firing Cycle   b. Typical Left Firing Cycle
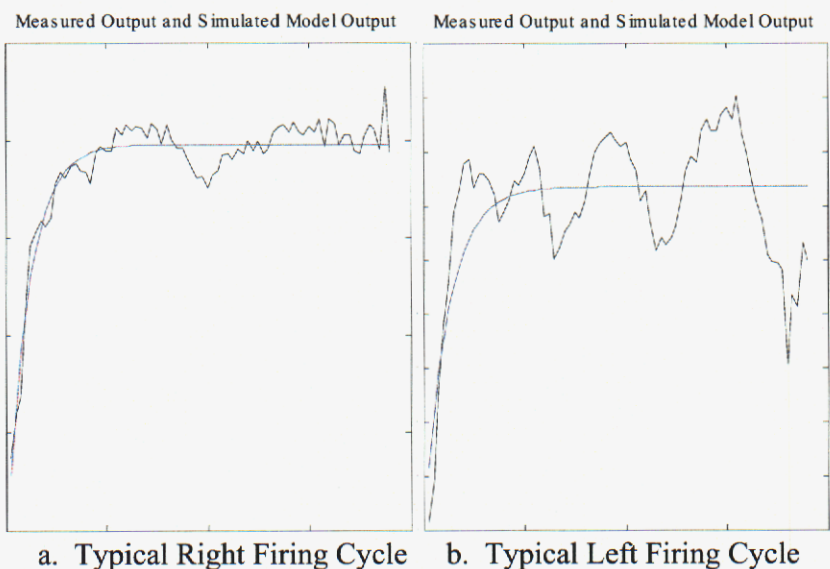
Figure 4-8. Port-to-port transfer function curve fit. NO_X versus time.

Figure 4-9 summarizes the results of the curve fitting. The figure shows the percent increase in NO_X output for a fixed change in port gas flow. Evaluating and comparing the percent changes, rather than the absolute changes, effectively normalizes the results. After preliminary analysis of the data, the Port-Left 3 change seemed lower than the predominant trend would predict it to be, so that port was retested. However, the gas change for the Port-Left 3 retest was 150% greater than the previous day's gas change. Though the normalization procedure should remove most consequences of this difference and make the data comparable, non-linear effects may not be completely normalized in this way.
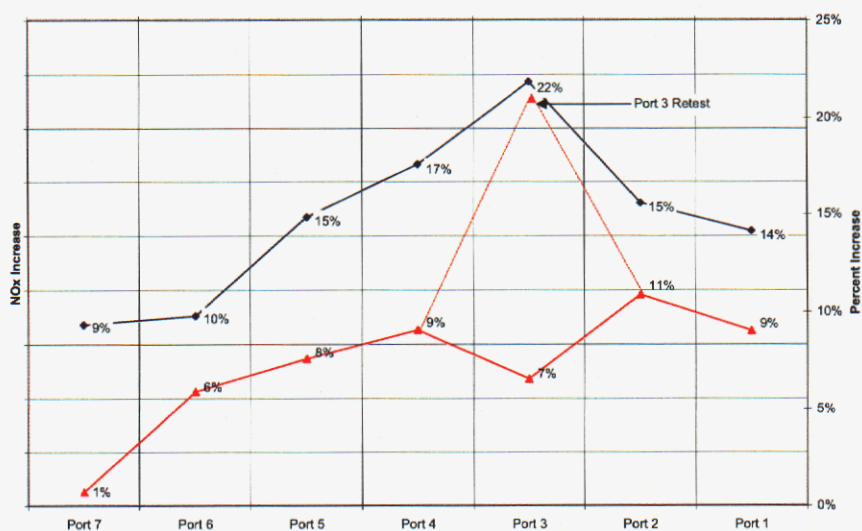
Figure 4-9. Port-to-port summary plot. Blue trace = right ports. Red trace = left ports.

Magnitude Test

This experiment was conducted on March 25, 2002 from 12:08 to 17:39. Figures 4-10 and 4-11 show the raw data from the test.
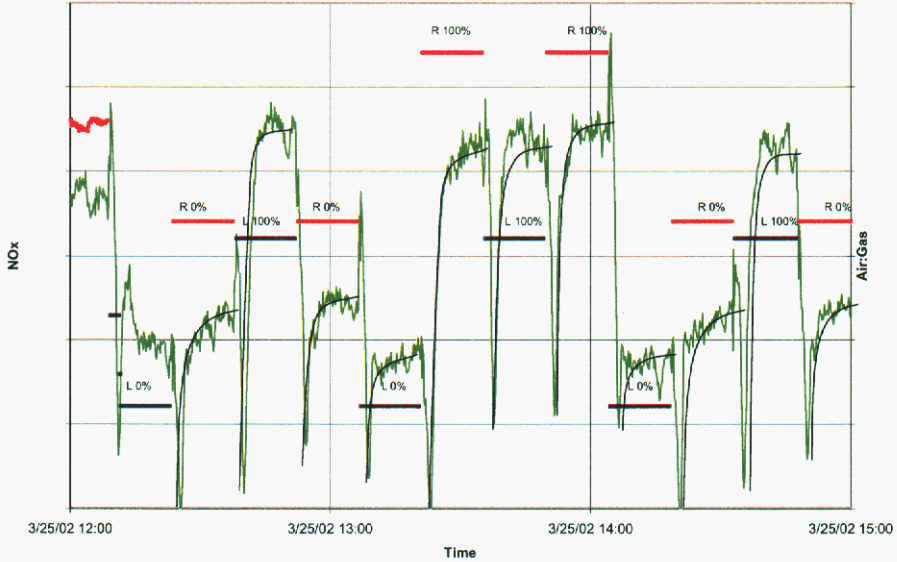
Figure 4-10. Magnitude test raw data (12:00-15:00).
Green = NO$_X$. Black = NO$_X$ reference curve.
Pink = right percent control effort. Blue = left percent control effort.
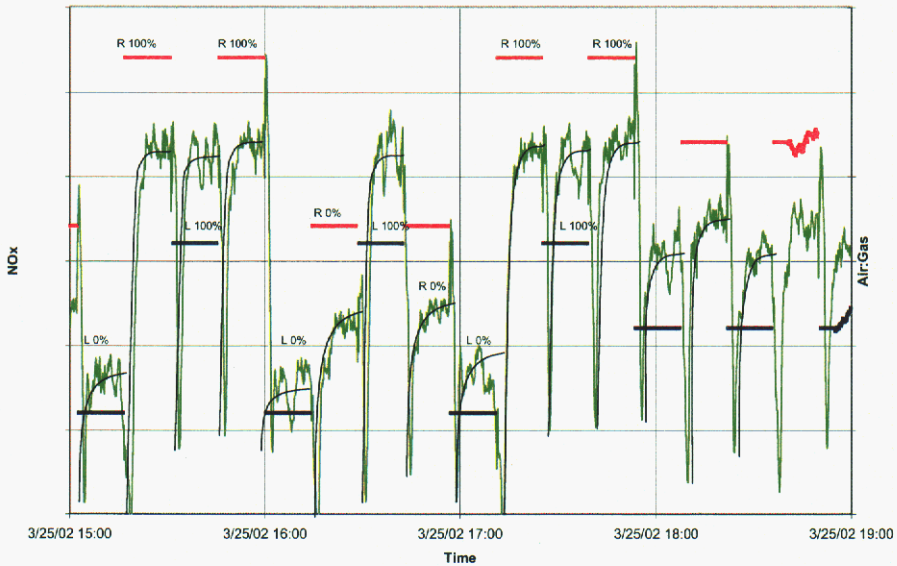
Figure 4-11. Magnitude test raw data (15:00-19:00).
Green = NO$_X$. Black = NO$_X$ reference curve.
Pink = right percent control effort. Blue = left percent control effort.

The NO_X data for individual firing cycles were extracted from the raw data and are shown in Figure 4-12. The final NO_X values for the curves separate into two distinct clusters, corresponding to 0% control effort and 100% control effort. The higher control efforts correspond to higher air-to-gas ratios and the higher NO_X production rates.

Each of the curves shown in Figure 4-12 was fit to a first order transfer function, relating the air-to-gas ratio to the NO_X production rate. Figures 4-13 and 4-14 show four typical curve fits. As before, the curve fitting routine was an Auto Regressive with Extra Input (ARX) and the model for the curve fit was a first order transfer function with one pole and no zeros. The data transport delay was determined by comparing the rising edge in the gas flow rate to the rising edge in NO_X and was removed from the data before the fit. The resulting curves illustrate the exponential increase in NO_X with time (with gain and time constant). The gain correlates to the excess air-to-gas ratio, calculated from the total air-to-gas ratio by subtracting the stoichiometric air-to-gas ratio and air in-leakage from the total.
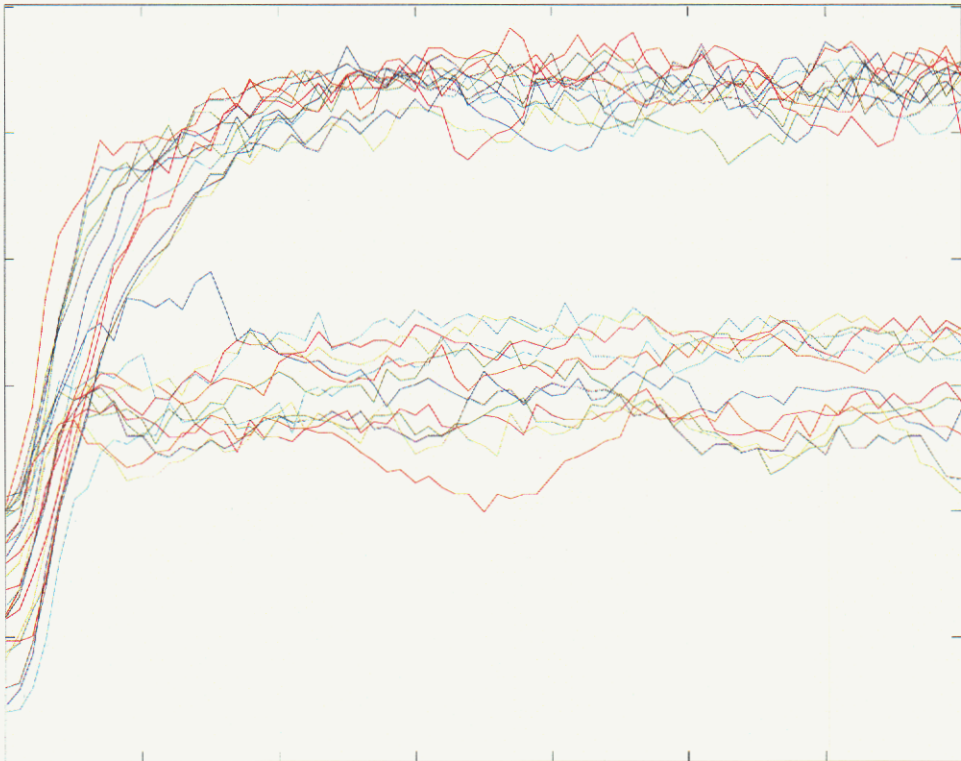
Figure 4-12. Individual NO_X curves extracted from the Magnitude tests. NO_X versus time.

Measured Output and Simulated Model Output

Measured Output and Simulated Model Output
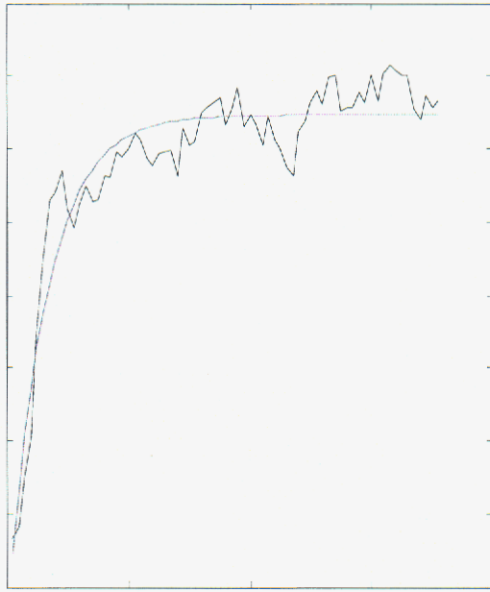
a. Typical right 0% control effort.   b. Typical right 100% control effort.
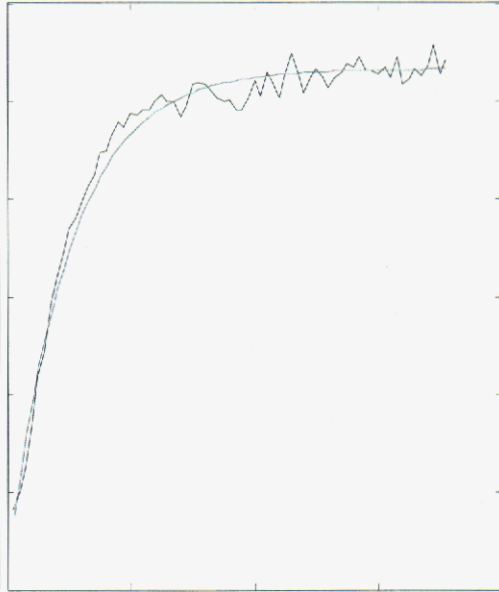
Figure 4-13. Magnitude transfer function curve fit. NO_x versus time.

Measured Output and Simulated Model Output

Measured Output and Simulated Model Output
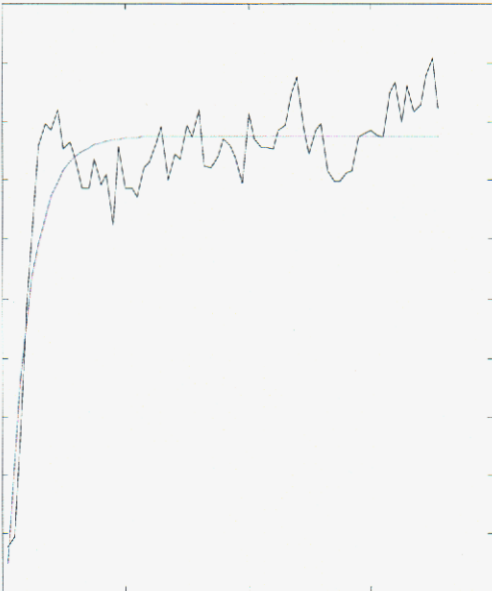
a. Typical left 0% control effort.   b. Typical left 100% control effort.
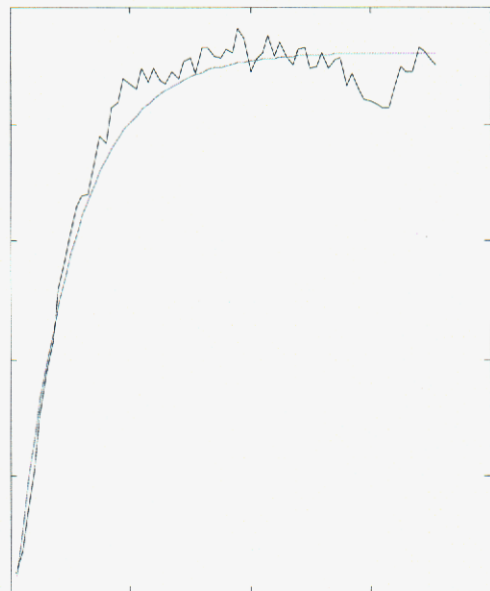
Figure 4-14. Magnitude transfer function curve fit. NO_x versus time.

__Loop Interaction.__   Figure 4-15 illustrates a control loop interaction that was discovered during the course of the test runs. The interaction was identified when an unstable oscillation consistently appeared in the NO_X output from the left side of the furnace. This type of oscillation is characteristic of a control loop that is not properly tuned and forcing an otherwise stable system out of control. However, since the control loops that typically can affect the NO_X were in manual mode, such an interaction was unexpected. The oscillation was also observed in the refiner pressure control system, also shown in Figure 4-15, but the process engineers indicated that refiner pressure is unlikely to affect NO_X production so dramatically.

A second NO_X sensor (ENERAC) was located in the connecting flue between primary and secondary regenerators, for comparison with the readings from the primary NO_X sensor (CEM) in the stack. The ENERAC instrument indicates the NO_X volume fraction, in contrast with the stack CEM, which reports the NO_X emission index, taking into account the stack gas flow rate. Figure 6-16 shows that the signal from the sensor in the connecting flue oscillates at the same frequency as that from the stack CEM. Identification of the source of this oscillation requires further investigation.
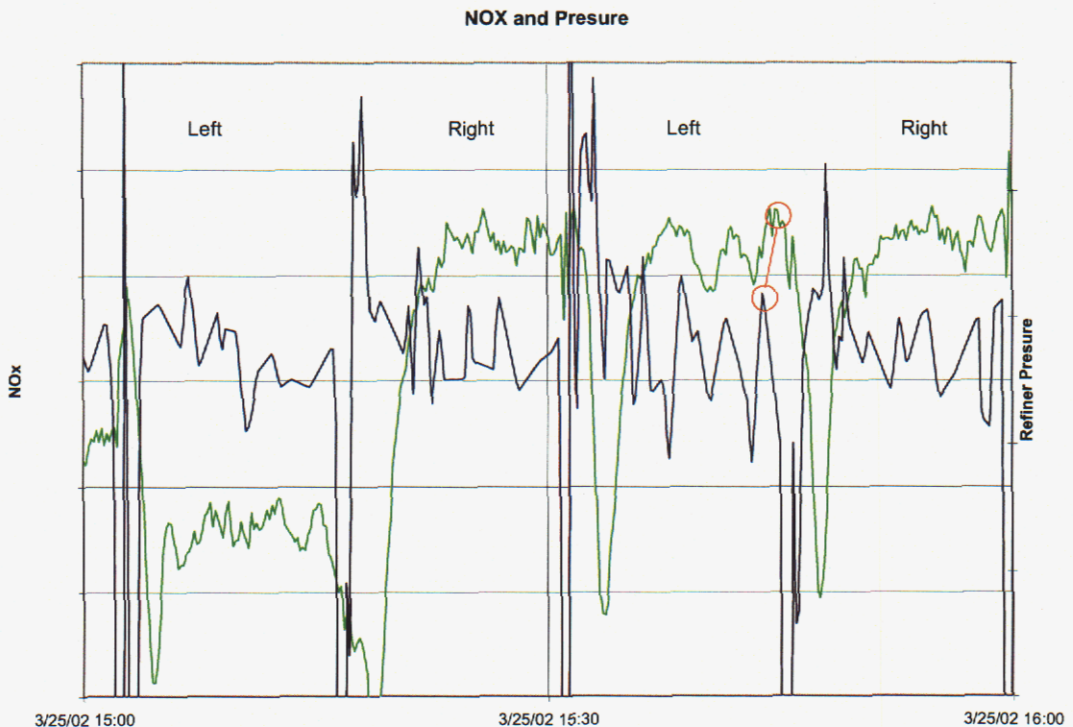
Figure 4-15. Example of control loop interaction.

Figure 4-16. Oscillation in NO_X production due to control loop interaction.

NO_X Control Trend Test

This experiment was conducted on March 26, 2002. The raw data from the Trend Tests are shown in Figures 4-17 and 4-18. The 7th firing cycle, at 13:37, was inadvertently started with 0% control effort, before proceeding to the planned 100% control effort, then transitioning to 0% control effort. This serendipitous event provided a richer data set for observation of the dynamic behavior of the process. Another such opportunity arose in the 20th firing cycle, at 16:42, when the control effort was inadvertently dropped from 100% to 0%, then corrected a short time later.

The NO_X data for individual firing cycles, shown in Figure 4-19, were extracted from the raw data. Final NO_X values for the firing cycles fall into three distinct clusters, corresponding to tests when: (1) the control effort began at 100% and was decreased to 0% midway through the firing cycle, (2) the control effort remained fixed at 50% throughout the firing cycle, and (3) the control effort began at 0%, then was increased to 100% midway through the firing cycle.
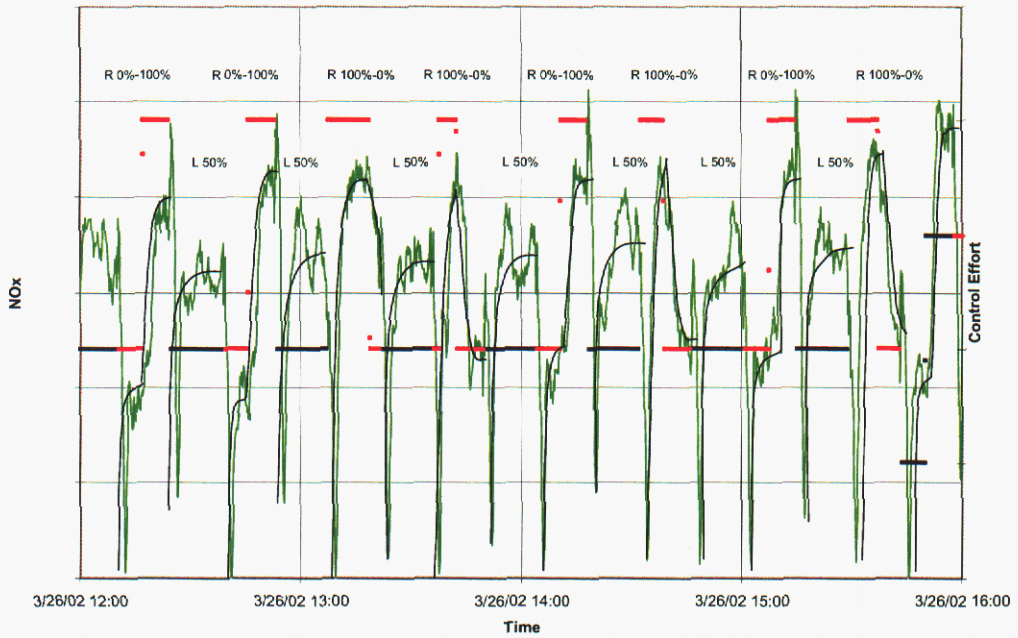
Figure 4-17. Trend test raw data (12:00-16:00).
Green = NO_X. Black = NO_X reference curve.
Pink = right percent control effort. Blue = left percent control effort.
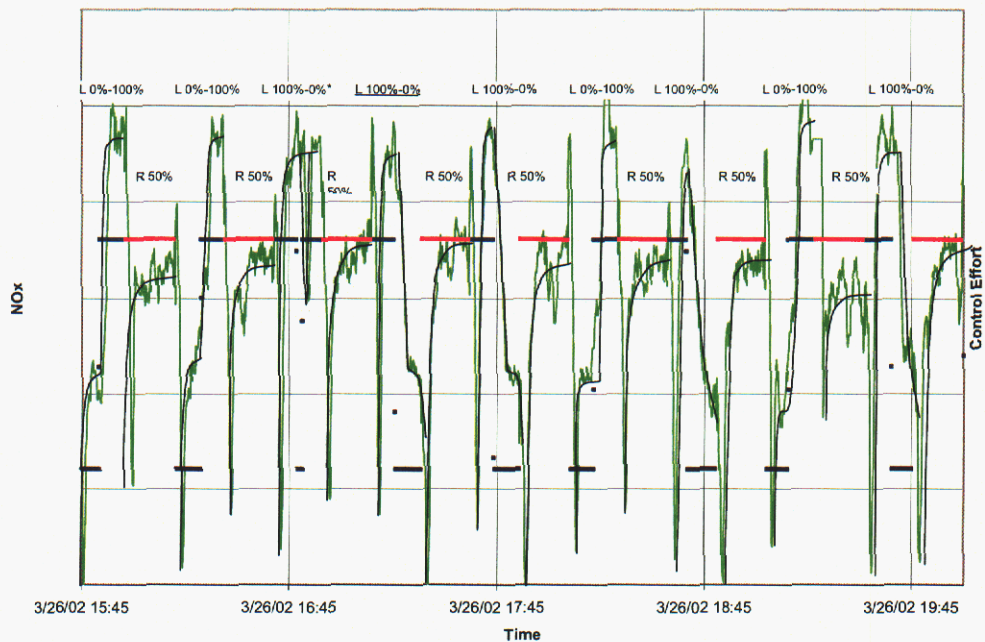
Figure 4-18. Trend test raw data (16:00-19:45).
Green = NO_X. Black = NO_X reference curve.
Pink = right percent control effort. Blue = left percent control effort.
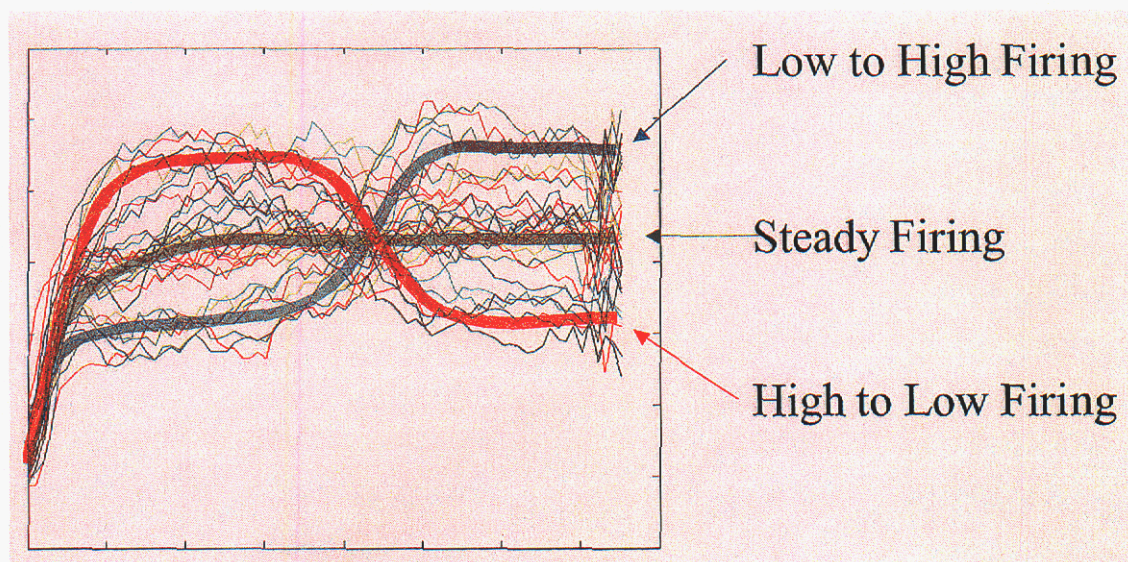
Figure 4-19. NO_x versus time curves extracted from the Trend test data.

Each of these curves for the individual firing cycles was fit to a first order transfer function, relating the air-to-gas ratio to the NO_x production rate. Figures 6-20, 6-21, and 6-22 show eight typical curve fits. As before, the curve fitting routine was an Auto Regressive with Extra Input (ARX) and the model for the curve fit was a first order transfer function with one pole and no zeros. Two different transport delays are evident from the raw data. Two delays are expected since there are two process inputs that affect NO_x production in this test. The first transport delay is the same as that found in the Magnitude test, determined by comparing the rising edge in the gas flow rate to the rising edge in the NO_x. The second, much shorter, transport delay was that between the change in air-to-gas ratio and change in NO_x production at mid-firing-cycle. The data were shifted by the second (shorter) time delay before performing the curve fits. The resulting curves illustrate the exponential change in NO_x with time (with gain and time constant) at the beginning of each firing cycle, and in response to changes in air-to-gas ratio. The gain was related to the excess air-to-gas ratio, calculated by subtracting the stoichiometric air-to-gas ratio and air in-leakage from the overall air-to-gas ratio.

Transport Delay Anomaly. As noted above, the Trend test analysis yielded two different transport delays for NO_x production. The first delay is the time between the instant when the gas is turned on at the beginning of a firing cycle and the time when the CEMS sensor in the stack registers an increase in NO_x production. The observed transport delay is reasonable, considering the time it should take combustion products to travel from the furnace through the regenerators, flues, and electrostatic precipitator to the sampling point in the stack, plus the time required for the sample to travel from the sampling point to the NO_x analyzer in the instrument room on the ground. The second transport delay is that from the instant when the air-to-gas ratio was changed at mid-firing cycle to the time when the stack CEMS NO_x sensor responded to the change. The delay

observed in this case seems unreasonably short, considering that it should take about the same time for the NO_x analyzer to respond to a change in combustion air flow rate as it takes to respond to the change from no gas to full flow at the beginning of a firing cycle.

The relationships between NO_x measurements, air-to-gas ratio control effort, and the apparent transport delays are shown in Figure 4-23. The figure shows four traces: (1 and 2) left and right ENERAC NO_x measurements in the connecting flues between the primary and secondary regenerators, which should respond quickly to changes in NO_x production, (3) CEMS NO_x measurement in the stack, a long distance from the furnace, that should exhibit a significant delay before responding to changes in NO_x production, and (4) air-to-gas ratio control effort, whose changes are expected to correspond to changes in NO_x production in the furnace. The ENERAC NO_x measurements in the connecting flues respond within a few seconds of a change in air-to-gas ratio. The CEMS NO_x emission index shows a reasonable time delay of 110 to 160 seconds following the changes in ENERAC NO_x and air-to-gas ratio. However, the CEMS NO_x shows an immediate upward trend when the air-to-gas ratio is increased in the middle of a firing cycle, and an immediate downward trend when the air-to-gas ratio is decreased in the middle of a firing cycle. Since a transport delay is the time between a command input and the first detectable sensor response, the apparent transport delay is very short. Since it is physically impossible for combustion products to reach the CEMS sensor from the furnace so quickly, a possible explanation is that the stack flow sensor responds to a disturbance in flue gas flow rate or static pressure well before combustion products reflecting a new air-to-gas ratio actually reach the NO_x analyzer. A change in actual or apparent stack gas flow rate would immediately register as a change in NO_x emission index, even in the absence of any change in NO_x volume fraction observed by the NO_x analyzer.

Measured Output and Simulated Model Output Measured Output and Simulated Model Output Measured Output and Simulated Model Output
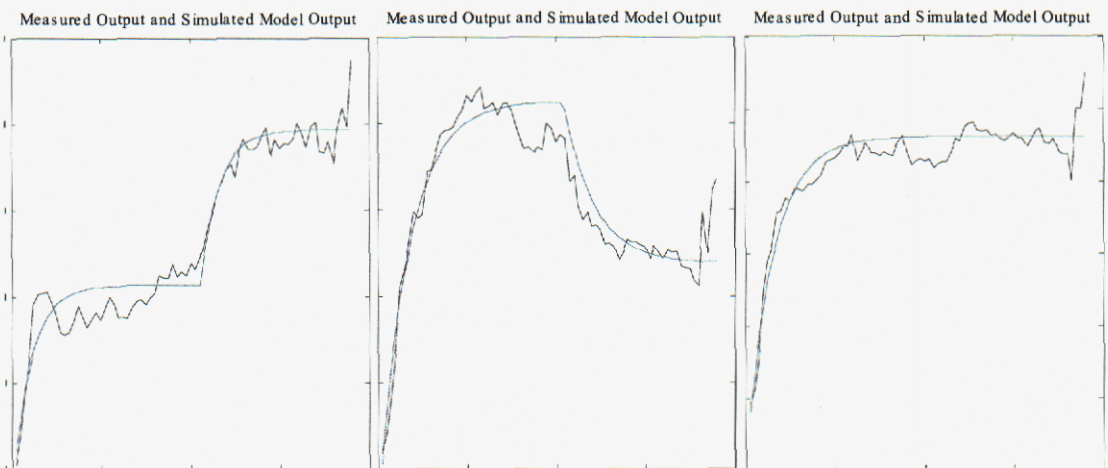
Figure 4-20. Typical right side firing cycles. NO_x versus time.
a. Control effort increasing from 0% to 100%.
b. Control effort decreasing from 100% to 0%. c. Fixed control effort.

Measured Output and Simulated Model Output   Measured Output and Simulated Model Output   Measured Output and Simulated Model Output
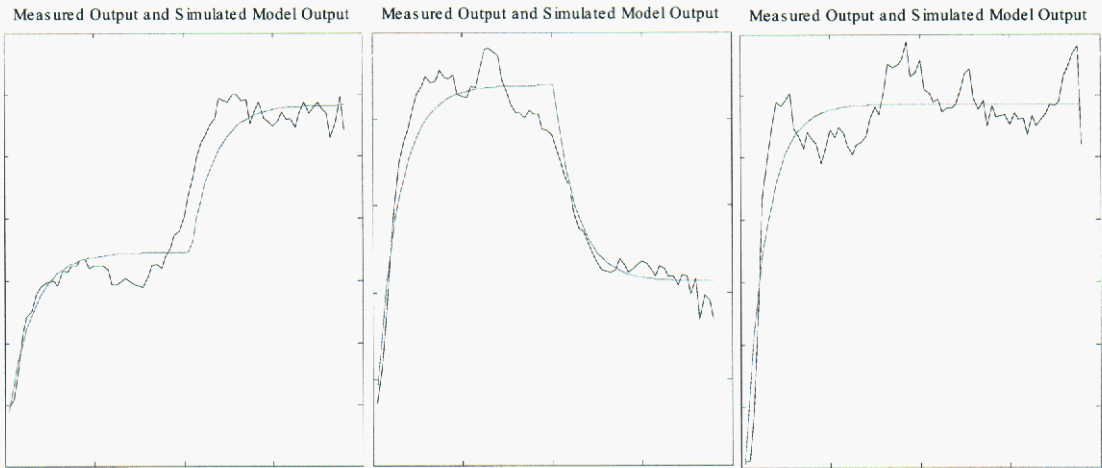
Figure 4-21. Typical left side firing cycles. NO_x versus time.
a. Control effort increasing from 0% to 100%.
b. Control effort decreasing from 100% to 0%. c. Fixed control effort.

Measured Output and Simulated Model Output   Measured Output and Simulated Model Output
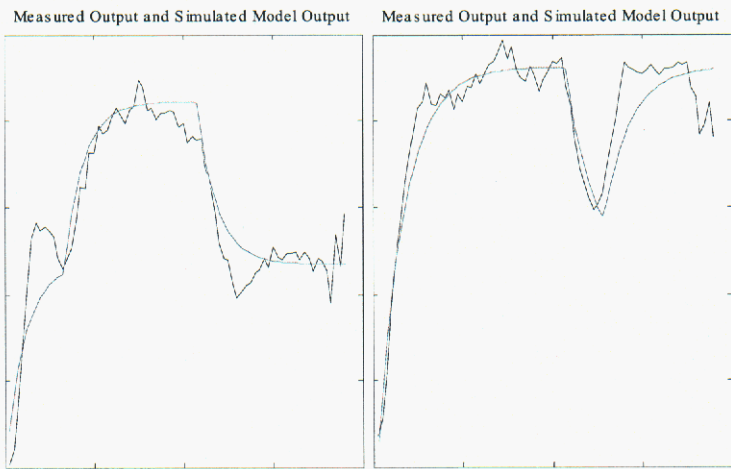
Figure 4-22. Two serendipitous events. NO_x versus time.
a. Firing cycle inadvertently started low before a 100% to 0% transition in control effort.
b. Inadvertent drop in control effort closely followed by recovery.

Discussion

The tests produced a great deal of useful information that can be used to tune the existing NO_x control loop. However, and more importantly, the information can be used to design a new NO_x control loop that accounts for the new discoveries resulting from these tests. Since this report cannot disclose proprietary information, the discussion here will be at a high level.
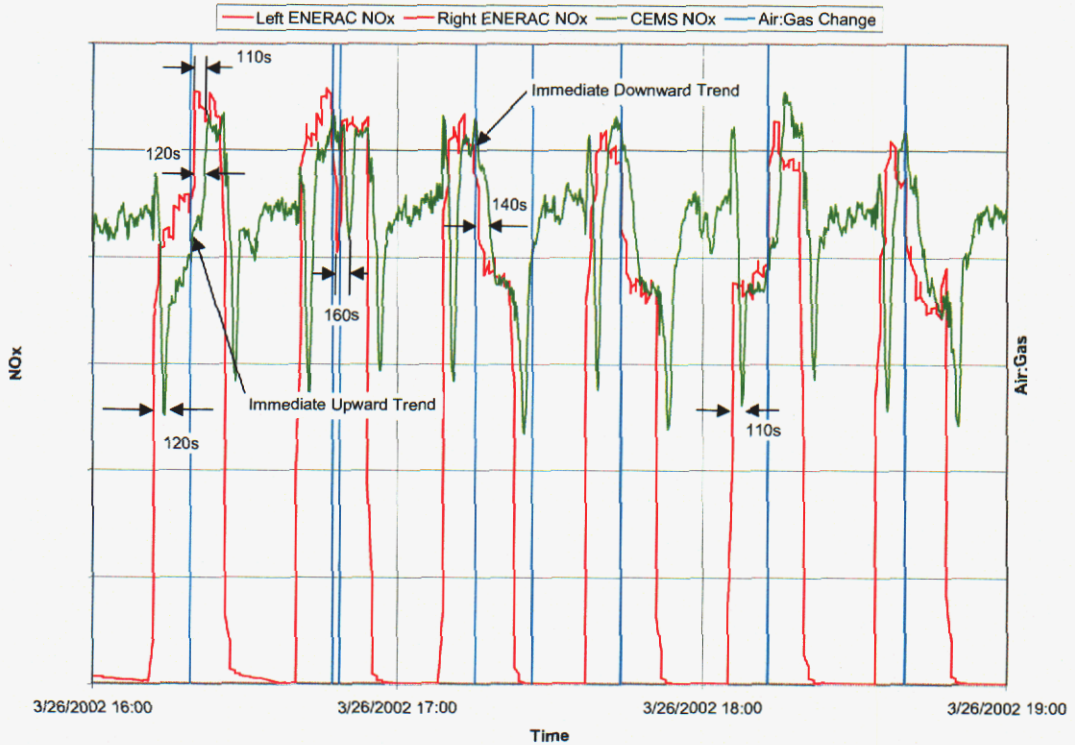
Figure 4-23. Transport delay analysis.

The initial observation from the test as a whole is that fewer tests will have to be run in the future to get similar information. This is because we were able to eliminate the consideration of some phenomenon that required several tests at different settings to extract the desired information. For example, we discovered that the conditions of a given firing cycle had little residual affect on NO_X production in subsequent firing cycles. Therefore, in future tests, a firing cycle at a particular set of conditions will not need to be preceded by alternative firing cycles at several different settings, in order to remove their effects.

Open Loop Control Test

The open loop test showed that the natural process variation over the course of a few hours was not significant compared to the degree of process variation that was imparted to the system during the other tests. However, the variation observed during the open loop control test should be considered when evaluating the test data. If, for example, the natural process variation over the course of one firing cycle can cause the NO_X production rate to change by 5%, then any changes observed in the experiments should only be considered significant if they are greater than 5%. By always applying this criterion, the conclusions drawn from a test will be more credible.

Port-to-Port NO$_X$ Source Identification Test

The Port-to-Port tests indicate that NO$_X$ production increases more near port three than near the other ports for the same decrease in natural gas flow to its burners. This test only considered the effect of decreasing the amount of gas going to a particular port. However, it is not an unreasonable assumption that the converse will also be true for small changes in gas flow rate. That is, for small increases in the gas to particular ports, a change at port three is expected to cause the greatest reduction in NO$_X$, and the others will follow the general trend shown in Figure 4-9. The location of the most influential port may be associated with furnace temperature in that area, mixing effectiveness in that area, or furnace geometry.

Magnitude Test

In the Magnitude tests, the NO$_X$ response was well above the level of noise on the NO$_X$ sensor and was well above the perturbations in NO$_X$ from other process controls. The data-sampling rate was sufficient to capture the primary process dynamics, although faster data sampling would have allowed us to determine the transport delay with greater accuracy.

One important observation from the magnitude tests is that conditions during a given firing cycle have little residual effect on subsequent firing cycles. We worried that the converse might be true when some historical production run data showed that if a given firing cycle produced a great deal of NO$_X$, then the next firing cycle would also produce high NO$_X$, regardless of control action. However, we found that we could manipulate production of NO$_X$ regardless of conditions during the previous firing cycle. The phenomenon observed in the historical production data must have been caused by an as yet undiscovered phenomenon.

Another important finding was that there are ways to exert significant control over NO$_X$ production. This was also in contrast to indications from the historical production run data, from which it appeared as though the NO$_X$ control loop had only a small influence on NO$_X$ production.

During the reversals at the end of cycles during which firing was from the right, there was a sharp peak in NO$_X$ indicated by the stack CEM, as shown in Figure 4-24. Since the onset of reversal should produce no additional NO$_X$, we believe that this peak is caused by a momentary increase in stack gas flow. As mentioned in the description of the transport delay anomaly, above, calculation of the NO$_X$ emission index by the stack CEM combines the stack gas flow and NO$_X$ volume fraction, so an increase in flue gas flow rate (or a perturbation decreasing the static pressure), even in the absence of any change in NO$_X$ concentration, will cause an increase in the emission index. The green trace in Figure 4-24 shows a distinct peak at the onset of reversal after firing on the right. The red trace in the figure is the measurement of NO$_X$ by the ENERAC instrument in a

sample from the left connecting flue, which contains the exhaust from the furnace when firing on the right. Since no peaks in NO_X appear in the ENERAC data at the onset of reversal, the NO_X spikes in the stack CEM data appear to be anomalous. The spikes in the CEM record could arise from a momentary increase in flue gas flow caused by a mistimed valve in the reversal system.
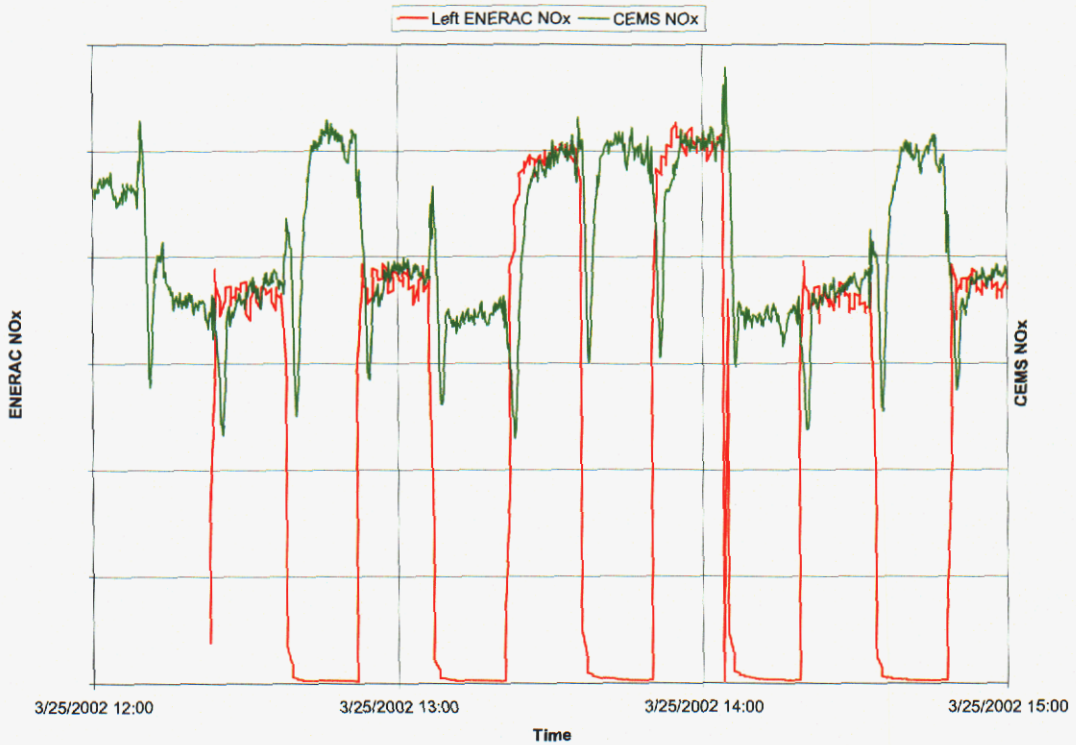
Figure 4-24. A characteristic peak in NO_X during right side reversals appears in the CEM data but not in the ENERAC measurements.

As mentioned in the section entitled, "Loop Interaction," we found that unstable oscillations were present when firing on the left. This type of oscillation is characteristic of an out-of-control feedback loop, not a natural process condition. Though we observed similar oscillations in the refiner pressure, we do not believe that the refiner pressure control loop is causing the oscillations. Further work is needed to determine the source of the apparently forced oscillation. Under closed loop control of NO_X, suppressing this oscillation would consume up to 50% of the available control effort. If the oscillation were eliminated at its source, then the NO_X control loop could be much more effective.

Similar changes in NO_X control effort on the two sides of the furnace did not produce similar changes in NO_X production. The left side of the furnace produced 25% more NO_X than the right side after a similar change in air-to-gas ratio. Only 7% of this difference can be attributed to the difference in set points on the two sides of the furnace.

At high levels of control effort, similar emissions of NO_X were observed when firing on the left and on the right, though the air-to-gas ratio was higher when firing on the right. This suggests that the actual air-to-gas ratios are similar on the two sides, and that the values indicated by the control system are not accurate, perhaps due to differences from one side to the other in loss of air from the flues downstream from the air flow measurement points.

At low levels of control effort, more NO_X was produced when firing on the right than on the left. This could be a non-linear effect of the air losses from the flues, such that at high air-to-gas ratio, the amounts of air leakage result in similar air-to-gas ratios in the furnace regardless of firing direction, but because changes in leakage on the two sides are not in the same proportion to changes in total air flow rate, a differential in NO_X production when firing left and right appears at low air-to-gas ratio.

NO_X Control Trend Test

Air-to-gas ratios were changed in the middle of firing cycles to determine their effects on NO_X production. This test was intended to answer the question, "to what extent does NO_X production depend upon active control and to what extent does it depend upon initial conditions?"

The tests revealed that the system behaves differently, from the point of view of NO_X production, when firing on the left and right, and not simply in the magnitude of NO_X produced. For example, when the air-to-gas was reduced at mid-cycle when firing on the right side of the furnace, NO_X production decreased exponentially, as expected. However, when the air-to-gas ratio was reduced at mid-cycle when firing on the left side of the furnace, NO_X production decreased linearly or logarithmically.

Some of the phenomena observed in the Magnitude tests were also observed in the Trend tests. In the Trend tests, the right firing cycle exhibited sharp spikes in NO_X at the onset of reversal, just as in the Magnitude tests. Unstable oscillations were observed when firing on the left during both the Magnitude and Trend tests. Oscillations were also detected, but to a lesser extent, when firing on the right.

Changes in NO_X production resulting from changes in air-to-gas ratio at mid-cycle during the Trend tests were similar to the changes associated with different air-to-gas ratios set at the beginning of firing cycles in the Magnitude tests. This is a good indication that the relationship between NO_X and air-to-gas ratio is linear over the range of air-to-gas ratios accessible through variation in control effort.

Conclusions from the NO_X Control Experiments

The four NO_X experiments that were conducted during the week of March 25, 2002 on Line 14-2 were well planned and well executed. Plant personnel provided

unprecedented access to control of conditions in the furnace to make possible the successful execution of the tests. Making use of the experience gained, it will be possible, in future tests, to gather an equivalent amount of information in a shorter period of time. The key observation that will allow us to compress future tests is the fact that conditions during a given firing cycle do not significantly influence NO_X production during subsequent firing cycles. A second observation that will allow us to make future testing more efficient is that NO_X production behaves approximately linearly with variation in air-to-gas ratio over the operating range of the NO_X control loop.

The Open Loop tests demonstrated that variability in NO_X sensor output due to other process controls and sensor noise were sufficiently small that the data to be gathered would provide meaningful information. The Port-to-Port tests provided quantitative information about the relative influence that changes in gas flow to the burners in individual ports have on NO_X production in the furnace as a whole. The Magnitude tests indicated that sufficient control over NO_X is provided by the range of air-to-gas ratio under control of the feedback loop. Data gathered during the Magnitude tests permitted evaluation of the NO_X production time constant, transport delay, and gain. The Magnitude tests revealed control loop interactions and sensor dynamics that were not well understood prior to the tests. For example, the refiner pressure and NO_X production exhibited correlated unstable oscillations, which warrant further investigation. An anomalous peak in NO_X was observed at the onset of reversal from right to left firing, thought to arise from a transient increase in stack flow caused by less than optimum valve timing.

The Trend tests provided information about the dynamics of mid-firing-cycle adjustment of air-to-gas ratio for control of NO_X. By changing the control variable midway through a firing cycle, the dynamic relationship between the control variable and NO_X response was determined. The NO_X control loop appeared to exhibit a much shorter transport delay in response to mid-cycle changes in air-to-gas ratio than it did in response to ignition of natural gas at the beginning of a firing cycle. When the air flow was adjusted in the middle of a firing cycle, the NO_X emission index indicated by the stack CEM appeared to respond before sufficient time had elapsed for combustion products to travel from the furnace to the stack and from the stack to the NO_X analyzer. Apparently, the change in flue gas flow or a pressure disturbance caused by adjustment of the combustion air is transmitted to the stack within a few seconds. Because the stack gas flow rate is included in the calculation of the emission index, a change in emission can be registered even before any change in NO_X concentration is detected by the analyzer. The actual transport delay between adjustment of the air-to-gas ratio and response of the NO_X CEM accurately reflecting the new condition was ~ 110 to 160 seconds. The Trend tests demonstrated that NO_X production in the furnace responds to changes in air-to-gas ratio on a time scale shorter than the reversal cycle and that the change in NO_X resulting from a given adjustment in air-to-gas ratio at mid-cycle was approximately the same as that observed when the same adjustment was made at the beginning of a firing cycle.

5. COMBUSTION MODELING OF AN INDUSTRIAL GLASS-MELTING FURNACE: Modeling Concerns and Recommendations*

Padmabhushana R. Desam and Philip J. Smith
Combustion and Reaction Simulations (CRSIM) Research Group
The University of Utah, Salt Lake City, UT

Objective

The main objectives of this report are 1) to use Computational Fluid Dynamics (CFD) simulations to understand port-port interaction in the glass furnace and 2) to make recommendations about experimental data that would be useful for model validation. Since not much experimental data is available for the Mt. Zion 14-2 furnace at this stage, an existing database of measurements for a similar furnace (Newbold et al., 1997) is considered in order to address the first objective. The furnace considered in this work is a side-port, regenerative, flat glass furnace similar to the Mt. Zion furnace.

The tasks we have completed towards the objectives are as follows:

1. Perform a single-port simulation to compare the velocity, temperature, and species concentration fields with the experimental data.

2. Perform a three-port simulation to identify the influence of nearest neighbor ports on the middle port.

3. Perform a full furnace simulation to identify the influence of all other ports on a single port.

4. Perform a sensitivity study to identify the influence of

   a. Glass surface temperature boundary conditions on the burner plane and on the whole domain.

   b. Inlet air flow rates on flow, temperature fields and major species concentrations in the furnace.

   c. Inlet air profiles on flow, temperature fields and major species concentrations in the furnace.

   d. Computational resolution of mixing in the port neck on flow, temperature fields and major species concentrations in the furnace.

   e. Crown temperature profile on the burner plane and on the whole furnace domain.

---

*See also Desam and Smith (2003). Links to presentations and publications related to this work may be found on the authors' web sites at <http://www.crsim.utah.edu/~desam/> and <http://opus.utah.edu/~smith/>.

Though the ultimate objective of this work is to predict and control the NO_X in the glass furnace, obtaining the flow field, temperatures and species distributions is very important in calculating the NO_X levels. NO_X does not alter the flow or temperature fields and thus generally is obtained as a post processed calculation (Carvalho et al., 1990). Validating the simulation capability of the major species and temperature distribution independent of the NO_X model is a necessary step in the overall validation.

Furnace Description and Experiments

A schematic of the side-fired, regenerative, six-port glass furnace combustion chamber used in the modeling work of this report is shown in Figure 5-1. The furnace is 11 meters wide, 21.5 meters long and 2.6 meters high in the center from the glass bottom. It has six port necks; each of them is 3.35 meters long with same area of cross-section and connects the regenerator with the furnace. Each port has two 4.4 cm diameter pipe burners on the sides and the burners centerlines intersect with the port neck centerline at the edge of the furnace wall.
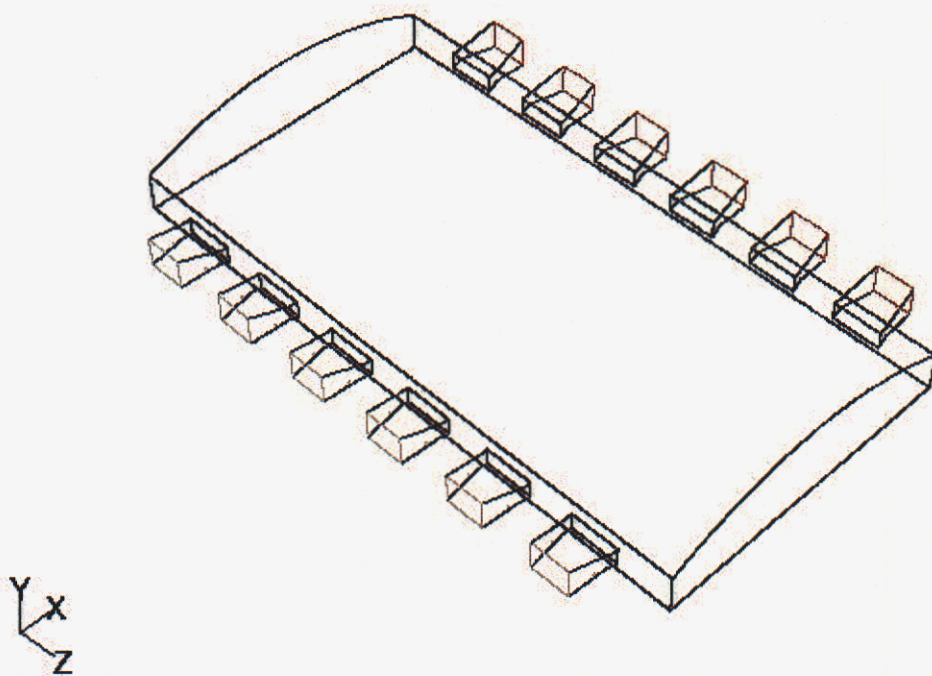

Figure 5-1. Schematic of the side-port, regenerative, flat glass-melting furnace combustion chamber.

Detailed experimental measurements (Newbold et al., 1997) are available along the centerline for port neck three at six locations, which are 1.1, 2.3, 3.4, 4.4, 5.3 and 7.6

meters from the north side furnace wall. These measurements include velocity, temperature, species concentration and radiant flux at different heights from the glass surface. There are no data available for NO_x from this source. Table 5-1 summarizes the operating conditions. The furnace operates on fifteen minute firing cycles; a fifteen-minute firing from north side with exhaust on south side and a fifteen-minute firing from south with exhaust on north side for regenerative purposes.

Table 5-1. Operating conditions of the glass-melting furnace (Newbold et al., 1997).

Wall Temperatures (K)	
North furnace wall	1910
South furnace wall	1900
Mass flow rates (kg/hr)	
Fuel	2763
Air	66,557
Stoichiometry (equivalence ratio)	
Overall plant value	0.61
Portneck 1	0.49
Portneck 2	0.54
Portneck 3	0.66
Portneck 4	0.72
Portneck 5	0.65
Portneck 6	0.58
Fuel Composition (volume %)	
Methane	87.49
Nitrogen	6.79
Ethane	3.66
Propane	0.77
Carbon dioxide	0.58
Oxygen	0.46
Hexane	0.10
n-butane	0.08
Isobutane	0.05
n-pentane	0.02

The fuel flow rates were individually measured for each burner and the sum was used to find the overall plant equivalence ratio. With the aid of a differential-pressure orifice meter, the overall airflow rate for the furnace was measured. Equivalence ratio for each port was calculated by integrating the measured port neck velocity data (measured only along the vertical centerline of the port neck and was assumed to be invariant along the horizontal direction) over the port neck cross-sectional area determined from the

furnace drawings. In practice, deposits have accumulated on the port necks over years of use. These deposits have decreased the cross-sectional area by an unknown amount. This results in higher airflow rates than when the furnace was operating at design conditions. This difference is estimated to be as high as 15% for this furnace.

A straight water-cooled stainless-steel pitot tube was used to measure gas-velocities. Gas temperatures were measured with the aid of a triple-shielded water-cooled pyrometer. To characterize the wall incident radiant heat flux on the crown, a water-cooled ellipsoidal radiometer was used. Combustion gases were analyzed with several on-line gas concentration analyzers in real time by being drawn through a water-cooled stainless steel collection probe. The wall temperatures were optically measured.

Simulation Details

In order to study the effect of port-to-port interaction, three different sets of simulations are built and solved for velocities, temperatures and species concentrations. Since the experimental data is only available for port three, the strategy is to compare the simulations with the measured data quantitatively for only port three. This serves our objective, which is to study the port-to-port interaction rather than validating the full furnace.

Figure 5-2 shows the geometry of a single-port combustion chamber. A single port model assumes the existence of symmetry between port necks and also within the port. That's why only half of the port is considered rather than the full port. The advantage of the single port model is the ability to resolve the wide range of scales present in the glass furnace with a fine grid. These models are computationally cheap and allow studying the effect of different operating and design variables economically. But, the glass furnace operates with different air and fuel flow rates for different ports, which may disrupt symmetry within and between ports.

In order to study the effect of the neighboring ports, a three-port model is built and is shown in the Figure 5-3. This model includes the effect of ports two and four (immediate neighbors) on the port three, which is located in the center of the simulation. It should also be observed from the geometry that only half of the geometry for port two and four is considered since we are interested in studying the effect of adjacent flames on port three. These three ports operate with different firing conditions, port four operates with high equivalence ratio than port three and port two operates with low equivalence ratio than port three. These differences are included in the simulation.

Figure 5-1 shows the geometry of the full furnace and is the geometry for the third simulation set. This model helps in the evaluation of the assumptions made in the other two models. In this case, the penalty is the coarse mesh because of the large dimensions of the furnace. This affects the quality of the results obtained when compared to the results from the other two models. Table 5-2 summarizes and compares the mesh elements (hexahedral) for these three models.
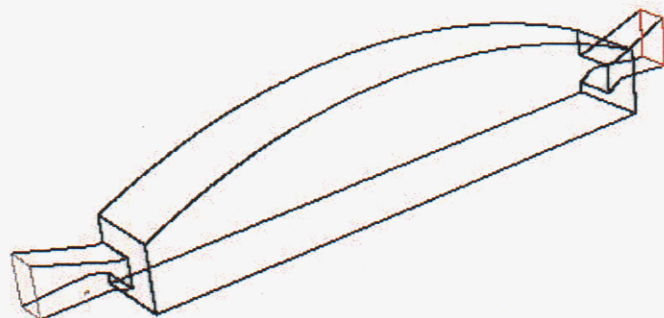
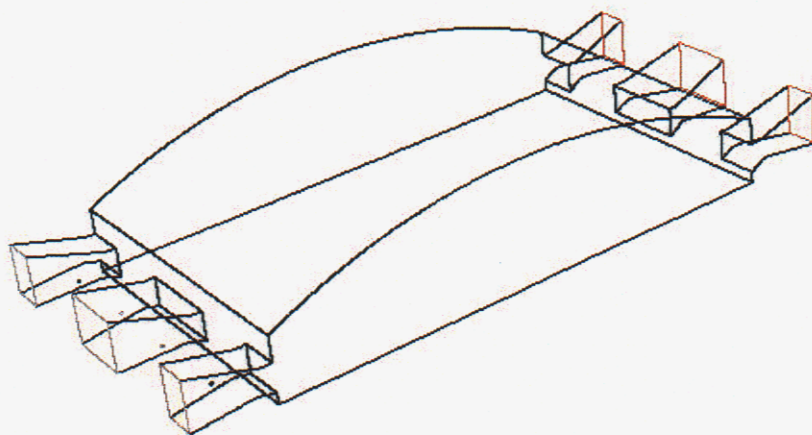Figure 5-2. Schematic of the single-port model for port three.

Figure 5-3. Schematic of the three-port model (Port three is located in the center, port two is towards +ve Z-direction and port four is in the -ve Z-direction).

Table 5-2. Comparison of different models for number of elements in the mesh.

Model	Total no of elements	Elements per port
Single-port	200,000	400,000
Three-port	300,000	150,000
Full furnace	600,000	100,000

The parallel version of Fluent 5.5 (Fluent, Inc.) with 4 processors is used in solving the models. Time-averaged Navier-Stokes equations are solved with a κ-ε model as the closure model for turbulence to predict the flow field. The flame is modeled as a turbulent diffusion flame and the chemical reactions associated with the heat release are assumed to be fast. A beta-function PDF model is used to include the temporal and sub-grid scale fluctuations on scalar properties. Radiation is the dominant form of heat transfer in these furnaces and is accounted for by the use of the Discrete-Ordinate radiation model with variable absorption coefficients based on weighted-sum-of-gray-gases model (WSGGM) (Fluent, Inc.). Soot formation is predicted with two-step Tesner model (Fluent, Inc.) and is included in the prediction of radiation absorption coefficient.

Boundary conditions play a very important role in combustion predictions because of the existence of strong coupling between combustion chamber, melt tank and batch. The glass surface has a distribution of temperature rather than a single constant temperature (Hayes, 1999). Figure 5-4 shows the assumed temperature distribution used in these simulations. It varies linearly from 1810 K in the center to 1760 K on both the sides. The sensitivity of the glass surface temperature distribution is also studied and presented in this report. Similarly, the velocity profile at the inlet influences the amount of mixing and should be included in the model for better predictions. The velocity profile obtained from the experiments for port neck three is used, which is shown in the Figure 5-5. The assumption in this profile is that the velocity does not vary in the horizontal direction (may not be true in practice).

Results and Discussion

Model Comparisons

Temperature Distributions. The temperature distribution in the burner plane for the three different models is shown in Figures 5-6, 5-7, and 5-8. Figure 5-9 shows the temperature contours in planes parallel to YZ at 1.0, 5.5 and 10.0 m in X-direction from the flame-side furnace wall. For three-port and full furnace models, port three is clipped exclusively for burner plane temperature distributions and shown in Figures 5-10 and 5-11. It can be observed from Figure 5-6 that the flame is well defined for single-port model because of the high resolution in the mesh. In order to compare these three models, the average temperatures in the burner plane and on the whole domain over port three are calculated and summarized in Table 5-3. There is a considerable difference in average temperatures between the full furnace model and the other two models. This could be due to the interaction between ports and/or the low-resolution grid in computing.

The dominant reason seems to be the grid resolution because the differences between the single-port and three-port model simulation results are small; yet, the three-port model includes port-to-port interaction effects. This motivates us to design a strategy that could incorporate full furnace effects without sacrificing resolution. One possibility might be to use boundary profiles to exchange information between ports. This strategy will be explored in future work.
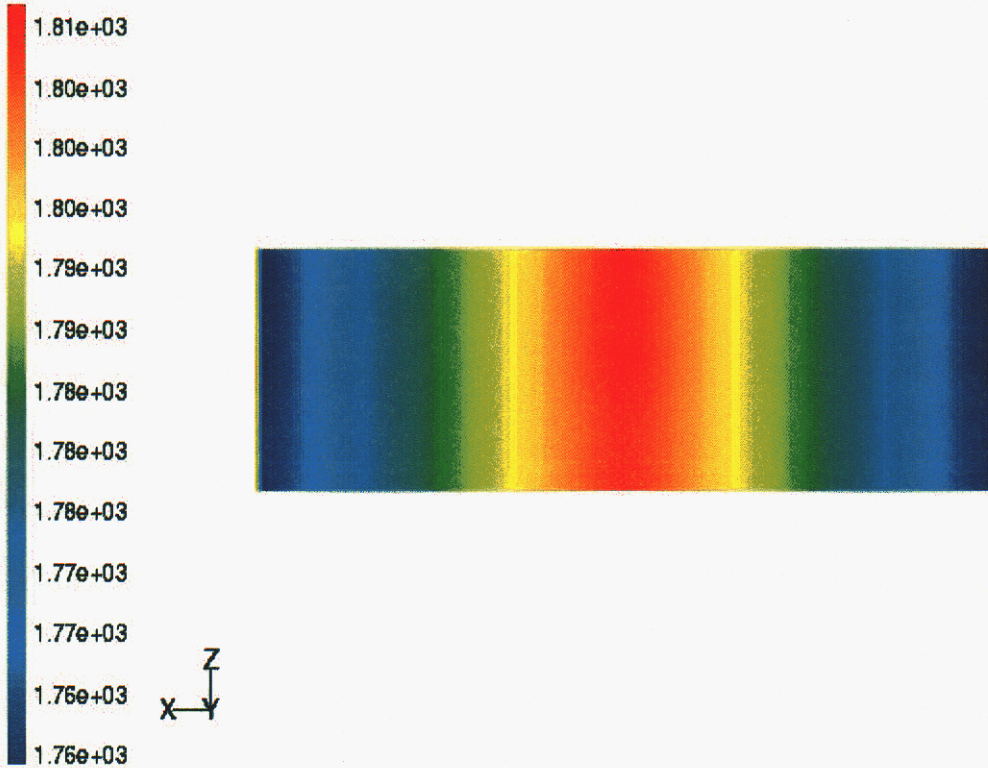
Figure 5-4. Glass surface temperature distribution (assumed) as a boundary condition for combustion model.
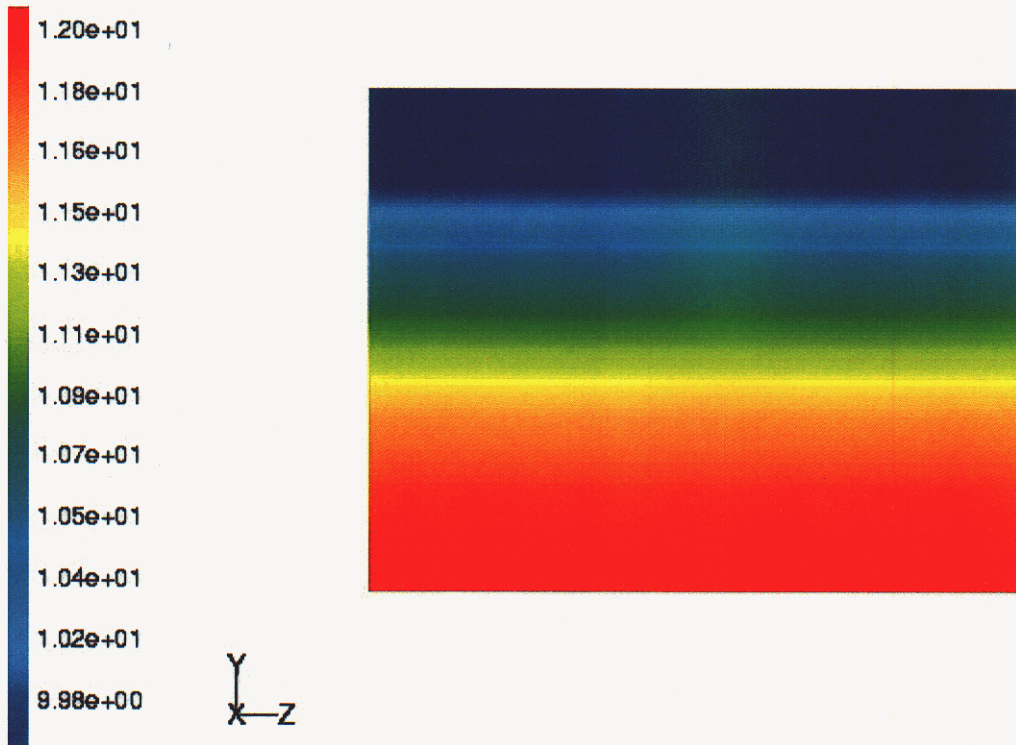
Figure 5-5. Velocity distribution at the inlet for port three (from experiments).

Table 5-3.
Comparison of average temperatures (K) in the burner plane and on the whole domain.

Model	Burner plane	Whole domain
Single-port	1830	1848
Three-port	1823	1855
Full furnace	1720	1745
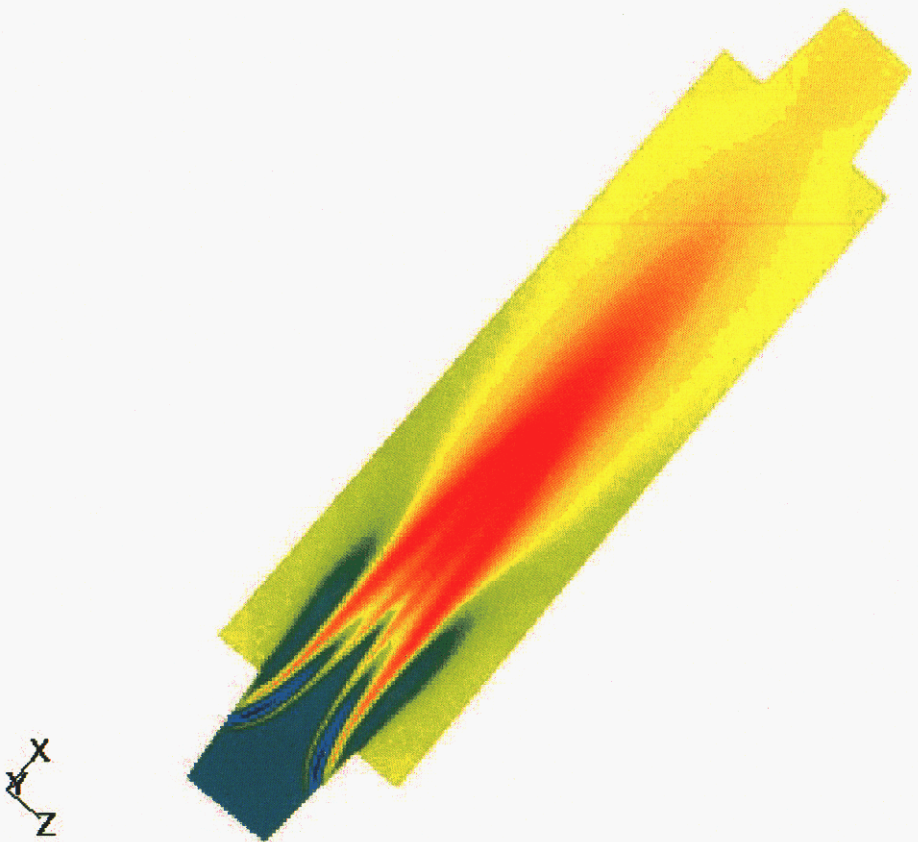
Figure 5-6. Temperature distribution in the burner plane for the single-port model.

2.26e+03
2.14e+03
2.02e+03
1.90e+03
1.79e+03
1.67e+03
1.55e+03
1.43e+03
1.31e+03
1.19e+03
1.08e+03
9.58e+02
8.40e+02

- 43 -
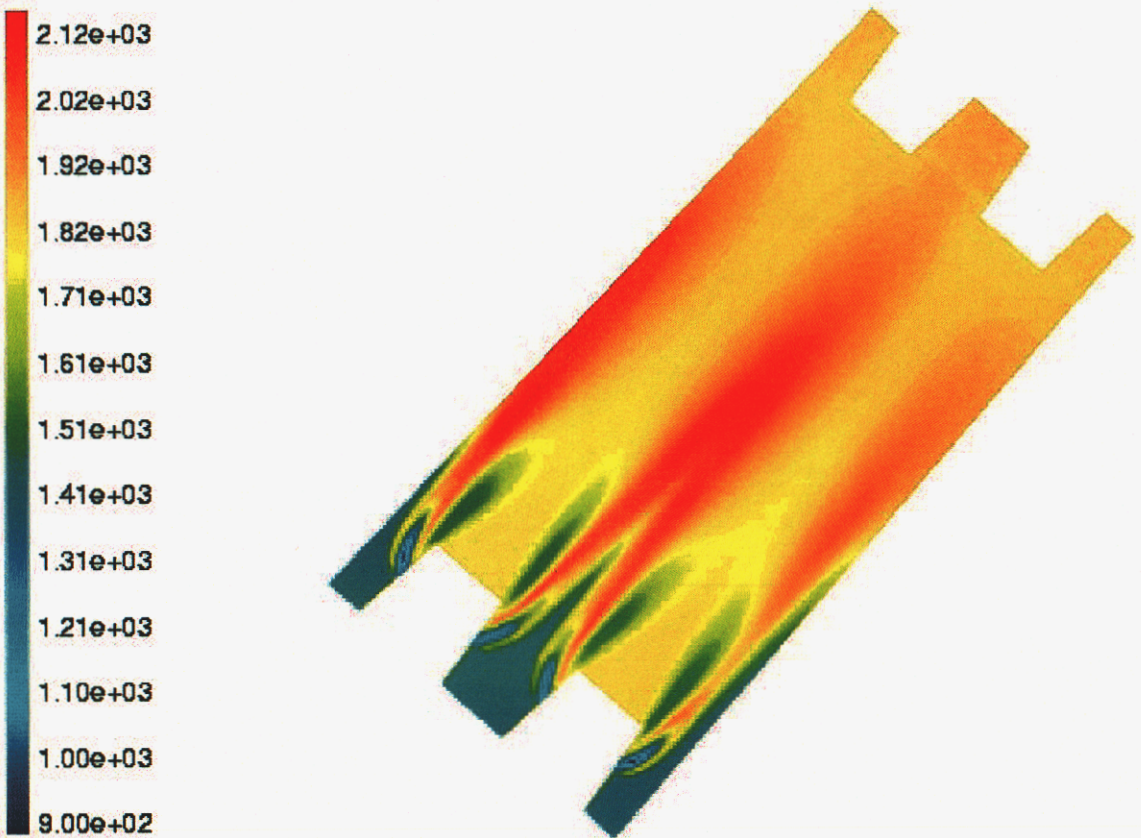
Figure 5-7. Temperature distribution in the burner plane for the three-port model.

- 44 -
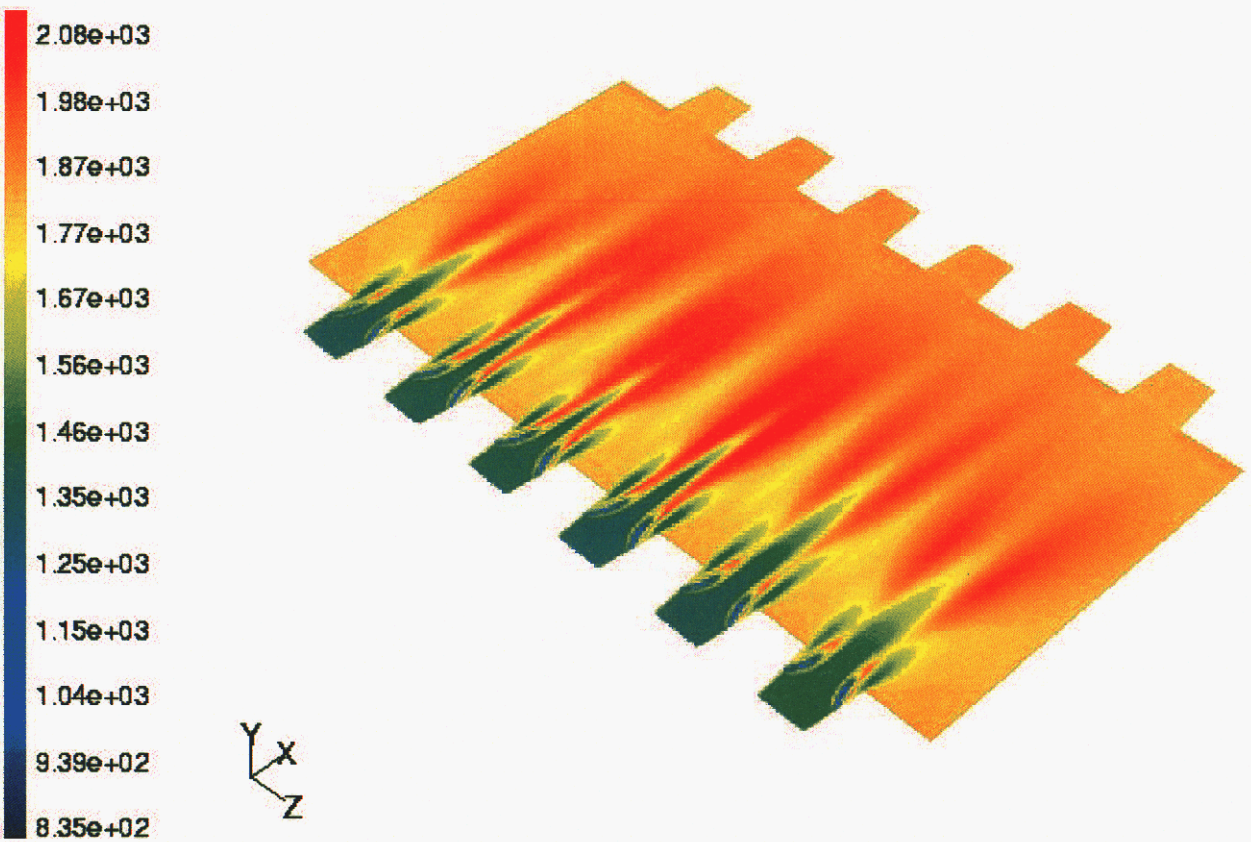
Figure 5-8. Temperature distribution in the burner plane for the full furnace model.
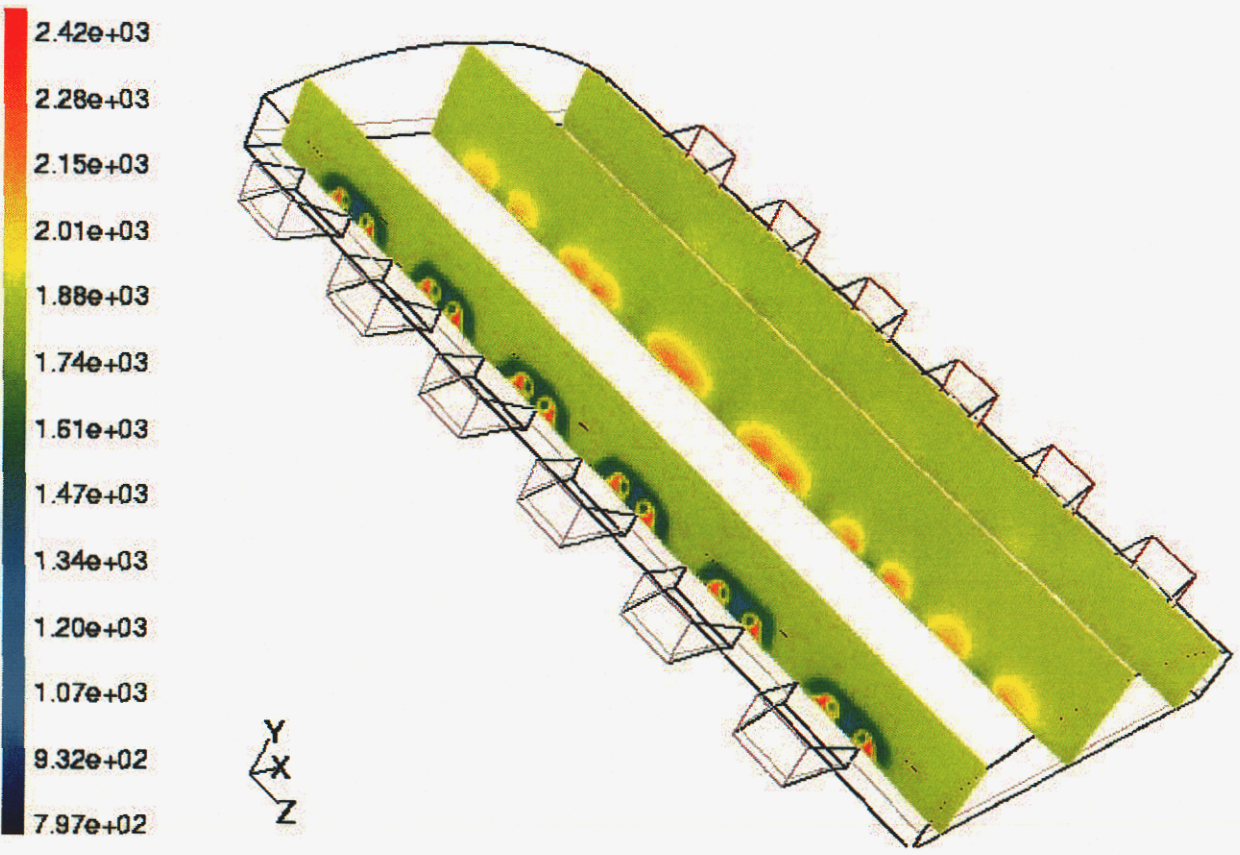
Figure 5-9. Temperature distribution in planes parallel to the Y-Z plane at 1.0, 5.5 and 10.0 m in the X-direction from the flame side furnace wall.
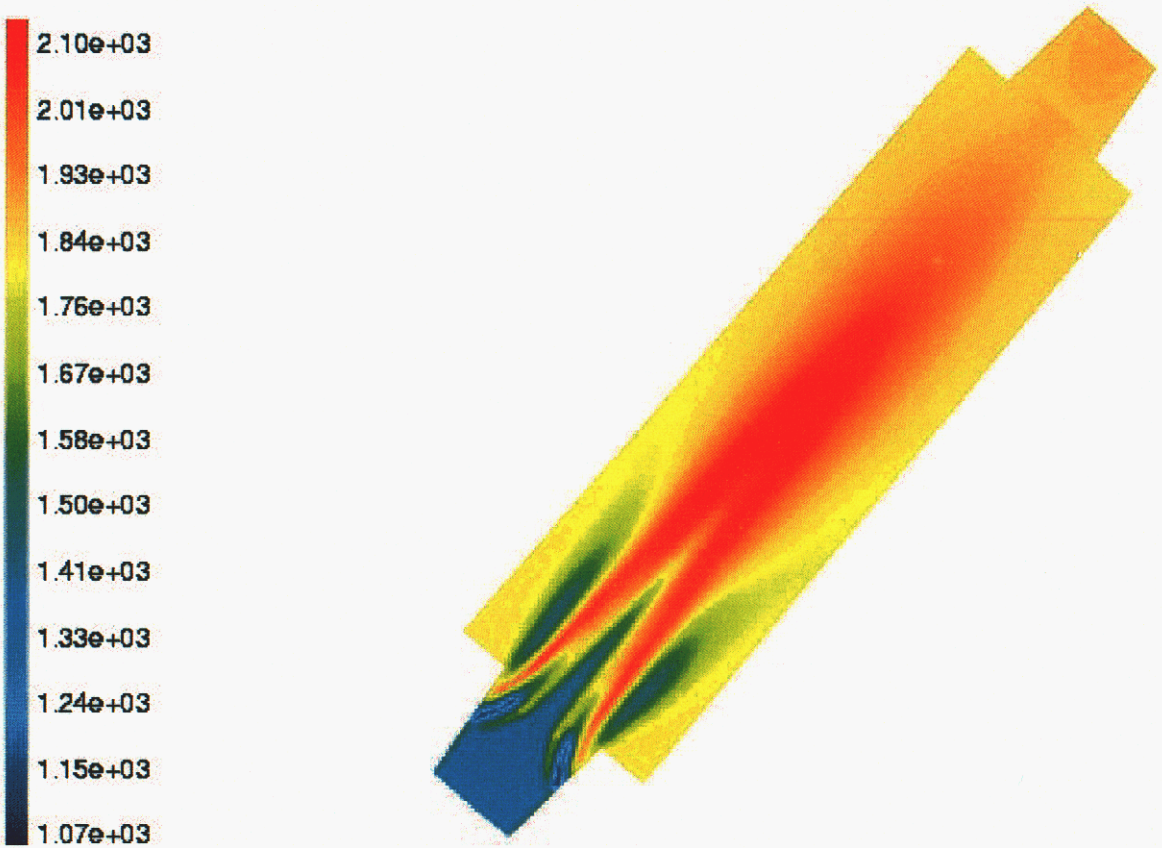
Figure 5-10. Burner plane temperature distributions clipped for port three in the three-port model.

2.10e+03	
2.01e+03	
1.93e+03	
1.84e+03	
1.76e+03	
1.67e+03	
1.58e+03	
1.50e+03	
1.41e+03	
1.33e+03	
1.24e+03	
1.15e+03	
1.07e+03	
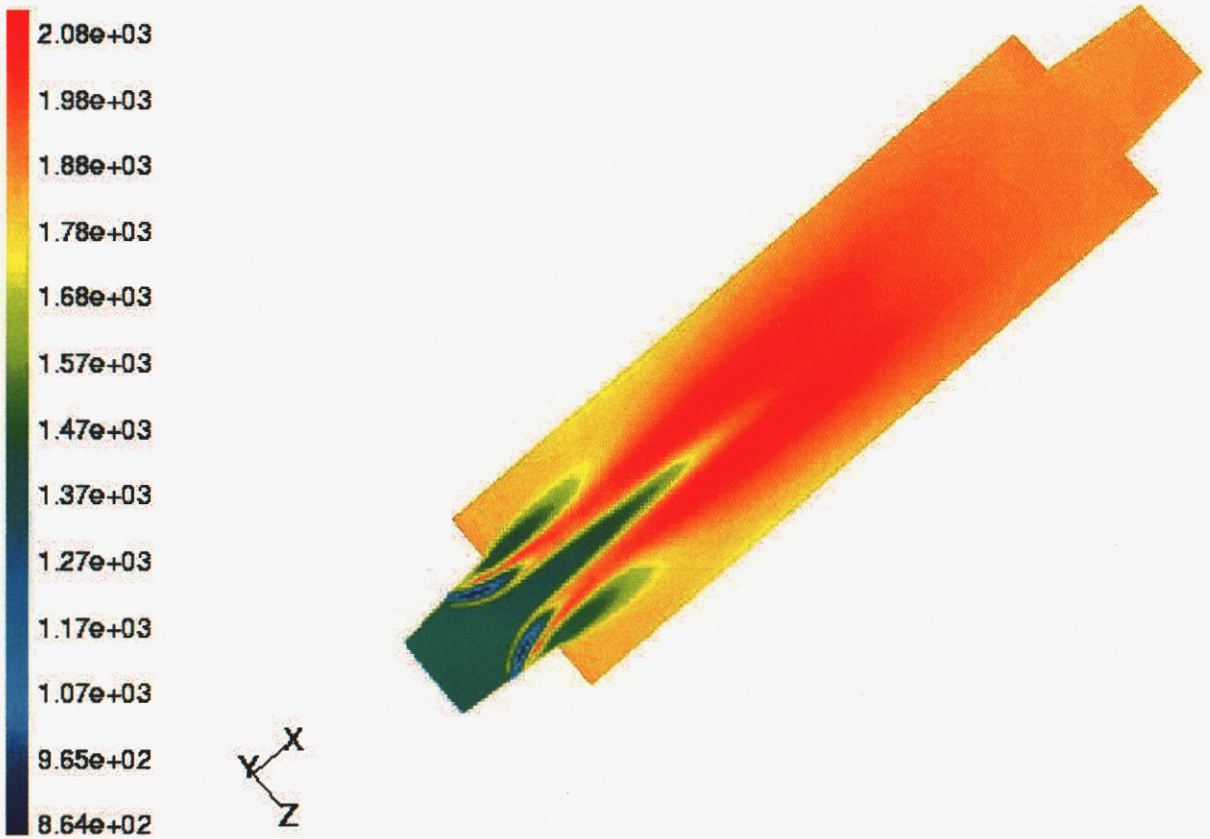
Figure 5-11. Burner plane temperature distributions clipped for port three in the full furnace model.

Comparison of X-Velocity Component. Figures 5-12 and 5-13 compare the X-velocity component for the three models with the experimental data for holes 2 and 5. The maximum velocities are observed near the glass surface in the flame region. The crown region contains a large recirculation zone with negative velocities. This velocity profile decays out to a more uniform profile near the exhaust port. Figure 5-13 shows the velocity profile approximately in the middle of the furnace. The predictions are in reasonable agreement with the experimental data. There is little variation between the different models, except near the flame.
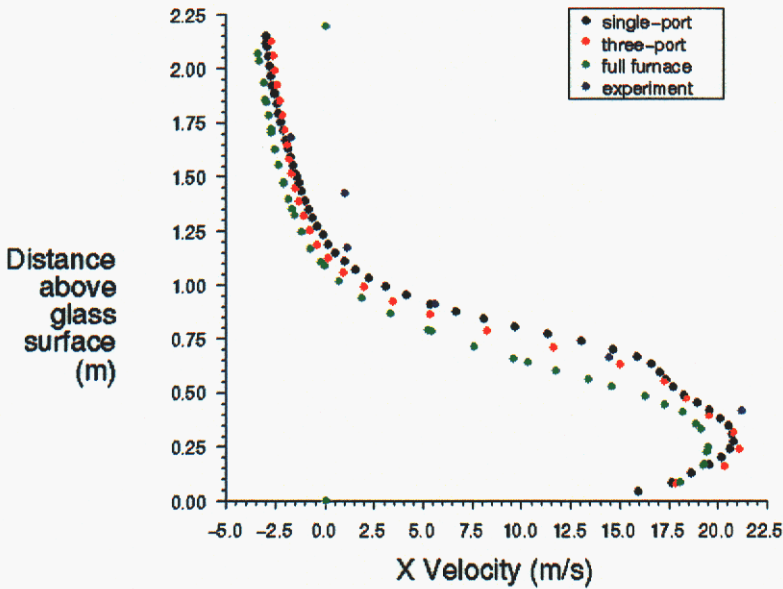
Figure 5-12. X-velocity component for hole 2, located at 2.3 m from the flame-side wall.

Comparison of Temperatures. Figure 5-14 shows the comparison of calculated and experimental temperature profiles for hole 1. There are only limited experimental data available for this location. There are no experimental data in the flame region. All three models agree above 1 m from the glass surface. This region has a constant low gradient and can be modeled with a low-resolution mesh. Figure 5-15 shows the temperature data for hole 2. It can be observed that none of the model predictions match the measured temperatures in the flame region. There is a huge variation in the predictions between different models. This emphasizes the importance of resolving the flame region, both in terms of grid and physics. Large eddy simulations are necessary to resolve the important mixing phenomena and will be explored in future work.
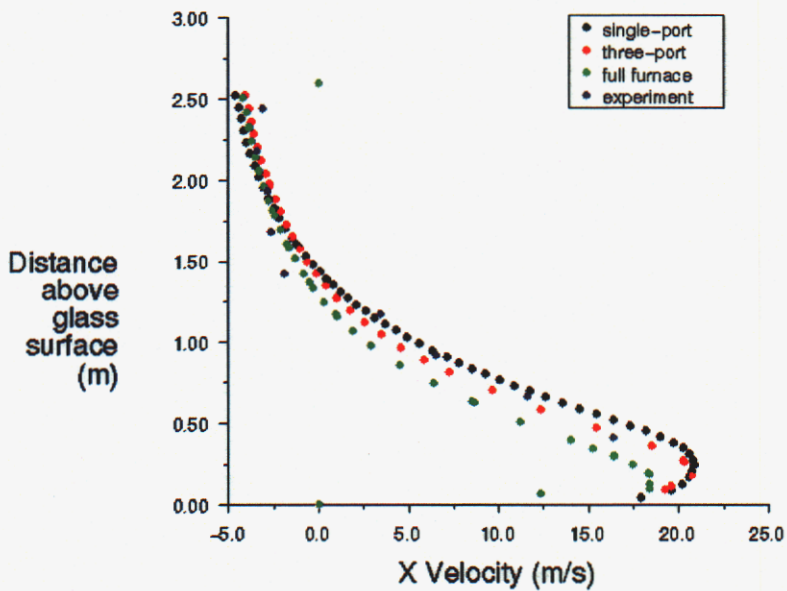
Figure 5-13. X-velocity component for hole 5, located at 5.3 m from the flame-side wall.
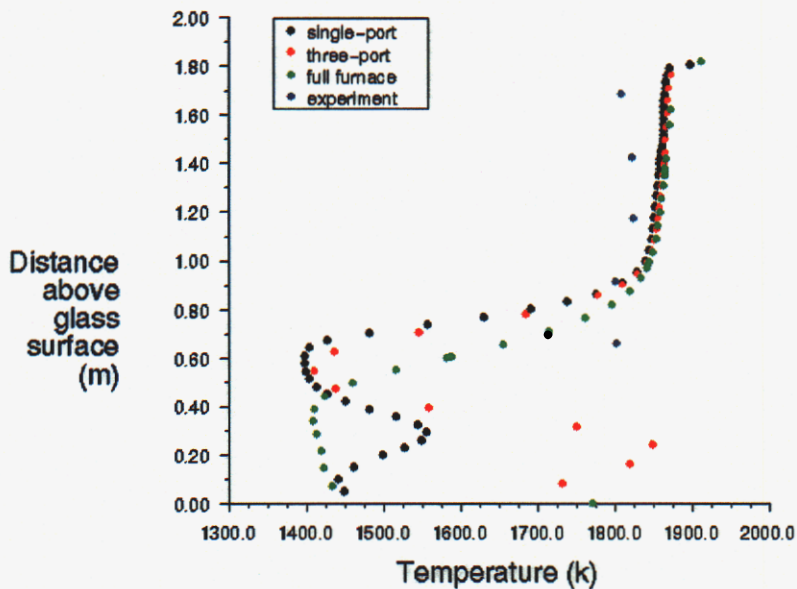
Figure 5-14. Temperature profile for hole 1, located at 1.1 m from the flame-side wall.
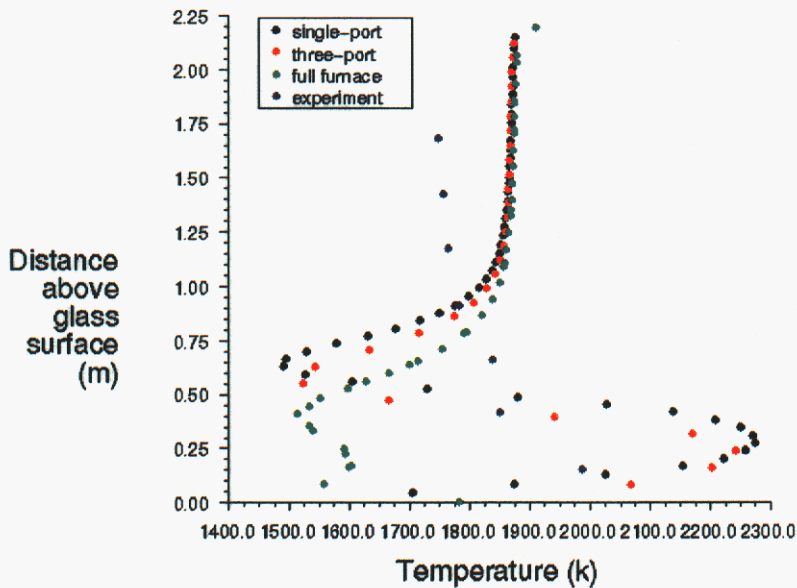
Figure 5-15. Temperature profile for hole 2, located at 2.3 m from the flame-side wall.

The measured flame region temperatures are not in agreement with even the fine mesh. We hypothesize that the reason for this discrepancy may be one or more of the following:

1. Inaccurate airflow rates at the port neck.
2. Inadequate turbulent mixing model.
3. Inadequate computational resolution.
4. Inadequate measured data.

We will address each of these. As an important first step we recommend that the PPG/Sandia/University of Utah team obtain air and fuel rates to each port and burner.

Comparison of Species Concentrations. Figures 5-16 and 5-17 compare the mole fractions of O_2 and CO_2 respectively for different models with the experimental data. The predicted species levels deviate highly from those measured. These discrepancies are consistent with the hypothesized reasons for temperature discrepancies. The predictions for different models did not vary much from 1.0 m above the glass furnace to the crown. We feel it is imperative to resolve the in-flame discrepancies for temperature and major species if we hope to get reasonable NO_X predictions. It has also been suggested that CO_2 released from batch melting process may be contributing to the high amounts predicted by the models.
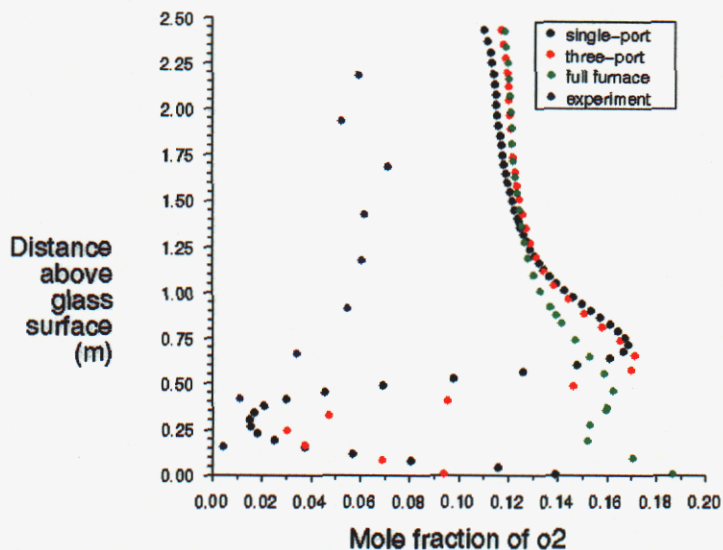
Figure 5-16. Mole fraction of O_2 for hole 3, located at 3.4 m from the flame-side wall.
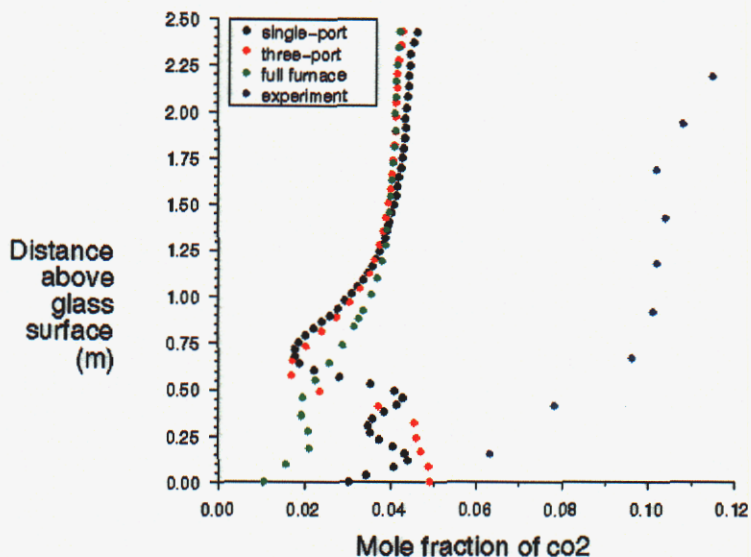
Figure 5-17. Mole fraction of CO_2 for hole 3, located at 3.4 m from the flame-side wall.

Mass Flow Distribution. The full furnace model is also analyzed for the mass flow distributions in the inlet and exhaust ports. Since the flow is fully three-dimensional in the glass furnace, the amount of mass entering into a particular inlet port does not exit from the same exhaust port (that is opposite to the inlet) and Table 5-4 shows the

distribution of mass between the individual ports. From our analyses of simulations to date, we conclude that this redistribution of exit gases is the major port-to-port interaction. No significant asymmetry has been observed in the flame region due to port-to-port interaction.

Table 5-4. Distribution of mass flow rates among the individual ports.

	Port 1	Port 2	Port 3	Port 4	Port 5	Port 6
Mass in (kg/s)	4.4665	4.1435	4.0499	3.2857	3.8417	3.7813
Mass out (kg/s)	3.9254	4.1149	3.8738	3.9592	4.0495	3.6454

Sensitivity Study

Glass Surface Temperature. In order to find the sensitivity of the simulations to the glass surface temperature boundary condition, four different tests are conducted with the single-port model and are numbered from 1 to 4. Test 1 uses the surface temperature distribution as shown in the Figure 5-4, with an average of 1785 K. Test 2 uses a constant temperature of 1785 K throughout the boundary. Test 3's temperature distribution varies linearly from 1760 K at the center of the furnace to 1810 K at the side walls, with an average of 1785 K. The surface temperature for the Test 4 is kept constant at 1885 K. The objective of this study is two fold: 1) to find the sensitivity of different temperature distributions by keeping constant average value, and 2) to study the effect of changing the boundary temperature values. For all these cases, the average temperatures over the burner plane and on the whole domain are calculated and tabulated in Table 5-5.

Table 5-5.
Comparison of average temperatures in the burner plane and on the whole domain for different glass surface temperature boundary conditions.

Sensitivity Test	Average Temperature (K)	
	Burner plane	Whole domain
Test 1	1830	1849
Test 2	1830	1849
Test 3	1831	1850
Test 4	1870	1894

It can be observed from Table 5-5 that the side-to-side profile of the surface temperature distribution has no effect on the temperature predictions. But, increasing the value up to 100 K resulted in an increase of 40 K in the burner plane and 45 K in the whole domain. We conclude that knowing an average glass surface temperature along

the length of the furnace (from batch to melter end) is important to the simulation for obtaining combustion temperatures. However, the temperature profile of the glass surface in between the sides is not significant to the simulation results.

Inlet Air Flow Rates. The simulation results from the previous section showed model results with higher values of O_2 in the combustion space than experimentally measured (i.e. see Figure 5-16). This may be due to uncertainty in the specified inlet air flow rates in the model. For example, although the vertical velocity profile was measured in the port neck, the horizontal profile was assumed to be uniform, thus establishing a total mass flow rate for the inlet air. To study the sensitivity to inlet air flow rates, simulation results from three models with different air flow rates are compared with experiments for flow, temperature and species. Fuel flow rates are not changed in this study. Thus, as the air flow rate is decreased, the overall equivalence ratio increases. The sensitivity study is performed with equivalence ratios of 0.8 and 1.0. These results are compared with the previous model results which had an overall equivalence ratio of 0.66. All three models are compared with the experimental data. In this study, only the magnitude of velocities in vertical direction is changed (by keeping the measured vertical profile), while maintaining a flat velocity profile along the horizontal direction.

Figures 5-18 and 5-19 compare the X-velocity components from the three models with experimental data. It can be observed that the flame-zone velocities are more sensitive to the air flow rates than other regions of the flow. Also, the velocity profile in the flame-zone becomes flat with increasing equivalence ratios and decreasing air flow rates.
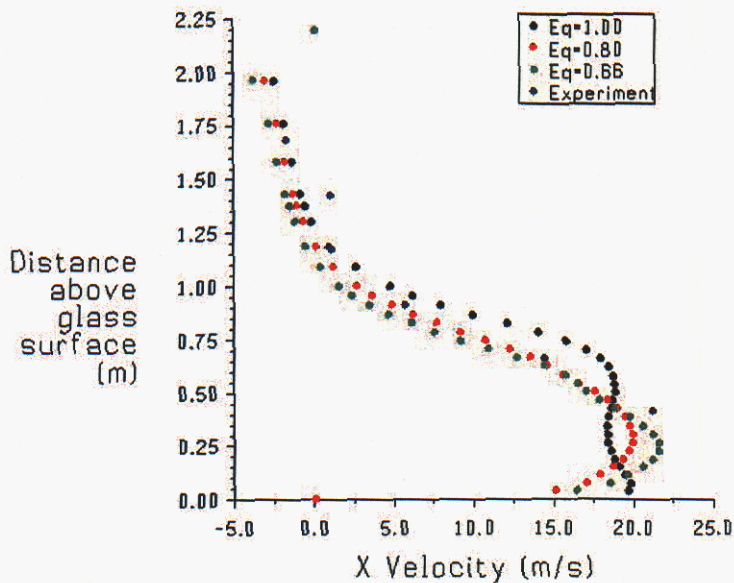

Figure 5-18. X-velocity component at hole 2 for different air flow rates (equivalence ratios).
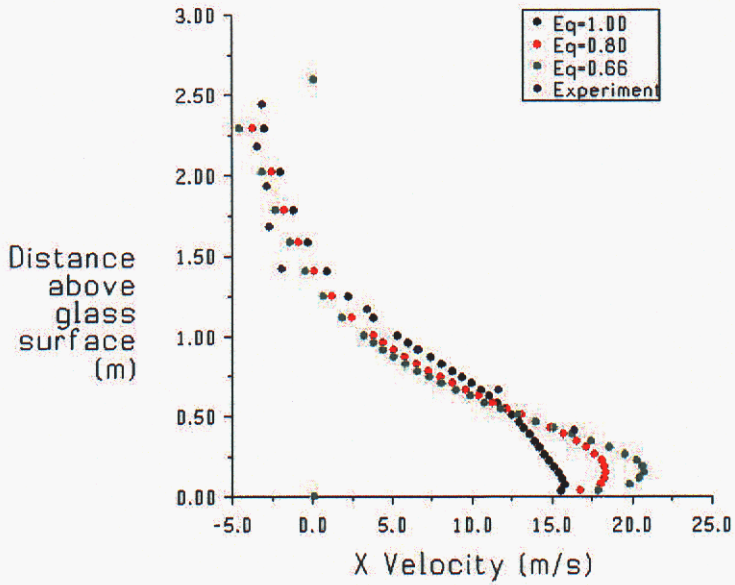
Figure 5-19. X-velocity component at hole 5 for different air flow rates(equivalence ratios).
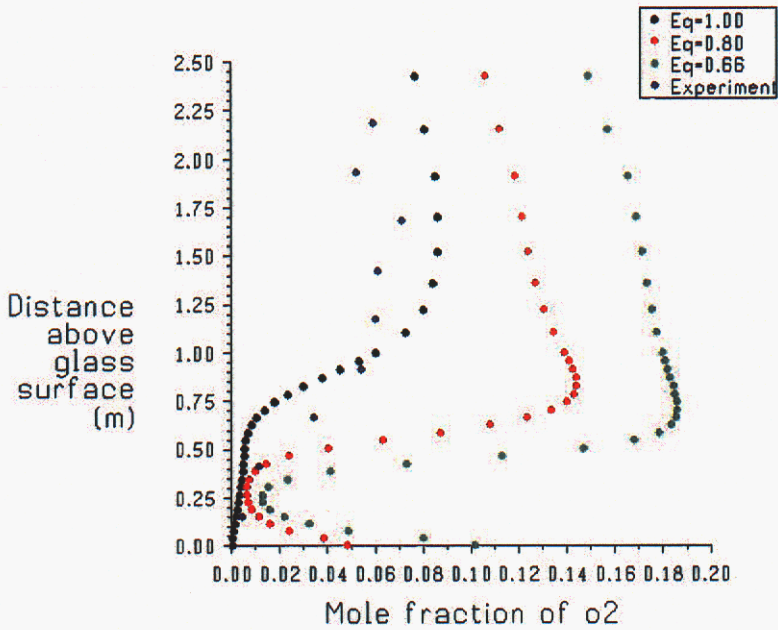
Figure 5-20. Mole fraction of O_2 at hole 3 for different air flow rates (equivalence ratios).
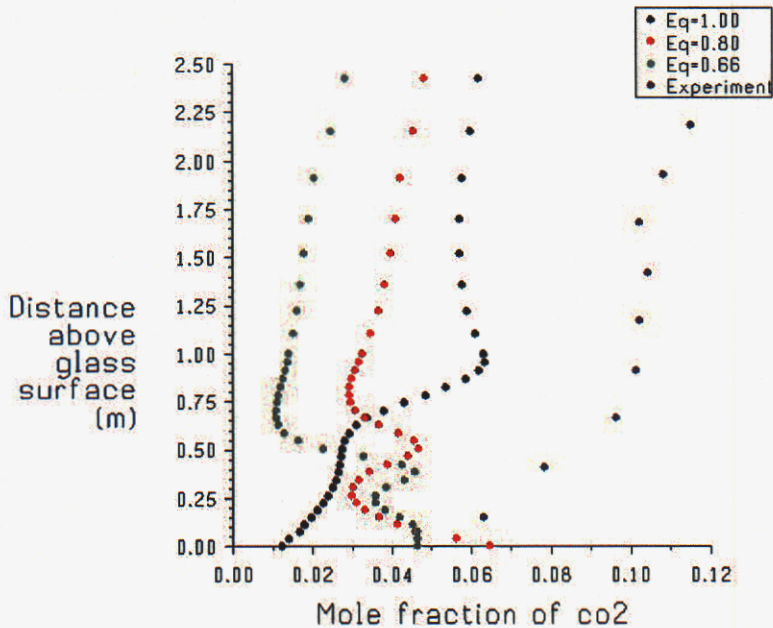
Figure 5-21. Mole fraction of CO_2 at hole 3 for different air flow rates (equivalence ratios).

The sensitivity of the mole fraction of O_2 is shown in Figure 7-20. O_2 predictions improve as the equivalence ratio increases. Consistently, the CO_2 predictions also follow this trend and are shown in Figure 5-21. Higher values of measured CO_2 are due to contributions from batch, which is typically about 4% in a glass furnace.

Figure 5-22 shows the temperature profile at hole 2 for different amounts of inlet air. Temperature predictions are very sensitive to the inlet air boundary condition, especially in the flame region. In order to get reasonable predictions, specification of the correct amount of air is mandatory. The wide discrepancies in the flame region can be better explained by the local mixture fraction shown for hole 2 in Figure 5-23. In this case, the stoichiometric mean mixture fraction is 0.09. Peak flame temperatures occur when the local mean mixture fraction reaches this value. Rich and lean mixture fractions result in lower flame temperatures. For the case where the overall equivalence ratio is 0.66, the local mixture fraction reaches the stoichiometric value only once and the remaining flame-zone is lean. The entire flame-zone is rich in the case where the overall equivalence ratio is 1.0. All the three regions i.e. lean, rich and stoichiometric can be observed in the flame region for an overall equivalence ratio of 0.8.

It is very difficult to compare the results of these different models with the experimental results since not much data is available in the flame region. The validity of the available experimental data in the flame region is also under question. Obtaining these kinds of data in large-scale industrial glass furnaces is extremely difficult.
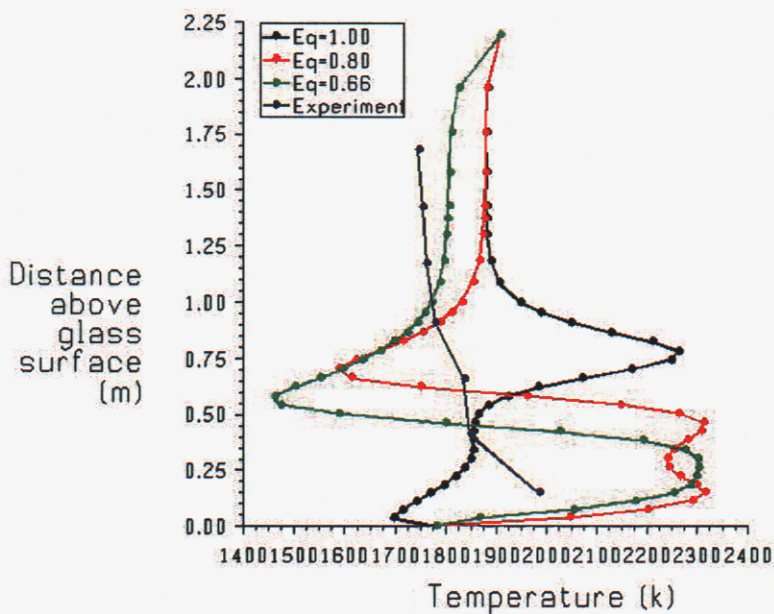
Figure 5-22. Temperature profile at hole 2 for different air flow rates (equivalence ratios).
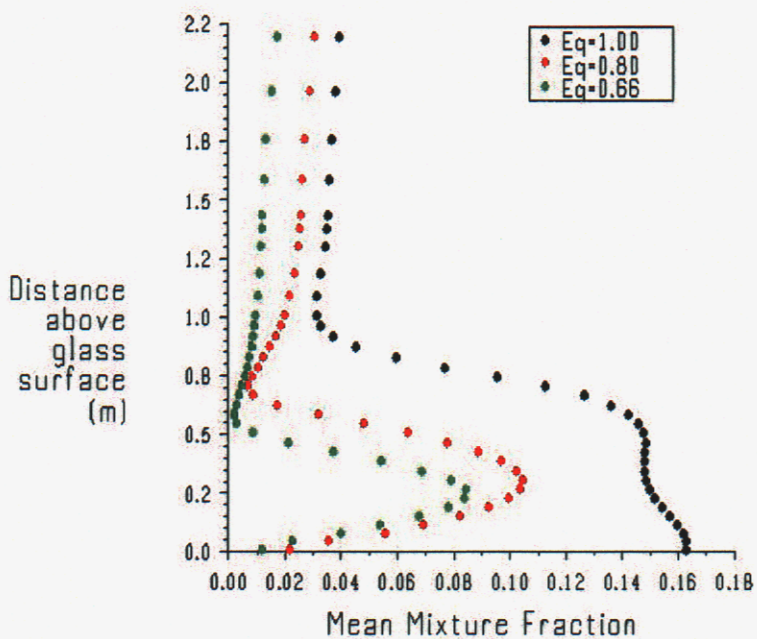
Figure 5-23. Mixture fraction at hole 2 for different air flow rates (equivalence ratios).

**Inlet Air Profile.** The objective in performing this sensitivity study is to find out the effect of the inlet air profile on the model predictions by keeping the total amount of inlet air at a constant value. Two different cases with equivalence ratio of 0.80 are studied, one with constant horizontal profile and the other with variable horizontal profile. The inlet profiles for both the cases are shown in Figure 5-24. In the case with a constant horizontal profile, the magnitude of the vertical component of the inlet air velocity is scaled to obtain the required air flow rate. In the case of a variable horizontal profile, the measured vertical component is not changed; instead the correct air flow rate is imposed with a profile in the horizontal direction. It should be noted that the colors in Figure 5-24 do not represent the same scale. The total air flow rate is the same in both cases.
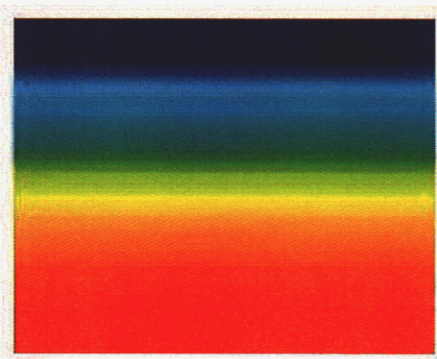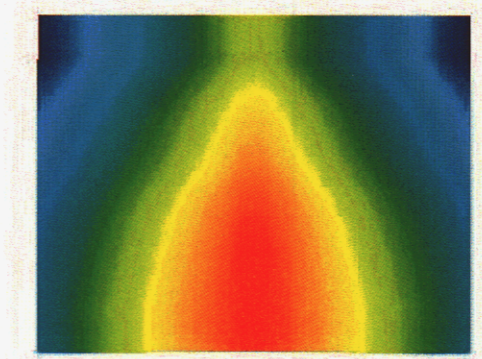
a. Constant horizontal profile.   b. Variable horizontal profile.

Figure 5-24. Inlet air profiles.

The X-velocity component is compared to the experimental data for these two different cases and is shown in Figures 5-25 and 5-26. The influence of the horizontal profile is observed only in the initial part of the flame. Its influence decays towards the end of the flame. There is no influence of the profile in the recirculation zone. Mole fractions at hole 3 for O_2 and CO_2 are shown in Figures 5-27 and 5-28 respectively. Not much difference is observed for different inlet air profiles except in the region between the flame and the glass surface. Discrepancies between experiments and predictions in this region could be either due to the inlet velocity profile or due to unresolved physics as discussed in the next section. Temperature and local mean mixture fraction profiles for hole 2 are shown in Figures 5-29 and 5-30 respectively. The trend is similar to that for the species and the discrepancies between experiments and predictions in the flame region can be explained by the same analysis proposed above. From this study, it can be concluded that the inlet air profile is not as crucial as the inlet air flow rates for model predictions.
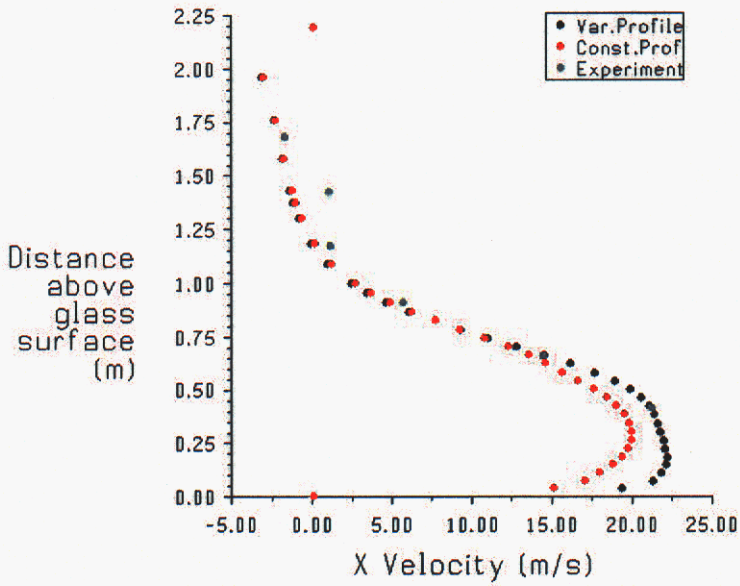
Figure 5-25. X-velocity component at hole 2 for different inlet air profiles.
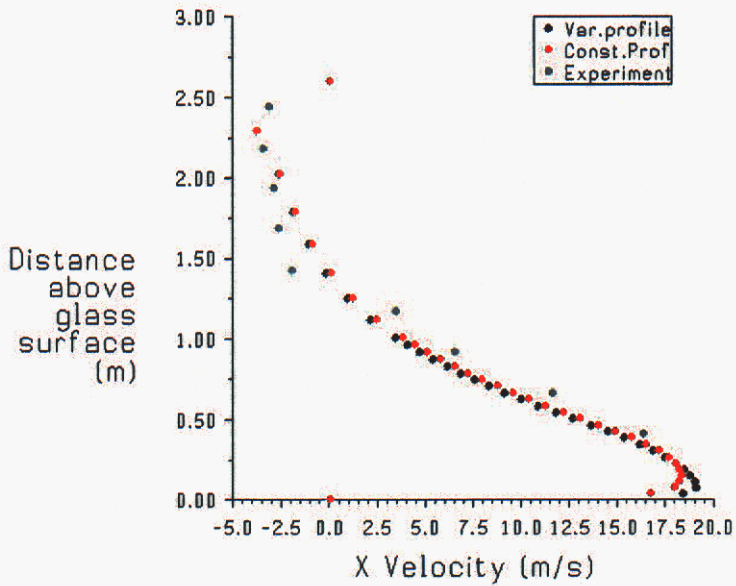
Figure 5-26. X-velocity component at hole 5 for different inlet air profiles.
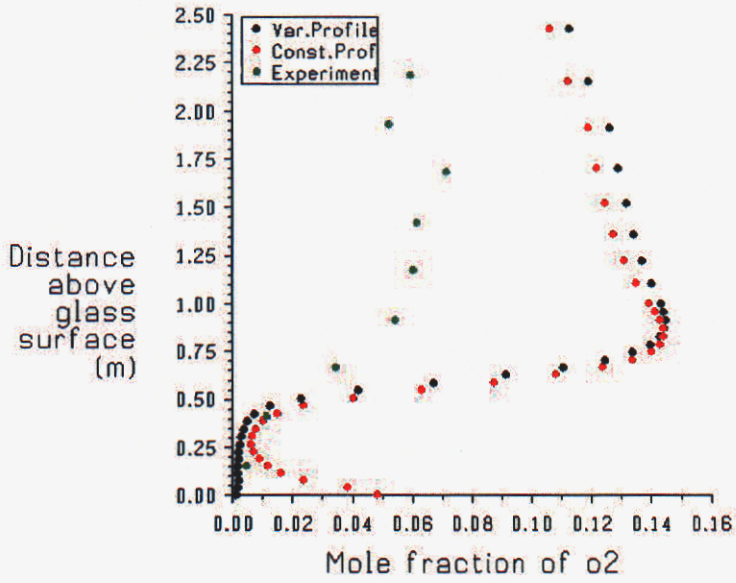
Figure 5-27. Mole fraction of O_2 at hole 3 for different inlet air profiles.
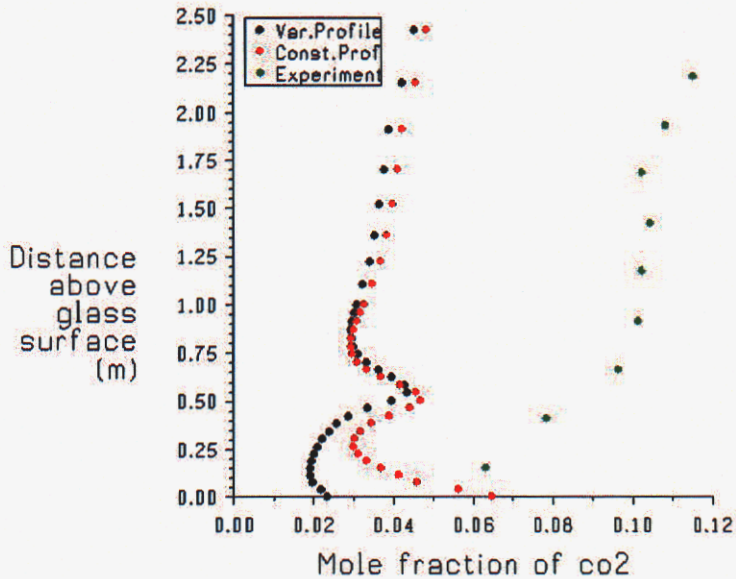
Figure 5-28. Mole fraction of CO_2 at hole 3 for different inlet air profiles.
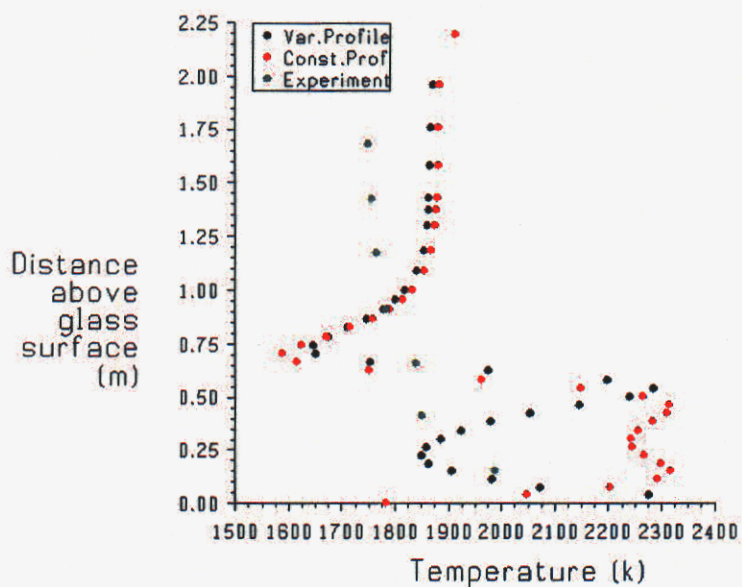
Figure 5-29. Temperature profile at hole 2 for different inlet air profiles.
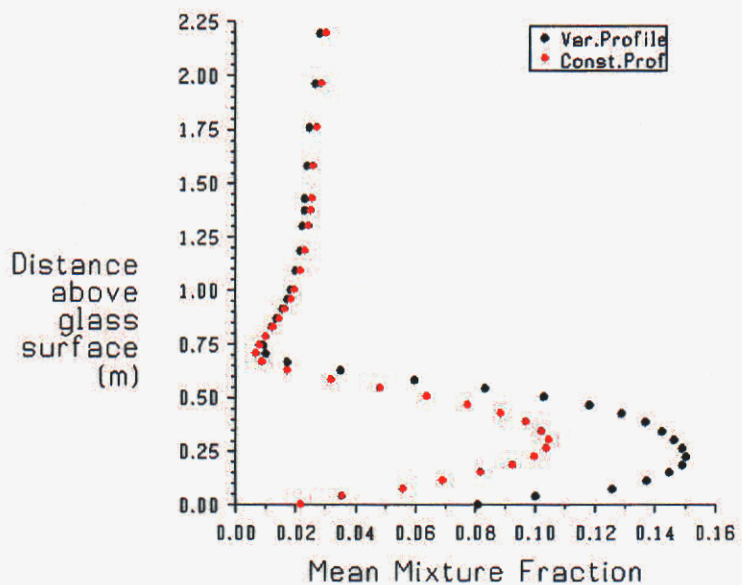
Figure 5-30. Mean mixture fraction profile at hole 2 for different inlet air profiles.

Mixing Resolution.   In simulating non-premixed combustion, resolving the mixing of fuel and air is very important for capturing the physics and chemistry of the process. Often this task is severely constrained by the wide disparity of geometrical scales present in large-scale industrial furnaces. To resolve all these scales together requires enormous computational resources and may not be practical. To circumvent this difficulty, mixing is finely resolved in a calculation for the individual port necks and this information is used as the boundary condition for calculations in the furnace. In order to study the sensitivity of mixing resolution, two different tasks are carried out. One task is to compare two cases with different resolutions for mean mixture fraction, mixture fraction variance, flow field and temperatures in the port neck. Another task is to compare the flow, temperature and species fields with the experimental data inside the furnace.

Individual port necks are solved with two different grid resolutions. The base case has nearly 30,000 computational cells and the high resolution case has approximately 180,000. Velocity vectors are plotted at the outlet of the port neck and are shown in Figure 5-31. It can be noticed that the high resolution case captured more details in the flow field. This improved velocity field significantly improves the simulation of mixing phenomena. Figure 5-32 shows the temperature, mean mixture fraction and mixture fraction variance profiles for base and high resolution cases at the end of the port neck. Since coarse grids are numerically too diffusive, the scalar gradients driving the mixing phenomena are not captured to the level that is needed for reliable predictions. The high resolution mesh better resolves these gradients. These comparisons show the importance of resolving mixing process. In order to capture the temporal variations in mixing, large eddy simulations are necessary.

To study the effect of this resolved mixing on combustion predictions in the furnace, simulations are performed for the furnace with this data as the input boundary condition. Comparisons are made between the base case results and the experimental data.

a. Base case   b. High resolution case
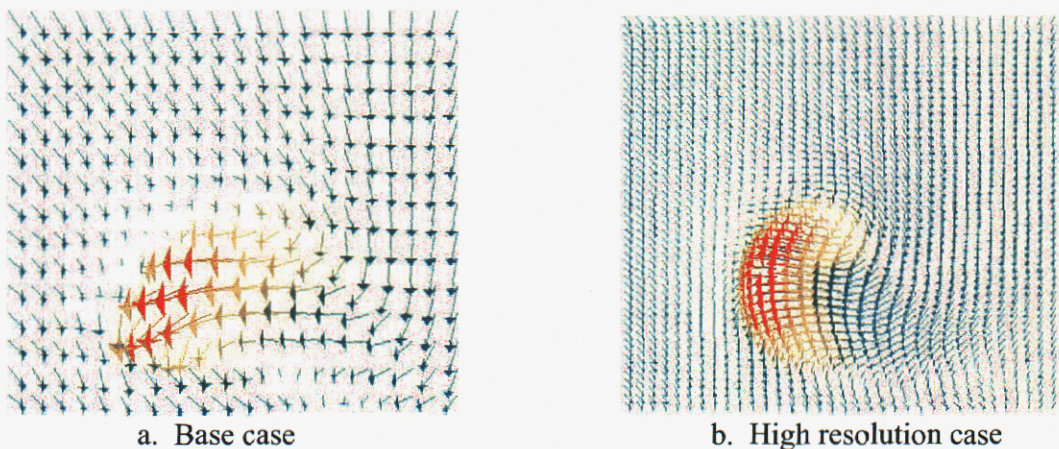
Figure 5-31. Flow field comparison for different grid resolutions in the port neck.

f

T

σ_f^2

a. Base case   b. High resolution case
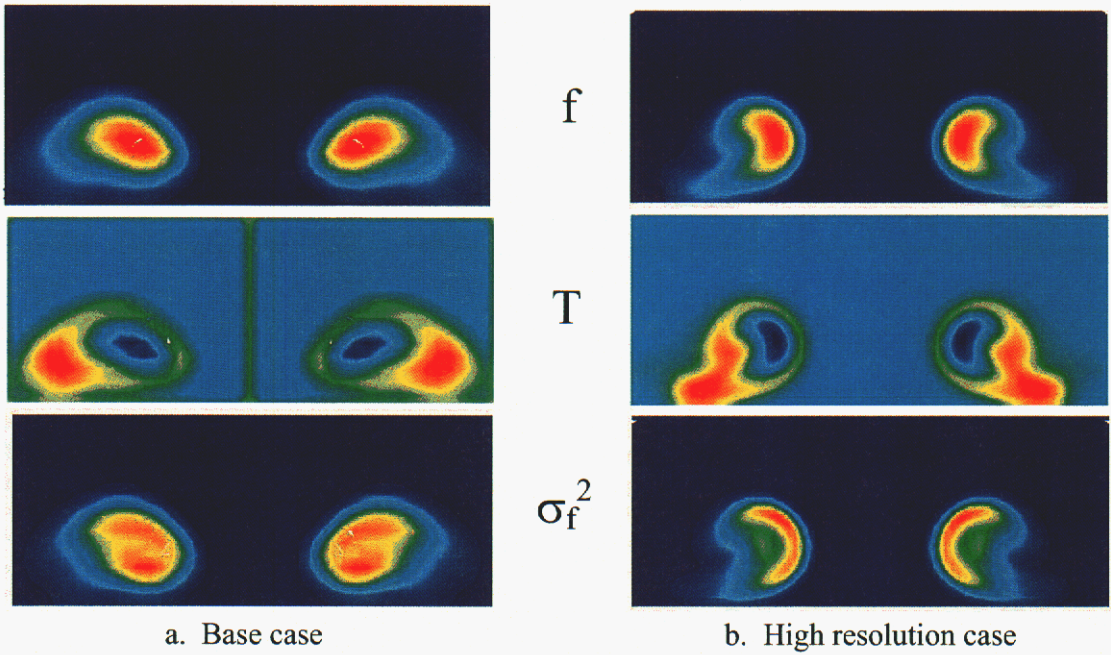
Figure 5-32. Effect of grid resolution in the port neck on mixing, energy.
f: Mean mixture fraction
T: Temperature
σ_f^2: Mixture fraction variance

From the velocity data shown in Figures 5-33 and 5-34, there is considerably good agreement between the base & high resolution cases compared with the experimental data. Figures 5-35 and 5-36 compare the mole fractions for O_2 and CO_2 respectively at hole 3. There is a substantial improvement in the species predictions when the mixing is resolved with fine grids. The predicted O_2 and CO_2 mole fractions are almost equal to the results from previously studied equivalence ratio of 0.80 case with lower resolution. Although the equivalence ratio used in this case is only 0.66. The temperature profile and local mean mixture fraction are shown in Figures 5-37 and 5-38 for hole 1. Since not much inflame temperature data is available, it is very difficult to compare the sensitivity of predictions in the flame region for different resolutions. But, there are even some differences in the temperature and mixture fraction values in the region of the furnace higher than 1.0 m above the glass surface. This suggests that mixing resolution is very important for better temperature predictions too.
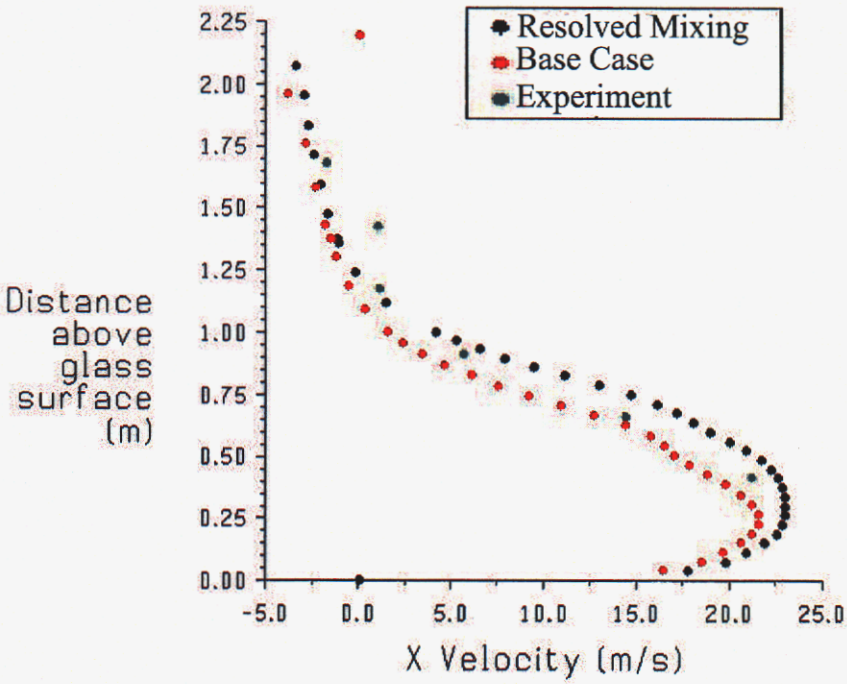
Figure 5-33. X-velocity component at hole 2 for different port neck resolutions.
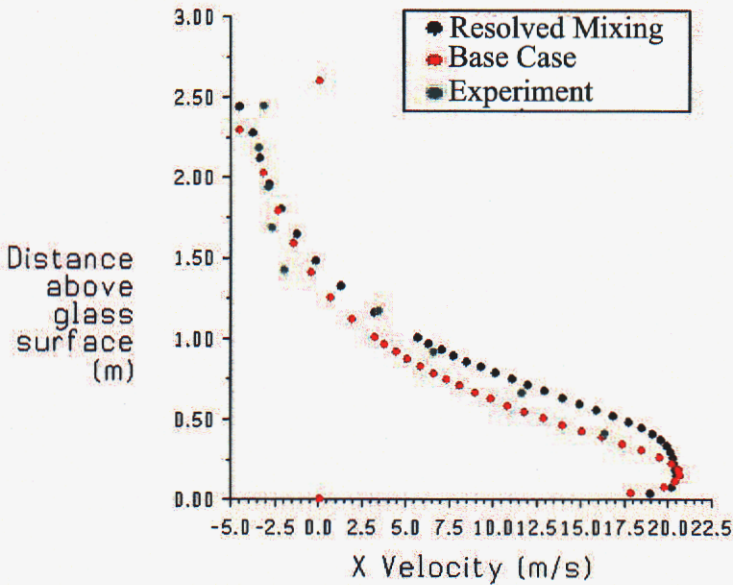
Figure 5-34. X -velocity component at hole 5 for different port neck resolutions.
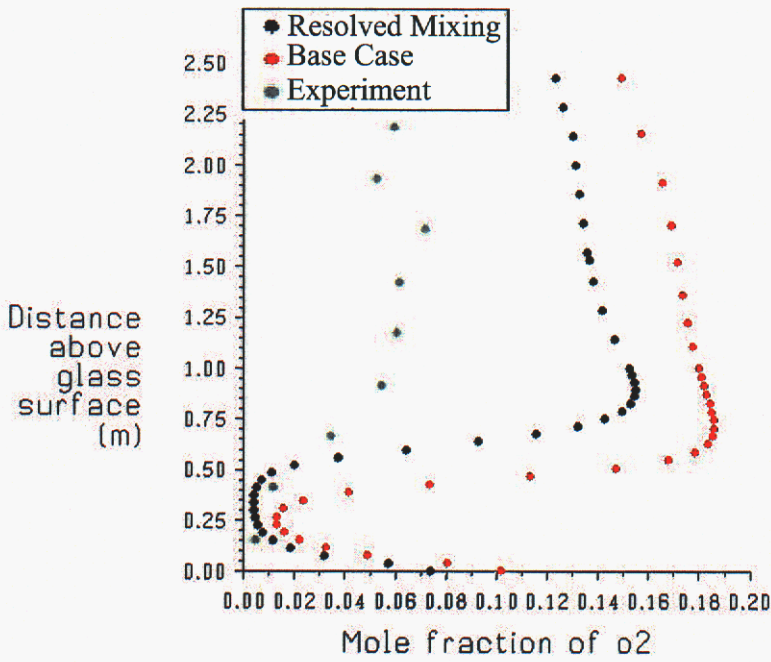
Figure 5-35. Mole fraction of O_2 at hole 3 for different port neck resolutions.
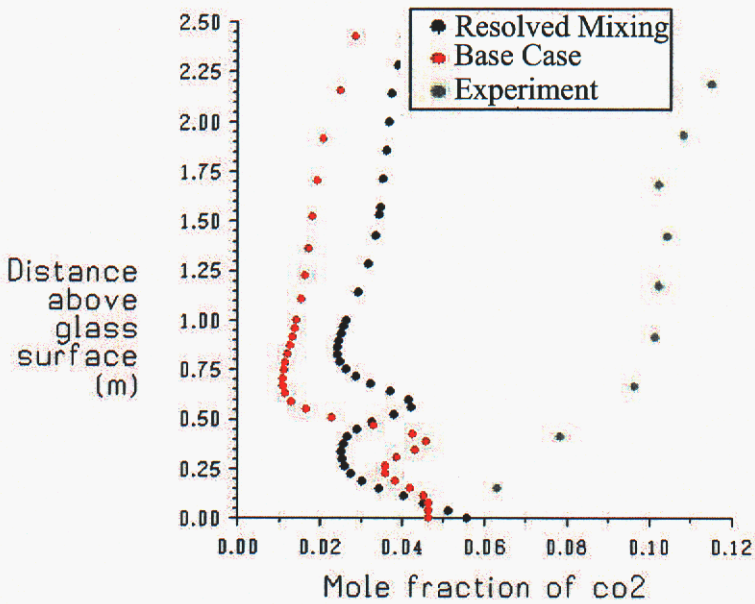
Figure 5-36. Mole fraction of CO_2 at hole 3 for different port neck resolutions.
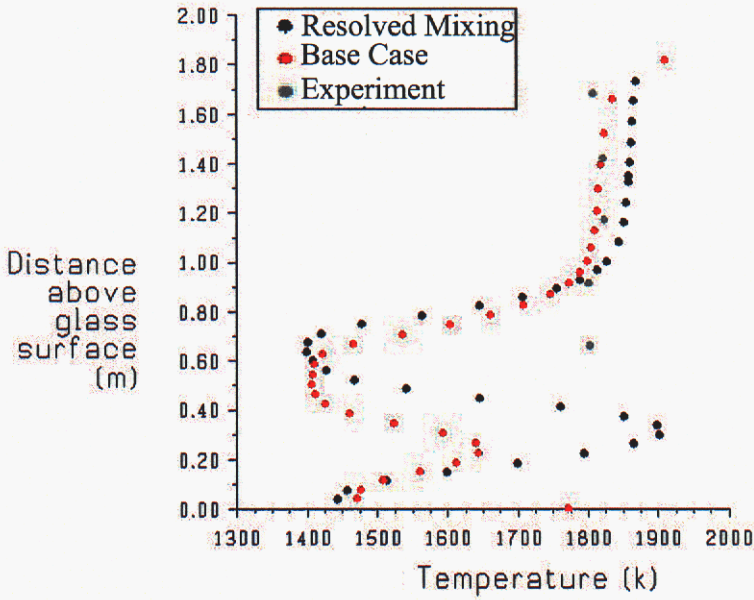
Figure 5-37. Temperature profile at hole 1 for different port neck resolutions.
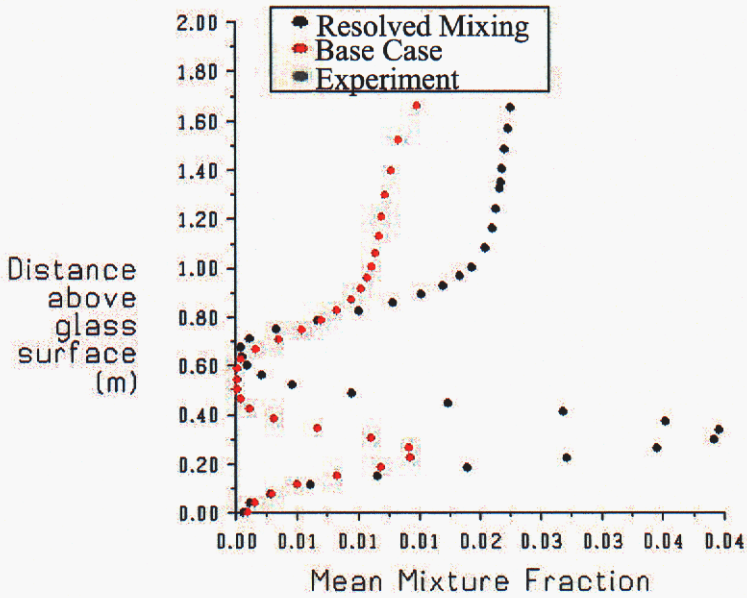
Figure 5-38. Mean mixture fraction profile at hole 1 for different port neck resolutions.

**Crown Temperature.** In order to find the sensitivity of the crown temperature to temperature predictions in the burner plane and in the whole furnace, two different cases are studied. One case used a constant crown temperature, which is 1910 K, measured with experiments and another case is with an assumed temperature distribution such that the average temperature on the crown is equal to the first case. Temperatures in the burner plane and in the whole furnace are averaged and tabulated in Table 5-6. From this study, it is concluded that the crown temperature distribution does not have any effect on the burner plane temperatures.

Table 5-6.
Comparison of average temperatures in the burner plane and on the whole domain for different crown temperatures.

	Average Temperature (K)	
Sensitivity Test	_Burner plane_	_Whole domain_
Constant temperature	1830	1849
Distribution of temperature	1830	1850

Conclusions from the Combustion Modeling

Different glass furnace models are thoroughly studied to find the effect of boundary conditions and port-to-port interactions. These models produce similar results for all variables in the region from 1.0 m above the glass surface to the crown. However, in the flame region, where the scalar gradients are high, the simulation results are sensitive to mesh resolution and for variables like inlet air flow rates. Except for velocities (and, in some cases, species), the simulations are unable to match the experimental measurements.

In order to get reliable predictions of temperature and major species:

1. The amount of air and fuel flow rates at the inlet should be measured accurately.

2. An accurate mean glass surface temperature, crown temperature (and emissivity) should be obtained.

3. Mixing should be resolved more accurately in the near burner region, which acts as a boundary condition for the full furnace model to capture the port-to-port interactions (if necessary).

4. Large eddy simulations to resolve more physics in the flame region.

Finally for NO_x model validation, we will need measurements of NO_x concentrations. We prefer data from within the combustion space and preferably within

the flame. However, we recognize the difficulty in obtaining such data. Whatever NO_x data we obtain must have the corresponding measurements for inlet and boundary conditions previously described.

6. THE REVERSAL CYCLE:
Fusion of Temperature Measurements for Furnace Control

Lee A. Bertram
Sandia National Laboratories
Livermore, CA

The crossfired furnace reverses its firing and exhaust sides after each t_{fire} interval and a pause Δt_{rev} has elapsed. Thus, a full heat/cool cycle of the regenerator has a period $2(t_{fire} + \Delta t_{rev})$. Perhaps the best index of this cycle is the integer flag 'HS-2SIDEFIRE.PV' stored by the PI database; it has value = 1 when the left side is firing, and value = 2 when the right fires. For a cycle which starts with firing on the right and then switches to the left, the temperature cycles of the rider arches of the regenerators are shown in Figures 6-1a and b.

These data histories indicate that the cycles repeat with great regularity, so each should have a curve fit to it which captures its shape. To illustrate the point, Figure 6-2 shows the data for the rider arch below Port 7 in the February run, plotted from the inferred beginning of the heatup cycles at 21:50:26.4. The triangles in the plot indicate a remarkable repeatability of the tracing of this cycle, with the scatter among corresponding data points being less than half the expected standard deviation of about 7.5 °F for thermocouples at temperatures 1100-1800 °F.

The curves of Figures 6-1 and 6-2 can be fit roughly with a four-part function consisting of a pause of length Δt_{rev} followed by a heat-up curve, then another Δt_{rev} pause as the firing reverses, then finally a cool-down curve as combustion air flows by. The heat-up and cool-down curves are the following piecewise exponentials:

$$T_h(t) = T_{min} + \Delta T_h \{1 - \exp[-(t - \Delta t_{rev})/\Delta t_h] \} \qquad (6\text{-}1)$$

with the time t being that elapsed since the start of the cycle, so the heating interval is $\Delta t_{rev} < t < (\Delta t_{rev} + t_{fire})$, and thus $0 < (t - \Delta t_{rev}) < t_{fire}$ in terms of the firing time t_{fire}. If the temperature is T_{max} at time $\Delta t_{rev} + t_{fire}$, then $\Delta T_h = (T_{max} - T_{min})/[1 - \exp(-t_{fire}/\Delta t_h)]$. After the pause of duration, Δt_{rev}, with $T = T_{max}$, cooling begins at $t_c = 2\Delta t_{rev} + t_{fire}$, which is fit by:

$$T_c(t) = T_{ref} + (T_{max} - T_{ref}) \exp[-(t-t_c)/\Delta t_c] \qquad (6\text{-}2)$$

where $T_{ref} = [T_{min} - T_{max} \exp(-t_{fire}/\Delta t_c)] / [1 - \exp(-t_{fire}/\Delta t_c)]$. The main point here is that the cycle is characterized by six parameters, T_{min}, T_{max}, t_{fire}, Δt_h, Δt_c, and Δt_{rev}, and the exponential function giving the shape of the curves. The fact that it can be captured with

a.
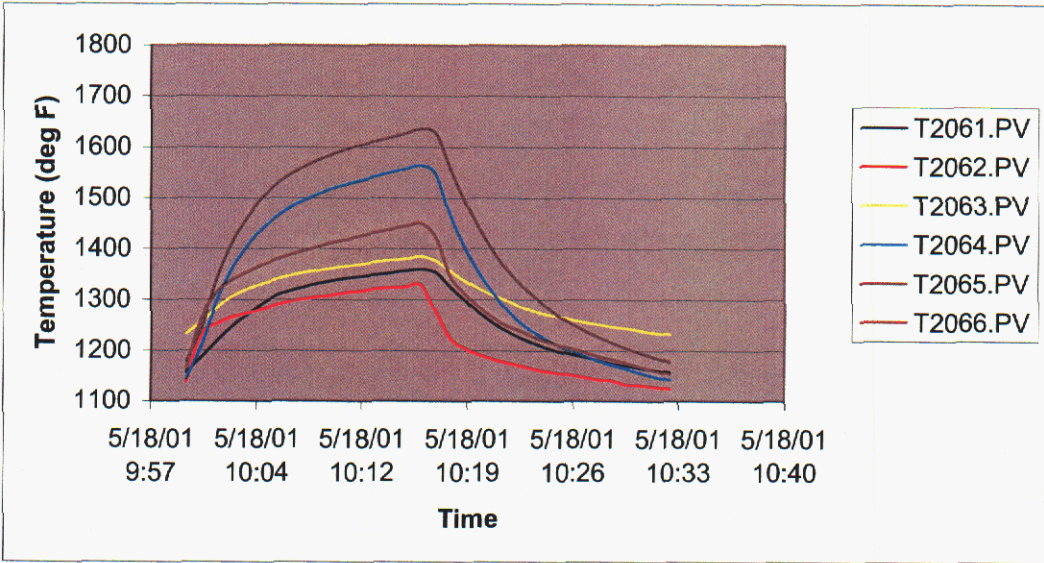
b.
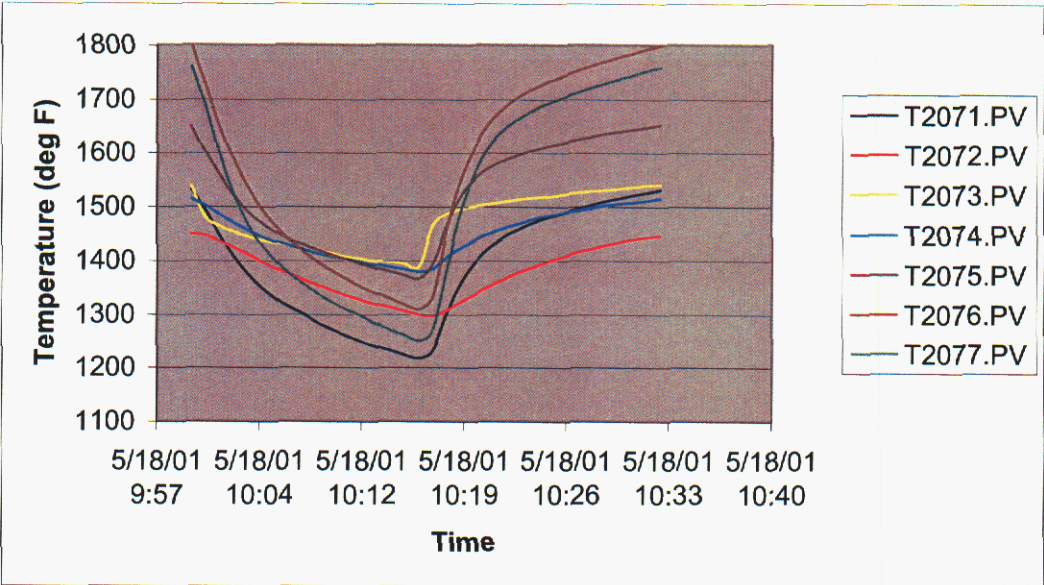
Figure 6-1. Rider arch thermal cycles on line 14-2 during May 2001 production run. Data at one-minute intervals from PI database.
   a.   Heat-cool cycle of left regenerator below ports 1 through 6.
   b.   Cool-heat cycle of right regenerator rider arches below ports 1 through 7.
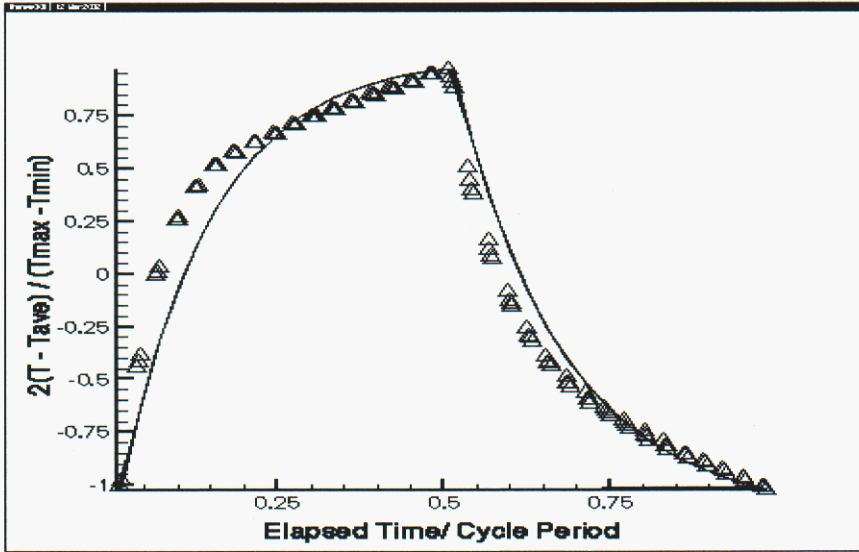
Figure 6-2. Repeatability of thermocouple data from rider arches. Port 7 in the right regenerator traces out the same curve with variations of only $\pm$ 3 °F over 4 cycles of period 34.08 min (triangles). The curve fit by Equations (6-1) and (6-2) is shown as the continuous curve, using $\Delta t_{rev.}$ = 0.5 min, t_{fire} = 16.54 min, Δt_h = 4.667 min, and Δt_c = 5.5 min for all of the rider arches.

so few parameters is important. Each temperature cycle defined by Equations (6-1 and 6-2 has an average value:

$$T_{ave} = \frac{1}{2}(T_{max} + T_{min}) - (T_{max} - T_{min}) \, f(t_{fire}, \Delta t_h, \Delta t_c, \Delta t_{rev}) \qquad (6-3)$$

where the period is $t_{per} = 2(\Delta t_{rev} + t_{fire})$ and

$f(t_{fire}, \Delta t_h, \Delta t_c, \Delta t_{rev}) =$

$\{\Delta t_h - \Delta t_c - t_{fire}[\exp(-t_{fire}/\Delta t_h) - \exp(-t_{fire}/\Delta t_c)]/[1 - \exp\{-t_{fire}/\Delta t_h\}][1 - \exp\{-t_{fire}/\Delta t_c\}]\}/t_{per}$

is the weighting appropriate to the exponential fit. Physically, the meaning of Equation (6-3) is that there is an average temperature which differs from the arithmetic mean of the peak and valley temperatures, $\frac{1}{2}(T_{max} + T_{min})$, by an amount that depends on the shape of the curves. This average value should be repeated cycle after cycle when the process is under control.

Equations (6-1 to 6-3) are presented to illustrate that well-chosen representations can capture the information contained in the PI database using several orders of magnitude less storage. Perhaps the point is best made by comparison of the plot of rider arch temperatures as stored by the PI database (Figure 6-3), requiring about 10^5 words, with Table 6-1, which contains all 40 or so of the words required by Equations (6-1 to 6-3).

The choice of exponential fits was physically motivated, of course. The expectation that the gas stream and the checkers asymptotically converge on the same temperature, over some time scale determined by the thermal diffusivity and the size of the checkers (Günther, 1958; Trier, 1987) suggests the form of Equations (6-1 and 6-2), and the ability of the very simple fit to capture most of the variation of the signals verifies that this is a reasonable expectation. In fact, the fit is sufficient to make several basic statements about handling this data. The very same statements will be true for any more faithful fit, such as that provided by wavelets (Chui, 1977).

The first issue, data compression, is raised already. As each 17.04-minute segment of data is captured, it can be reduced to values for T_{min} and T_{max}, and a 'yes' or 'no' decision made on whether its fit to the scaled function for the cycle shape (curve in Figure 6-2) is satisfactory. When the result is 'yes', the second-by-second data need not be stored, only the values for T_{min} and T_{max}.

An immediate advantage to using the scaled data is that it allows use of a simple metric to identify outliers. Isolated bad data can be screened as it is acquired. That is, in Figure 6-2, as each new data point (triangle) is captured during the process, its vertical distance from the cycle shape function [Equations (6-1 to 6-3)] can be computed, and values more than, say, 0.10 away from the expected values identified as outliers. Such values could be discarded, stored for later inspection, or could be used to trigger a call for attention by engineers, operators, or sensor maintenance personnel. The key point is that
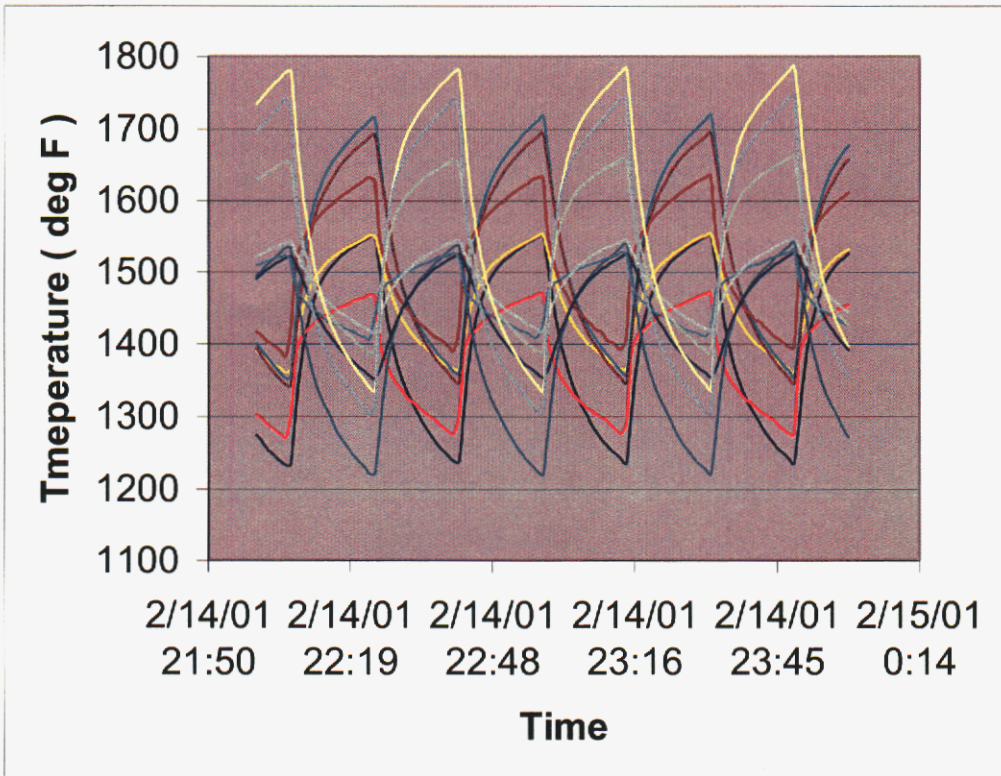
Figure 6-3. PI database storage for rider arch temperatures during February 2001 production run. At the rate of 1 sample/s, about 10^5 words of data are stored.

Table 6-1.
Total Dataset (26 words) Needed to Reproduce Figure 6-3.
Representation uses Equations (6-1 and 6-2) and the timescales in the caption of Figure
6-2 above (4 words). Total data compression achieved is about 2500:1.

Thermocouple	T_{min} (°F)	T_{max} (°F)
T2061	1232	1552
T2062	1270	1471
T2063	1360	1553
T2064	1352	1719
T2065	1341	1694
T2066	1382	1634
T2071	1220	1542
T2072	1351	1526
T2073	1406	1531
T2074	1416	1547
T2075	1385	1661
T2076	1334	1786
T2077	1301	1747
T2081	2577	2669

the same test is applied to all channels, rather than having a custom algorithm developed
for each.

An operational upset could also lead to data values moving away from the
established cycle shape function, and the correct response in that case is to initiate control
action. Thus, controls using the data need to be able to distinguish between isolated
flukes in sensor reports and good data reporting systematic movements of the furnace
away from the standard condition. One test that makes the interpretation as a real,
systematic movement would be the consistency of subsequent data, departing as far or
farther from the standard condition. This requires delaying any action until an ongoing
pattern is established. Another test to indicate good data is consistency with neighboring
and related sensors. For the rider arches, every thermocouple has at least one neighbor;
the interior ones each have two neighbors. If the neighboring thermocouples are
reporting data with the same trend as the out-of-bounds signal, the likeliest interpretation
would be that the data are good, and control action should be taken, or an advisory
message should call attention to the departure. This is an example of "sensor fusion," in
which two or more sensors are used to validate each others' data. Alternatively, this can
be described as replacement of a single-input control with a multiple input, based on the
group of sensors rather than on one alone.

The issue of identifying and utilizing related sensor data necessarily involves
establishing cause-and-effect relationships for events in the furnace. Clearly, such a
relationship is to be expected for the regenerator crown temperature: when the rider

arches run hotter or cooler than normal, the crown temperatures must follow. To determine the degree to which this is true, the first step would be to analyze the regenerator crown thermocouples in the same way as the rider arch thermocouples have been treated above. However, only one regenerator crown thermocouple was indicating reliably during the February 2001 and May 2001 runs, the one at Port 1 on the left side (Figure 6-4). The figure clearly indicates that the regenerator crown temperature history can be represented very well in the same manner as the rider arch temperatures, but, without additional data, firm cause and effect relationships cannot be established.

In seeking relationships to other data from the furnace, one might ask: "Is rider arch temperature data useful for control, or only as a furnace status check? Did it respond, for example, to the large excess of combustion air introduced in February 2001?" In this specific event, it was clearly responsive. In particular, there is a morning and an afternoon dataset in the "Reversal" files for February 2001 and also for May 2001. During the morning of the February 2001 dataset, the air/gas ratio firing on the right side had been held at about 19 for several days, but was reduced to about 14 by evening. For both the morning and evening of the May 2001 dataset, the right side air/gas ratio was 13.5. If the average of the rider arch T_{ave} values is taken, it can be used as a measure of the general level of temperature, call it T_{gen}, in the flue. This value T_{gen} was 140 °F hotter in February 2001 than in May 2001. This suggests some longer-term changes in operation, perhaps beyond those due to the air/gas ratio changes.

Tracking T_{ave} over a production run, one can tell at a glance whether the process is stable or not, and deviations of 25 °F or greater will be apparent in such a plot even though such small changes would not be apparent in the raw plot of several hundred cycles drawn as a continuous curve. Certainly the use of any discrete sample time (such as hourly sampling, for example) would be confusing at best and meaningless to the user most of the time (Figure 6-2).

In summary, the behavior of the rider arch temperatures can be monitored with little effort (and great stability) by imposing a template such as the exponential fit (or a better approximation in the form of a wavelet), extracting and tracking average values over whole cycles, and monitoring incoming data for departure from the predictive template. This kind of sensor fusion can stabilize control loops that have used single-input signals and are thus vulnerable to outliers in the data. The template can reject outliers with great confidence.

The basic problem here is the presence of many time scales in the data. For the rider arch example, there are clearly changes on the scale of minutes when tracking the cycle shape, changes on the scale of hours as the cycle average evolves, perhaps also diurnal cycles, and long-term drift over the duration of a production run.

For effective utilization of such data by operators and engineers, separate displays would be provided on these time scales. A record such as that shown in Figure 6-1 could be collapsed onto the template (except for Ports 3 and 4) and checked for departure from the template as the cycle evolves.
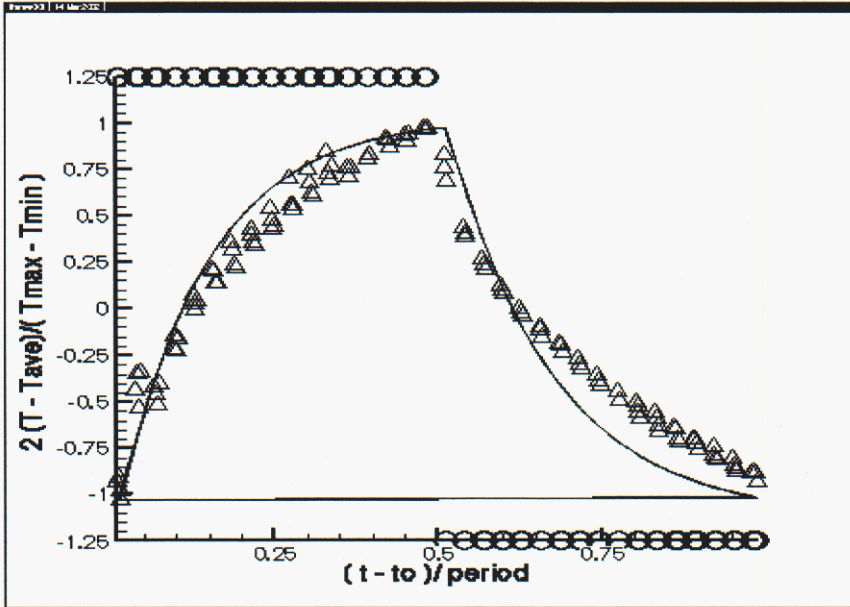
Figure 6-4. Regenerator crown temperature cycle. The thermocouple is near Port 1 in the left regenerator; triangles give data for February 14, 2001. High circles indicate firing on the right (HS-2SIDEFIRE = 1); low circles denote firing on the left (HS-2SIDEFIRE = 1). The curve is described by Equations (6-1 and 6-2), with parameters from Table 6-1 for thermocouple no. T2081.

There remains the curious problem that the Port 3 and 4 thermal cycles appear as though truncated. Were the airflow through the checkers uniform and heat transfer conditions at the gas/packing interface the same, these cycles would resemble the others. The fact that they do not suggests either flow anomalies or the presence of contamination on the refractory. Could Na_2SO_4 be freezing and melting in large quantities in these zones, and not in the others? Could the thermocouples be in a place where there are local heat sources and sinks? Could the thermocouples be mounted in a different way from the others? The Port 4 thermocouple seems more deeply embedded in refractory, because its response is smoother and has peaks and valleys that lag the others by a couple of minutes. Did these signals also have this truncated form at the beginning of this tank's present campaign?

7. MODELING AND CONTROL OF A FLOAT GLASS ANNEALING LEHR*

William G. Houf
Sandia National Laboratories
Livermore, CA

Introduction

Work on modeling and control of float glass annealing lehrs continued, in order that maximum benefit will be realized from the results obtained by Bertram (2001a and 2001b) and Houf (2002) in the first phase of the project. This section presents the details of a fully coupled 3-dimensional model of heat transfer in a float glass annealing lehr that is designed to execute rapidly on a small computer workstation so that it may be used by process engineers to determine optimum set points for lehr operation. The model executes rapidly enough that it may also be suitable for use in real-time model-based control.

A float glass annealing lehr is a large enclosure through which a thin ribbon of float glass continuously moves at a fixed speed. The proper annealing of float glass requires control of the temperature history of the glass ribbon as it moves through the lehr. If the ribbon is cooled too slowly or too rapidly, undesirable residual stresses can occur in the glass that make final cutting of the glass difficult. If large temperature variations develop across the width of the glass ribbon, then large membrane stresses can occur that warp or even split the glass ribbon before it can be cut.

Controlled cooling of the float glass in a continuous feed production facility is performed in the annealing lehr. The annealing lehr may be as long as 120 meters and is approximately 5 meters in width. Longitudinally the lehr is broken into several zones, each of which acts as a separate heat exchanger. Laterally each zone is divided into several flues or ducts through which air flows at a controlled rate and initial temperature. The exterior walls of the ducts form the top and bottom surfaces of the lehr enclosure and as the hot glass ribbon is drawn through the lehr on rollers it exchanges heat with the air flow in the ducts. By varying the flowrate and inflow temperatures of the air in the ducts, both the longitudinal and lateral temperature distribution of the glass ribbon can be controlled as it cools. Figure 9-1 shows a sketch of a portion of the annealing section of a typical float glass lehr.

In typical operation, set points for duct air flowrates and temperature are determined from past experience. Any change in conditions of the glass ribbon, environment, or production schedule may require trial-and-error tuning to maintain stable operation of the lehr. This can be a costly and time-consuming process and often results in set points that may not produce optimum yield.
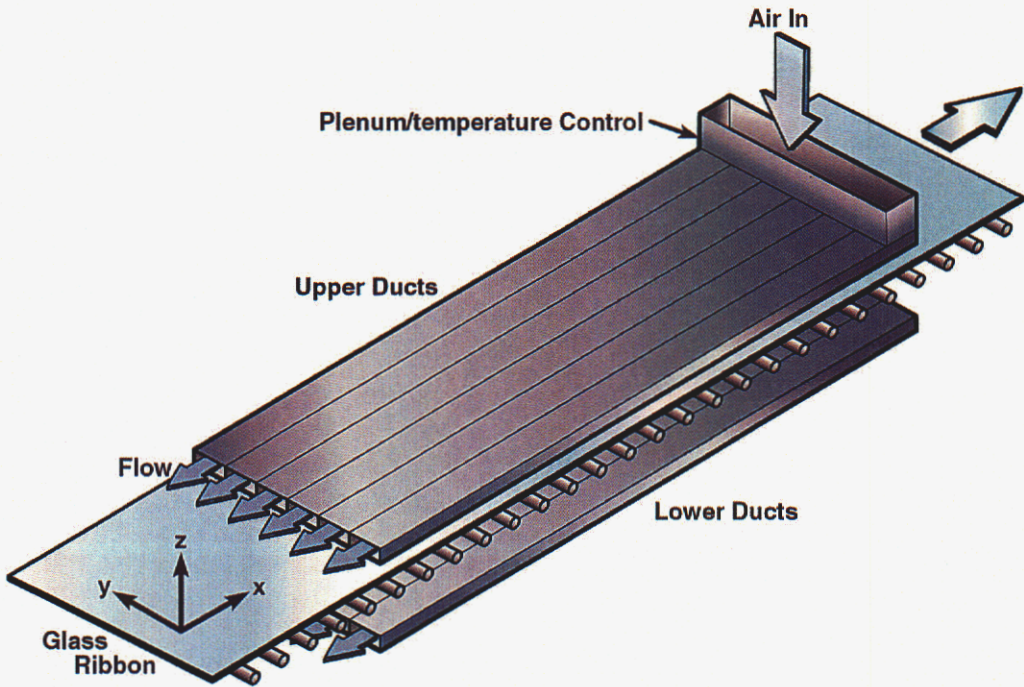
Figure 7-1. Sketch of a portion of the annealing section of a typical float glass lehr.

This paper presents a fully coupled 3-dimensional model of heat transfer in an annealing lehr that is designed to execute rapidly on a small workstation. The model treats heat conduction and advection in the moving glass ribbon and considers the semitransparent nature of radiative heat transfer in the glass. The model also accounts for mass flow of air and heat transfer in the cooling ducts and surface-to-surface radiative exchange between the exterior walls of the ducts and glass ribbon. The model computes a total energy balance on the lehr as part of each simulation.

Results show the effects of operating conditions on the glass temperature distribution in a typical lehr and illustrate the use of mathematical modeling to improve design, operation, and control. The model has also been used to perform inverse problems, where necessary changes in lehr operating conditions required to compensate for changes in lehr inlet glass temperature have been computed. Finally, a simple lehr temperature control algorithm is proposed and demonstrated by application to successful control of the lehr simulation model.

Mathematical Model

Previous modeling studies on annealing lehrs include the work of Chui (1977) who considered gray-body radiation between the moving glass ribbon and its enclosure and convection of gas in the flue system for a lehr with identical arrays of top and bottom ducts. Gardon (1982) used a one-dimensional model of heat transfer in an annealing lehr to compute annealing stresses and lehr thermal performance. Bertram (2001b) developed a closed-form solution for the heat transfer between the glass ribbon and a single duct when the ribbon and duct are considered infinitely wide.

This paper presents the details of a fully coupled 3-dimensional model of heat transfer in a float glass annealing lehr that is designed to execute rapidly on a small computer workstation so that it may be used by process engineers to determine optimum set points for lehr operation. The model treats heat conduction and advection in the moving glass ribbon and includes the non-gray semitransparent properties of radiative transfer in the glass. The model also accounts for mass flow of air and heat transfer in the cooling ducts and surface-to-surface radiative exchange between the exterior walls of the ducts, lehr side walls, and the glass ribbon. Heat transfer to the rollers supporting the moving glass sheet is presently not considered in the analysis.

The lehr heat transfer model is based on the schematic representation of the cross-section of a typical float glass annealing lehr shown in Figure 7-2. A radiation enclosure is formed by the inside walls of the cooling flues, the lehr sidewalls, and the glass ribbon. Heat is exchanged by radiation among the surfaces of this enclosure and the net gain or loss of energy by the glass ribbon results in its temperature change as it moves through the lehr. Heat is also transferred by convection from the flue walls to the flowing air stream and the temperature of the air is changed accordingly. Heat loss through the lehr side walls to the ambient is also included.
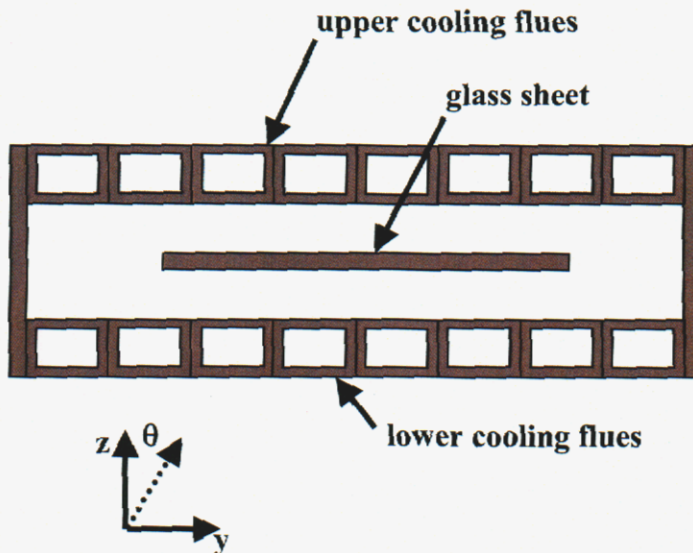
Figure 7-2. Schematic of cross-section of a typical float glass annealing lehr.

The conservation of energy equation for the glass ribbon is of the form (definitions of symbols may be found in the list of nomenclature at the end of this section)

Glass ribbon:

$$\rho c_p u \frac{\partial T}{\partial x} = \frac{\partial}{\partial y}\left(k\frac{\partial T}{\partial y}\right) + \frac{\partial}{\partial z}\left(k\frac{\partial T}{\partial z}\right) - \frac{\partial q_{rad}}{\partial z} \tag{7-1}$$

where T is the local glass temperature, k and c_p are the thermal conductivity and specific heat of the glass respectively, u is the speed of the glass ribbon, and q_{rad} is the local radiative heat flux inside the glass sheet.

Conduction of heat in the direction of the glass ribbon pull (x) was neglected compared to advection. For the air in each of the flues the conservation of energy equation is

Flue air:

$$\pm m_i c_{p,air}\frac{dT_{air,i}}{dx} + h(T_{wall,i} - T_{air,i})w_i = 0 \tag{7-2}$$

where m_i is the air mass flow rate through flue i, $c_{p,air}$ is the specific heat of air, $T_{air,i}$ is the local air temperature in flue i, $T_{wall,i}$ is the local flue wall temperature, w_i is the width of the flue, and h is the heat transfer coefficient between the flue wall and the flue air. The negative sign on the first term of Eq. (7-2) is used when the flue air and glass ribbon are in concurrent parallel flow, while the positive sign is used when they are in counterflow. The model can consider an arbitrary number of flues; in the present analysis 8 flues (see Figure 7-2) were considered, and Eq. (7-2) represents 8 equations for the individual flue air temperatures. Equation (7-2) assumes that the temperature of the air in each flue varies only in the direction of flow and that heat transfer between adjacent flues and to the environment is negligible.

To evaluate the gradient of the radiative heat flux in Eq. (7-1) the glass ribbon was assumed to be a plane-parallel absorbing-emitting medium and the radiation field within the glass was determined by solving the one-dimensional radiative transfer equation

$$\cos\theta \frac{\partial I_\lambda}{\partial z} = -\kappa_\lambda I_\lambda + \kappa_\lambda I_{b,\lambda} \tag{7-3}$$

where $I_\lambda(\theta, z)$ is the spectral intensity, κ_λ is the spectral absorption coefficient of the glass, and $I_{b,\lambda}(T)$ is Planck's function. Eq. (7-3) is solved for $I_\lambda(\theta, z)$ subject to boundary conditions on the top and bottom faces of the glass ribbon that account for transmission and reflection at the glass surface. The irradiation on the faces of the glass ribbon is computed as part of the enclosure analysis given by Eqs. (7-5) through (7-7). Once the intensity in the glass is computed, the positive and negative components of the radiative flux as well as the total radiative flux are then obtained from Eq. (7-4)

$$q_{rad}(z) = q_{rad}^+(z) + q_{rad}^-(z) =$$
$$2\pi \int_\lambda \int_0^1 I_\lambda(z,\mu)d\mu d\lambda + 2\pi \int_\lambda \int_{-1}^0 I_\lambda(z,\mu)d\mu d\lambda \tag{7-4}$$

where $\mu = cos\ \theta$ and the integration over λ is for wavelength. Data for the spectral absorption coefficient of glass (Viskanta and Anderson, 1975) indicates that glass is opaque to radiation greater than approximately 4.5 μm. Hence a 2-band model was used where the glass was considered to be semitransparent with a constant absorption coefficient at wavelengths less than 4.5 μm and opaque to radiation greater than 4.5 μm. Equation (7-3) is solved in closed form (Viskanta and Anderson, 1975; Brewster, 1992) for use in the lehr heat transfer model.

Heat transfer in the lehr enclosure is dominated by radiation and the net radiative exchange method (Siegel and Howell, 1992) was used to compute the energy transfer. The equations are of the form

$$J_i = \varepsilon_{wall,i}\sigma T_{wall,i}^4 + (1 - \varepsilon_{wall,i})G_i \tag{7-5}$$

$$G_i = \sum_{j=1}^N J_j F_{j-i} \tag{7-6}$$

$$G_i - J_i - q_i = 0 \tag{7-7}$$

where J_i is the radiosity leaving an element i, G_i is the irradiation on a wall or glass surface element i, $\varepsilon_{wall,i}$ is the emissivity of wall element i, σ is the Stefan-Boltzmann constant, $T_{wall,i}$ is the temperature of wall element i, q_i is the convective or conductive heat flux from wall element i, and F_{j-i} are the shape factors between elements on the walls and elements on the top and bottom surfaces of the glass ribbon. For flue wall elements the expression $q_i = h(T_{wall,i}-T_{air,i})$ is used in Eq. (7-7) to account for convective heat transfer to the flue air. For lehr side wall elements the expression $q_i = U(T_{wall,i}-T_{amb})$ is used in Eq. (7-7) to account for heat loss through the side walls to the environment, where U is an overall heat transfer coefficient and T_{amb} is the ambient temperature. Radiosities, J_i, leaving lehr wall elements are computed from Eq. (7-5), while radiosities leaving elements on the top and bottom surfaces of the glass ribbon are computed as part of the solution to Eq. (7-3). Temperature gradients in the longitudinal direction are small and were neglected in computing the radiative exchange in the enclosure.

The three-dimensional temperature distribution in the glass sheet is found by marching Equations (7-1) through (7-7) in the longitudinal direction (x). The y and z derivatives in Eq. (7-1) are discretized with central differences over a two dimensional mesh placed over the cross-section of the glass ribbon and the closed-form solution to Eq. (7-3) is used to evaluate the gradient of the radiative heat flux. These differential equations for glass temperature and the differential equations for flue air temperatures (Eq. (7-2)) are solved in conjunction with the nonlinear algebraic equations (Eqs. (7-5) to (7-7)) for the temperatures of the lehr flue walls and side walls using the Sandia developed code DASSL (Petzold, 1982). For cases where the flue air and glass ribbon

are in counterflow a shooting method is also used to iterate for the specified flue air inlet temperatures. A grid refinement study was performed to ensure that the solution was independent of grid size.

Baseline Results

A set of baseline dimensions and operating conditions for a typical counterflow float glass annealing lehr are shown in Table 7-1 (Chui, 1977). The baseline mass flowrate of air through each of the flues was computed by setting the product of total air mass flowrate and air specific heat equal to the product of the glass mass flowrate and glass specific heat. The individual flue air flowrates were set by dividing the total air flowrate by the number of flues. The heat transfer coefficient in the flues was determined from the empirical expression (Perkins and Worsoe-Schmidt, 1965)

$$Nu_w = 0.023\,\mathrm{Re}_w^{0.8}\,\mathrm{Pr}_w^{0.4}\left[1+\left(\frac{x}{D}\right)^{-0.7}\left(\frac{T_w}{T_b}\right)^{0.7}\right] \tag{7-8}$$

where Nu_w is the Nusselt number, Re_w is the Reynolds number, D is the hydraulic diameter of the flue, T_w is the flue wall temperature, and T_b is the bulk temperature of the air. For values of (x/D) greater than 24 the (x/D) term is dropped.

Viskanta and Anderson (1975) report a glass absorption coefficient of approximately 1.0 cm^{-1} in the semitransparent band and this was taken as the baseline value. If a Planck-averaged value is computed at 1000 K, then the value becomes approximately 3.0 cm^{-1}. A baseline value of 0.2 was used for the glass surface reflectivity based on Viskanta and Anderson (1975).

Figure 7-3 shows temperature contours across and down the glass ribbon for baseline operating conditions. The glass cools faster near the edge of the ribbon due to heat loss through the walls of the lehr and because there is more flue air per unit mass of glass under the edge flues.

Figure 7-4 shows a comparison of glass and flue air temperatures from the present analysis with the analysis of Chui (1977). Chui considered an opaque glass ribbon with an emissivity of 0.8. The two-band semitransparent model of the present analysis was made to simulate Chui's opaque glass ribbon by assuming a very large value of the absorption coefficient (1000 cm^{-1}) in the semitransparent band and a value of 0.2 for the glass surface reflectivity. The best agreement with the results of Chui were obtained when a constant value of $h = 17$ W/m^2 was used for the convective heat transfer coefficient between the flue walls and flue air.
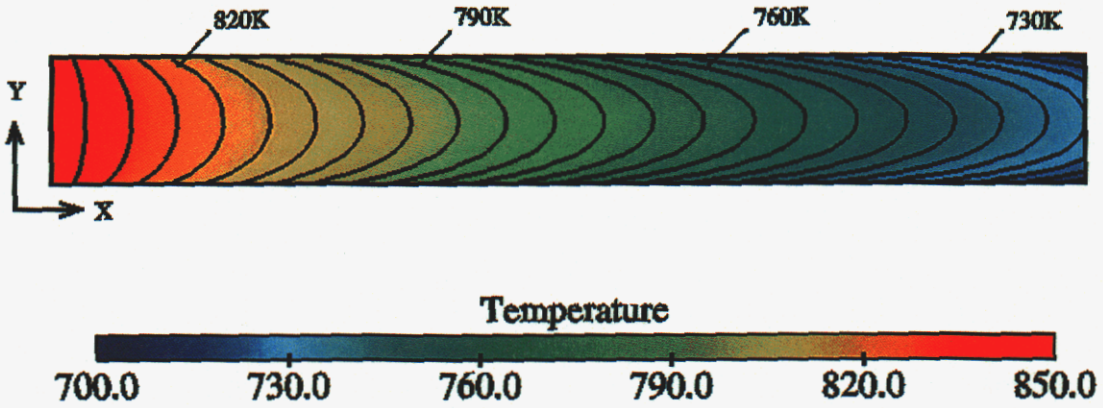
Figure 7-3. Temperature contours in the center plane of the glass ribbon for baseline conditions (5 K intervals).

Table 7-1.
Baseline operating conditions for counterflow float glass annealing lehr.

Glass Ribbon	
Width	330.2 cm
Thickness	0.254 cm
Speed	1270 cm/min
Glass Inlet Temperature	838.7 K
Lehr	
Width	406.4 cm
Height	51.054 cm
Length	2743.2 cm
Side wall Conductance (U)	1.42×10^{-4} W/cm^{2}K
Wall emissivity	0.90
Flues	
Width	50.8 cm
Height	15.24 cm
Length	2743.2 cm
Air Inlet Temperature	616.4 K
Wall emissivity	0.90

The value of the reflectivity of glass can vary depending on the material comprising the glass and the wavelength and angle of incidence of the incoming radiation. The sensitivity of the model calculations to variations in the reflectivity of the glass was assessed by using the standard model parameters and varying the value of the glass reflectivity between 0 and 0.2. Figure 7-5 shows the lateral temperature variation across the exit of the glass ribbon for different values of glass reflectivity. Temperature at the center of the glass ribbon varies from approximately 730 K for a reflectivity of 0.2 to a value of 748 K for a reflectivity of 0.05.

- 83 -
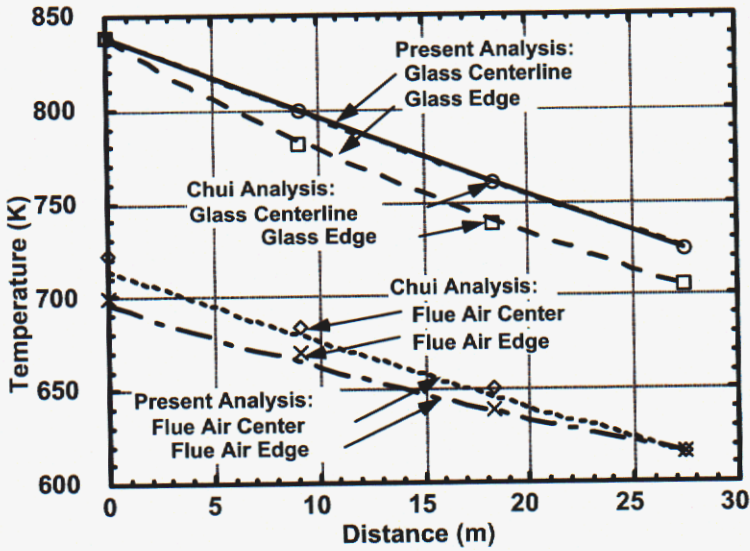
Figure 7-4. Comparison of longitudinal (*x*-direction) temperature distributions from present analysis (lines) with the analysis of Chui (points) for an opaque glass sheet assuming a flue to air heat transfer coefficient of 17 W/m^2.
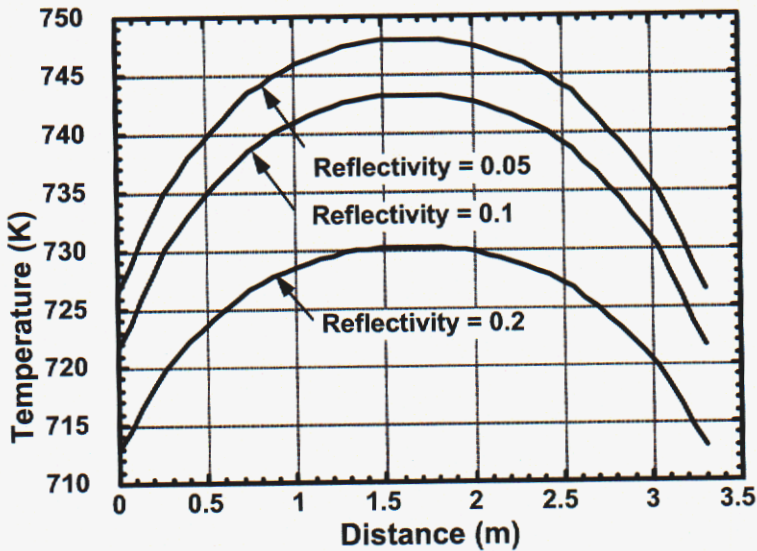
Figure 7-5. Computed lateral (*y*-direction) temperature distribution in the glass sheet at midplane at the lehr outlet for different values of glass surface reflectivity (baseline conditions).

Inverse Problem

The results above illustrate the application of the model to compute glass ribbon response given a set of inlet conditions for the glass ribbon and flue air. The model can also be used to solve inverse problems where the inlet flue air conditions required to achieve a desired exit glass temperature profile are computed. This procedure is similar to a control scheme where the inlet and outlet glass temperatures are monitored and the model supervises the flue air inlet conditions to correct the glass outlet temperature to a pre-set target. The numerics of this inverse method are accomplished by treating the lehr model as a system of nonlinear functions where the flue inlet conditions are the inputs and the difference between the glass outlet temperature and the desired pre-set outlet temperature profile are the responses to the inputs. A Powell Hybrid method (Powell, 1988) was used to find the inputs of this system that minimize the sum of the squares of the output response functions.

As an example of the inverse method consider the baseline counterflow annealing lehr of Table 7-1 with a uniform inlet glass temperature of 838.7 K. For the flue air flowrates specified in previous section it is desired to compute the inlet air temperatures of the 4 upper and 4 lower flues required to cool the glass ribbon to a uniform outlet temperature of 728 K. The inverse method computes that the inlet air temperature in the 8 flues from edge to center to be 758.4, 696.3, 690.3, and 686.9 K, respectively, where the temperatures in the adjacent top and bottom flues are assumed equal. Figure 7-6 shows contours of the temperature in the glass ribbon at center plane for the inverse problem. The temperature profiles show that the glass temperature cannot be uniformly maintained throughout the cooling process. Although the exit temperature of the glass ribbon is controlled to be uniform, a temperature difference of approximately 0.25 K exists between the edge and center of the glass ribbon at the center plane.
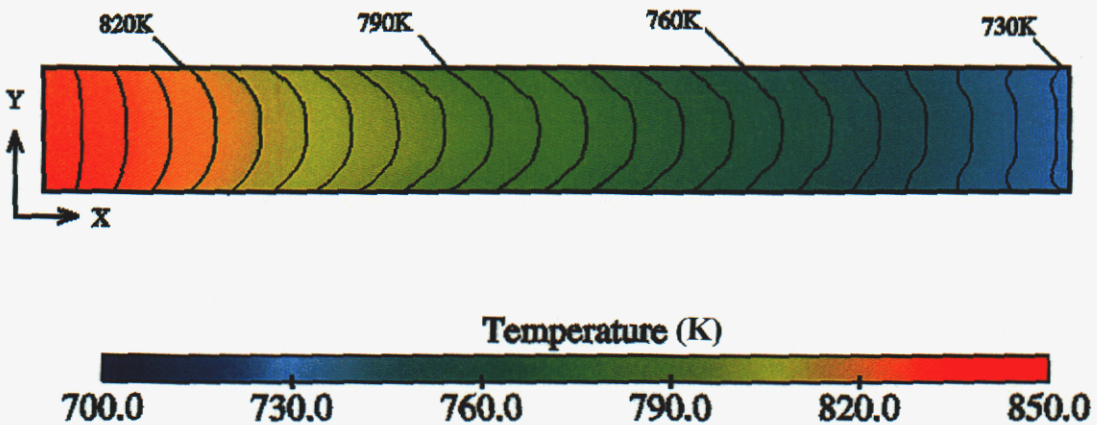
Figure 7-6. Temperature contours in the center plane of the glass ribbon for inverse problem (5 K intervals).

Control Algorithm

The lehr heat transfer model coupled with the inverse method of the previous section could be used as a control algorithm for the lehr. In this case the model must execute quickly enough on a small computer so that it could be applied on-line.

As an alternative the lehr model and inverse method could be applied off-line to create a schedule of operating conditions. In this approach, the flue conditions required to obtain a desired target glass exit temperature profile are first computed with the lehr model and inverse method. A perturbation is then introduced into one of the inputs of the model, such at the glass inlet temperature, and the inverse method is again applied to compute the change in flue conditions required to bring the glass exit temperature back to the target value. These two calculations are used to compute a relationship between the perturbation to the input and the change in flue conditions required to correct it. These relationships are called control coefficients and they may be used in a linear projection algorithm for on-line control of the lehr. A control algorithm of this type can initiate fast corrections to unexpected disturbances to a particular input. Although the control coefficients are valid for a wide range of disturbances, the lehr model and inverse method could be activated off-line periodically to improve and update the coefficients.

As an example, consider the results shown in Figure 7-6 as the standard operating point for the lehr. For this case the inverse method was used to compute the flue air temperatures required to cool the glass from a uniform inlet temperature of 838.7 K to a uniform outlet temperature of 728 K. For a perturbation in the glass inlet temperature, the control coefficients are to be calculated for a linear projection algorithm that will bring the glass exit temperature back to the desired target value of 728 K. To compute the control coefficients the original uniform glass inlet temperature of 838.7 K is perturbed by 10 K to a value of 848.7 K. The lehr model and inverse method are then executed again to compute a new set of flue air temperatures required to bring the glass exit temperature back to the target value of 728 K. Glass and flue air temperatures from this calculation as well as the original calculation in Fig. 6 are used to compute control coefficients according to the relationship

$$C_i = (T_{flue\ in,\ s} - T_{flue\ in,\ p})/(T_{glass\ in,\ s} - T_{glass\ in,\ p}) \tag{7-9}$$

where, C_i is the control coefficient for flue i, $T_{flue\ in}$ is the prescribed flue air inlet temperature for flue i, and $T_{glass,in}$ is the glass inlet temperature in the center of ribbon at the point directly beneath flue i. The subscripts s and p refer to standard and perturbed values of the temperatures respectively. Table 7-2 shows values of the control coefficients for standard lehr operating conditions shown in Figure 7-6, where the inlet glass temperature has been perturbed by 10 K. For this example case the control coefficients are assumed equal for adjacent upper and lower flues and symmetric about the centerline of the lehr.

Table 7-2.
Control coefficients for example lehr problem.

Flue Location	Control Coefficient, C_i
Edge	-0.7680
Next to Edge	-0.1616
Next to Central	-0.8579
Central	-0.9417

The control coefficients are used in a linear projection algorithm of the form

$$T_{flue\ in} = C(T_{glass\ in} - T_{glass\ in,\ s}) + T_{flue\ in,\ s} \qquad (7\text{-}10)$$

to perform on-line changes to flue air inlet temperature, $T_{flue\ in}$, as a response to changes in the inlet glass temperature profile $T_{glass\ in}$.

The linear projection control algorithm given by Eq. (7-10) was tested by applying it to control the lehr model. To test the algorithm the inlet glass temperature to the lehr was perturbed from the baseline uniform value to the parabolic profile shown in Figure 7-7. For this parabolic glass inlet temperature profile the flue air inlet temperatures required to bring the glass exit temperature back to the uniform target exit temperature of 728 K are projected using Eq. (7-10) with the control coefficients in Table 7-2. The flue air inlet temperatures computed from Eq. (7-10) are then used in the annealing lehr model (without the inverse algorithm) to compute the glass exit temperature. If the projection algorithm is valid, the computed glass exit temperatures should be very close to the uniform target value of 728 K. Figure 7-8 shows contour plots of the temperature in the glass ribbon for the linear projection algorithm test case. The exit temperature of the glass is very close to the uniform target value of 728 K and has a root-mean-squared error of approximately 0.05%. Hence, it appears that the linear projection scheme would provide a satisfactory means of on-line control.

Summary of Lehr Modeling and Control

A fundamental 3-dimensional model for heat transfer in a float glass annealing lehr has been presented. The model executes rapidly on a small computer workstation and has practical application for use by process engineers in determining optimum set points for annealing lehr operation. The model has been used to perform inverse problems, where necessary changes in lehr operating conditions to compensate for changes in load or other perturbations have been computed. This capability, coupled with the models fast execution on a small workstation indicates that it may also be suitable for use in real-time model-based control of float glass annealing lehrs. As an alternative, a quick linear projection control scheme has been developed and demonstrated by application to successful control of the lehr simulation model. The model computes a total energy balance on the lehr as a part of each simulation.

Because the goal of an annealing lehr is to control stress in the glass, future work should include the development and coupling of a stress model with the annealing lehr thermal model.
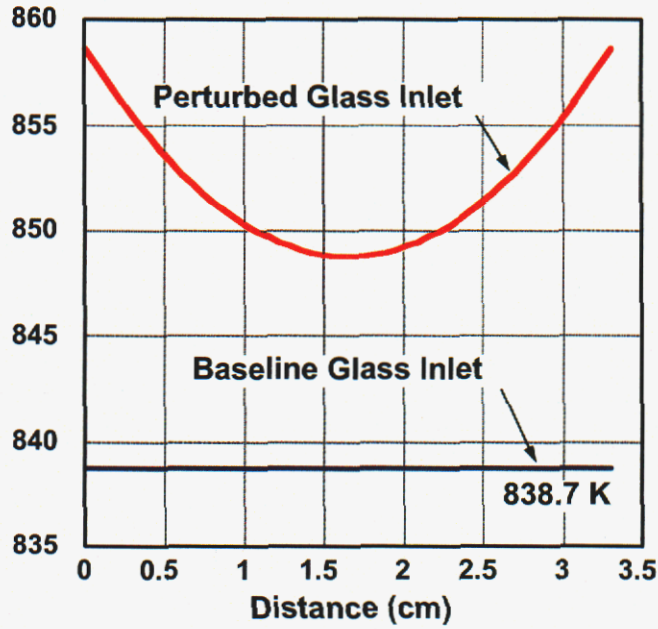
Figure 7-7. Baseline and parabolic glass inlet temperature profiles.
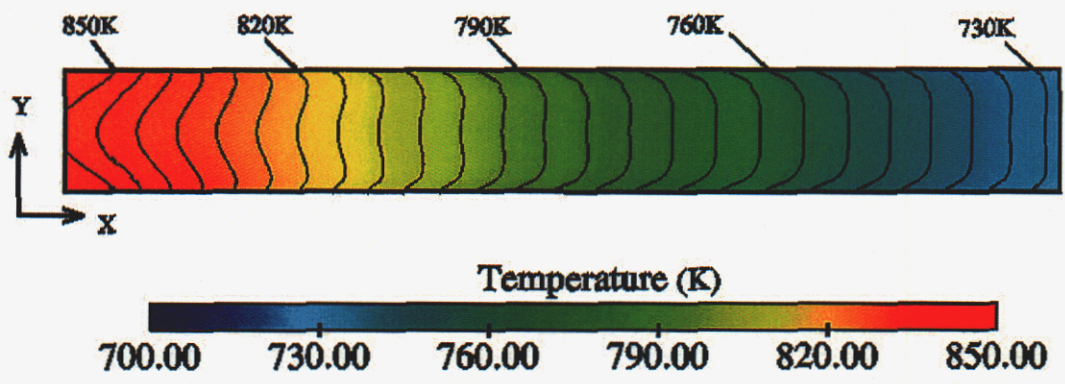
Figure 7-8. Temperature contours in the center plane of the glass ribbon for linear projection algorithm test case (5 K intervals).

Nomenclature for Section 7

c_p	specific heat
C_i	control coefficient for flue i
D	hydraulic diameter of the flue
$F_{j\text{-}i}$	shape factor from element j to element i
G_i	irradiation on element i
h	heat transfer coefficient from flue wall
$I_{b,\lambda}(T)$	Planck's function
$I_\lambda(\theta, z)$	spectral radiative intensity in the glass sheet
J_i	radiosity leaving element i
k	thermal conductivity
m_i	air mass flow rate through flue i
Nu_w	Nusselt number
Pr	Prandtl number
q_i	convective or conductive heat flux from element i
q_{rad}	radiative heat flux in glass sheet
Re_w	Reynolds number
T	temperature
U	overall heat transfer coefficient
u	speed of the glass ribbon
w_i	width of the flue i
x,y,z	Cartesian coordinates
$\varepsilon_{wall,i}$	emissivity of wall element i
κ_λ	spectral absorption coefficient of the glass
λ	wavelength
μ	$\cos\theta$
θ	azimuthal angle
ρ	density of glass ribbon
σ	Stefan-Boltzmann constant

Subscripts

air	values for air
b	bulk fluid properties
flue in	inlet flue air temperature
glass in	inlet glass temperature
i,j	element numbers
p	perturbed value
rad	radiative flux
s	standard value
w or wall	values at the wall
x	value along the x-coordinate direction
λ	wavelength
+,-	upward and downward flux values

Intentional Left Blank

REFERENCES

Aluminum Association, *Aluminum Industry Technology Roadmap*, Washington, DC, 1997. Available on the World Wide Web at <http://www.oit.doe.gov/aluminum/visions.shtml>.

American Chemical Society, American Institute of Chemical Engineers, Chemical Manufacturers' Association, Council for Chemical Research, and Synthetic Organic Chemical Manufacturers' Association, *Technology Vision 2020: The U.S. Chemical Industry*, Washington, DC, 1996.

American Forest and Paper Association, *Agenda 2020 - The Path Forward: An Implementation Plan*, Washington, DC, 1999. Available on the World Wide Web at <http://www.oit.doe.gov/forest/visions.shtml>.

American Iron and Steel Institute and Steel Manufacturers' Association, *Steel Industry Technology Roadmap*, 1998. Available on the World Wide Web at <http://www.steel.org/mt/roadmap/roadmap.htm>.

R. A. Bauer, H. P. H. Muijsenberg, R. Beerkens, and F. Simonis, "Advanced Control of Glass Tanks Using Simulation Models and Fuzzy Control," 29th International Symposium on Automotive Technology and Automation, Florence, Italy, 1996, Paper No. 96NM074.

R. A. Bauer and O. op den Camp, "Optimal Control of Glass Melting Process Using Simulation Models," 18th International Congress on Glass, San Francisco, July 5-10, 1998, Paper No. ICG063-B06-002.

L. A. Bertram, 2001a, "Elements for Real Time Steady Simulation of Flat Glass Lehr Control," SAND2001-8001, Sandia National Laboratories, Livermore, CA, January.

L. A. Bertram, 2001b, "Radiation Heat Transfer in a Glass Lehr," in: *CHT'01: Advances in Computational Heat Transfer II*, Proceedings of a Symposium organized by the International Centre for Heat and Mass Transfer, G. de Vahl Davis and E. Leonardi (Eds.), Begell House, Inc., New York, Vol. 2, pp. 1057-1064.

M. Q. Brewster, *Thermal Radiative Transfer and Properties*, John Wiley and Sons, Inc., New York, 1992.

M. G. Carvalho et al., Predictions of nitric oxide emissions from an industrial glass-melting furnace, *Journal of the Institute of Energy*, March 1990.

M. G. Carvalho, N. Speranskaia, and M. Nogueira, "A Physical-Model Based Expert System for the Optimisation of Glass Melting Furnaces Operation," 18th International Congress on Glass, San Francisco, July 5-10, 1998, Paper No. ICG651-B07-001.

Cast Metal Coalition, *Metalcasting Industry Technology Roadmap*, American Foundrymen's Society, North American Die Casting Association, and Steel Founders' Society of America, 1998. Available on the World Wide Web at <http://www.oit.doe.gov/metalcast/visions.shtml>.

G. K. Chui, "Heat Transfer and Temperature Control in an Annealing Lehr for Float Glass," *Journal of the American Ceramic Society*, Vol. 60 (1977) pp. 477–484.

P. R. Desam and P. J. Smith, "NOx Validation Study in an IFRF Glass Furnace: The influence of subgrid scale models on predictions," American Flame Research Committee International Symposium, Livermore, CA, October 15-17, 2003.

R. H. Duffus, "Control of Critical Variables on a Siemens Furnace," 29th International Symposium on Automotive Technology and Automation, Florence, Italy, 1996, Paper No. 96NM068.

J. Eisenhauer, P. Donnelly, S. McQueen, A. Monis, J. Pellegrino, and J. Julien, "Report of the Glass Technology Roadmap Workshop," held in Alexandria, VA, April 24-25, 1997, Prepared for the U.S. Department of Energy, Office of Industrial Technologies, by Energetics, Inc., Columbia, MD, September 1997. Available on the World Wide Web at <http://www.oit.doe.gov/glass/visions.shtml>.

D. Farmer, M. V. Heitor, J. Sentieiro, Vasconcelos, A. T., "New Methodology for Furnace Monitoring, Analysis, and Control," *Glass Industry*, October 1992, pp. 10-16.

Fluent, Inc., Fluent 5.5 User's Guides, Vols. 2 and 4.

R. Gardon, "Modelling Annealing Lehrs for Flat Glass," *Journal of the American Ceramic Society*, Vol. 65 (1982) pp. 372-379.

Glass: A Clear Vision for a Bright Future, Glass Industry Technology Vision and Research Agenda, January 1996.

R. Günther, *Glass-Melting Tank Furnaces*, Translated from the German by J. Currie, Society of Glass Technology, Sheffield, UK, 1958.

R. R. Hayes, Glass surface temperature and incident heat flux measurements in an industrial, regenerative, natural, gas-fired flat-glass furnace, M.S. Thesis, Brigham Young University, August 1999.

M. V. Heitor and D. P. Correia, "On the Monitoring of Industrial Glass Furnaces for Reduced Pollutant Emissions," 29th International Symposium on Automotive Technology and Automation, Florence, Italy, 1996, Paper No. 96GL013.

W. G. Houf, 2002, "Model for Heat Transfer in a Float Glass Annealing Lehr," to be presented at the 12th International Heat Transfer Conference, Grenoble, France, August 18-23, Paper No. 0639.

A. M. Huber, "Advanced Glass Process Control," 18th International Congress on Glass, San Francisco, July 5-10, 1998, Paper No. ICG718-B07-002.

T. Kimura, T. Ito, K. Inagaki, and T. Nakagawa, "The Bottom Temperature Control by Image Processing with the Wave-Let Method," 29th International Symposium on Automotive Technology and Automation, Florence, Italy, 1996, Paper No. 96NM073.

D. Koenig, "Generalized Predictive Control for Glass Manufacturing Processes," 18th International Congress on Glass, San Francisco, July 5-10, 1998, Paper No. ICG383-B07-003.

D. Koenig, "Generalized Predictive Control for Glass Manufacturing Processes," *Ceramic Engineering and Science Proceedings*, Vol. 20, Issue 1, 1999, pp. 181-206.

R. J. Mouly (Ed.), *Automatic Control in Glass*, International Federation of Automatic Control, Düsseldorf, 1973, distributed by the Instrument Society of America, Pittsburgh, PA.

T. Nakagawa, K. Tsuyosi, and T. Kimura, "Multiresolution Analysis and Control for Crown Temperature and Bottom Temperature of a Glass Melting Furnace,"

Proceedings: International Symposium on Glass Problems, Vol. 1, R. Akçakaya, N. Erinç, G. Albayrak, and S. Isevi, Eds., Istanbul, Turkey, September 4-6, 1996, pp. 550-556.

National Mining Association and U.S. DOE, Mining Industry of the Future, "Mineral Processing Technology Roadmap," September 2000. Available on the World Wide Web at <http://www.oit.doe.gov/mining/visions.shtml>.

National Science Foundation and National Institute of Standards and Technology, Workshop Report, "Process Measurement and Control: Industry Needs," Prepared by F. J. Doyle III, A. Garrison, B. Johnson, and W. D. Smith, New Orleans, March 6-8, 1998. Available on the World Wide Web at <http://www.oit.doe.gov/chemicals/visions_process.shtml>.

J. Newbold, B. W. Webb, M. Q. McQuay, and A. M. Huber, "Combustion Measurements in an Industrial Gas-Fired Flat-Glass Furnace," *Journal of the Institute of Energy*, June 1997, Vol. 70, pp. 71-81.

H. C. Perkins and P. Worsoe-Schmidt, "Turbulent Heat and Momentum Transfer for Gases in a Circular Tube at Wall to Bulk Temperature Ratios to Seven," *International Journal of Heat and Mass Transfer*, Vol. 8 (1965) pp. 1011-1031.

L. R. Petzold, Sandia National Laboratories Report, SAND 82-8637 (1982).

D. Pirovolou, G. Vachtsevanos, V. I. Henry, and A. M. Huber, "Intelligent Process Optimization and Control in Glass Manufacturing," Air and Waste Management Association, 89th Annual Meeting and Exhibition, Nashville, TN, 1996, Paper No. A1241.

M. J. D. Powell, "A Hybrid Method for Nonlinear Equations," in P. Rabinowitz (Ed.), *Numerical Methods for Nonlinear Algebraic Equations*, Gordon and Breach, 1988.

P. Sewell, *The Glass Researcher, Bulletin of Glass Science and Engineering*, New York State College of Ceramics at Alfred University, Vol. 6, No. 2, Winter 1997, p. 1.

R. Siegel and J. R. Howell, *Thermal Radiative Heat Transfer*, Hemisphere Publishing Corp., Washington, D.C., 1992.

M. H. Smith, D. K. Pirovolou, G. J. Vachtsevanos, A. M. Huber, and V. Henry, "A Neuro-Fuzzy Approach to Stabilization of Glass Fabrication Processes," 29th International Symposium on Automotive Technology and Automation, Florence, Italy, 1996, Paper No. 96NM070.

J. R. Staahl, J. M. Matesa, and D. E. Worth, "Manufacture of Flat Glass at Controlled Throughput Rate," U.S. Patent 4,004,900, January 25, 1977.

W. Trier, *Glass Furnaces: Design, Construction, and Operation*, Translated from the German by K. L. Lowenstein, Society of Glass Technology, Sheffield, UK, 1987.

U.S. DOE, "Technology Roadmap for the Petroleum Industry," Draft, February 2000. Available on the World Wide Web at <http://www.oit.doe.gov/petroleum/visions.shtml>.

R. Viskanta and E. E. Anderson, "Heat Transfer in Semitransparent Solids", *Advances in Heat Transfer*, Vol. 11 (1975) pp. 317-411.

Intentional Left Blank

APPENDICES

A. Radiation Heat Transfer in a Glass Lehr, *Lee A. Bertram*

B. Test Plan for the NO_X Control Experiments, *Robert G. Hillaire, Yu Jiao, David Hanekamp, and John J. Connors*

C. Full Furnace Simulation Results: Comparison of Oxygen Mole Fractions at the Glass Surface and Crown, *Padmabhushana R. Desam and Philip J. Smith*

Intentional Left Blank

Appendix A

RADIATION HEAT TRANSFER IN A GLASS LEHR

Lee A. Bertram
Sandia National Laboratories
Livermore, CA

Reproduced, with permission, from:

CHT'01: Advances in Computational Heat Transfer II, Proceedings of a Symposium organized by the International Centre for Heat and Mass Transfer, G. de Vahl Davis and E. Leonardi (Eds.), Begell House, Inc., New York, Vol. 2, pp. 1057-1064.

RADIATION HEAT TRANSFER IN A GLASS LEHR

Lee A. Bertram
Chemical and Materials Process Modelling,
Sandia National Laboratories
Livermore, CA 94551

ABSTRACT. In partnership with Ford/Visteon, Sandia National Laboratories investigated an intelligent control for the annealing lehr in float glass production, both for optimum usage of sensors and for the ability to report digitally the state of the lehr to an end-to-end control system, under DOE Office of Industrial Technology sponsorship. The heat transfer simulation of the lehr enclosure for that purpose is described here. This includes a closed-form solution for the infinitely wide glass ribbon, which allows robust computations of the thermal profile and inverses of this function for controls use. This also allows useful initial temperature estimates for the case with counterflow in the lehr ducts, which should greatly simplify and speed the convergence of more detailed models in which the glass participates in the radiative exchanges.

INTRODUCTION

The annealing lehr is basically a large insulated enclosure through which a ribbon of flat glass passes at controlled speed (see Schematic, Fig. 1). The enclosure contains air ducts through which air flows with controlled initial temperature and flowrate from a plenum. The goal of this arrangement is to subject the ribbon to a suitable temperature history so that the exiting ribbon has a desirable residual stress distribution when it reaches room temperature.

To achieve the goal, it is necessary to select flowrates in the individual ducts as well as inflow temperatures, so that the desired temperature distribution is imposed. Either an array of sensors adequate to the characterization of the temperature distribution must be provided and maintained, or the glass temperature must be simulated in real time so that a few robust sensors can provide sufficient information for successful control. We have chosen the second approach.

Chui [1] solved for the quasisteady temperature distribution $T(x,y)$ in a glass ribbon levitating between two arrays of identical ducts. Grey-body radiative heat transfer operated between ducts and ribbon, so the temperature solution was symmetric about the $z = 0$ midplane and the $y = 0$ centerline as well. He reported numerical solutions for initial temperatures, ribbon geometry and mass flows which were typical of industrial practice. The solutions were validated in that temperature differences overall were as expected from industrial measurements in working lehrs.

Lehr Heat Exchange Schematic

coo6.plt

Air In

Plenum/Temperature Control

Upper Ducts

Flow

Glass Ribbon

Lower Ducts

Feet

Feet
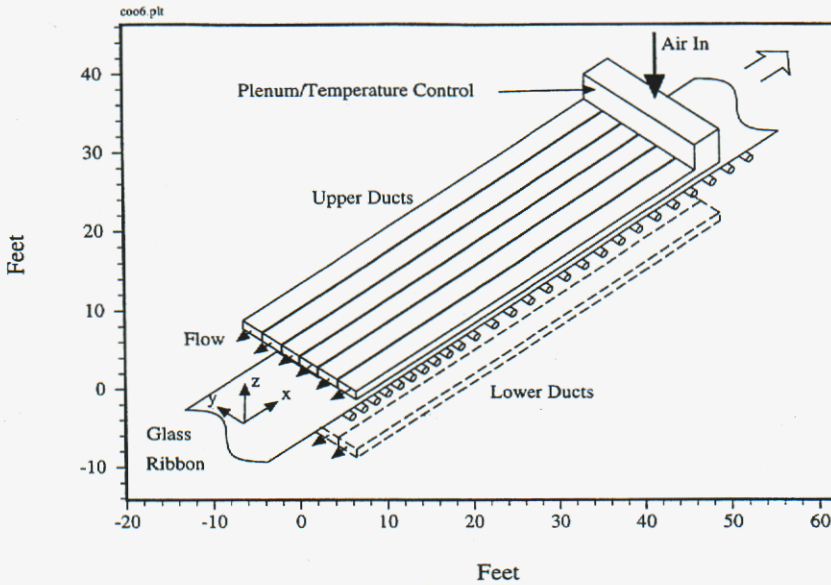
Figure 1. A glass ribbon carried on supporting rollers enters the lehr in a fluid state at a temperature around 840 K and exits below the glass transition temperature of 725 K. The complete lehr consists of three sections— conditioner, annealing section, and cooldown section, all enclosed in an insulated box. The first two sections are cooled primarily by radiative exchange with cooling air in the ducts above and below the ribbon. Airflow in the ducts can be parallel or counter to the ribbon motion which defines the positive x-direction here. Electrical heaters may also be installed between the bottom of the ducts and the ribbon to improve control.

A simplified version of the Chui model, with ribbon and ducts infinitely wide and long but only infinitesimally separated in z, is solved in closed form below. Then radiative viewfactors of realistic lehr geometries are discussed in the second section This section also covers roller radiative exchanges and thermal contact between glass ribbon and the support rollers as well. Extension to the case of radiative participation of the glass ribbon will be treated separately, see Ref. [2]. No heat conduction in glass or duct air was considered, as in Chui [1].

PLANE PARALLEL SOLUTION

Consider the case of an infinitely wide glass ribbon moving through an infinitely long and infinitely wide pair of ducts in which a fluid flows. Let the ducts be symmetric about the midplane of the ribbon, and suppose that the heat exchange is entirely by radiation between the ribbon surface and the ducts' surfaces. For steady operation of this system, the surface temperature of the glass will be $T_g(x)$, depending only on the position along the direction of motion, and, if the ducts' fluid and surface temperatures are taken to be the same, these will similarly be functions of x alone: $T_d(x)$. The energy balance for bulk temperatures can be written in terms of the ribbon mass flux per unit width times the specific heat $\dot{M}_g c_g$, that is, the heat capacity of the ribbon, simply as:

$$\dot{M}_g c_g \frac{\partial T_g}{\partial x} = -2\varepsilon_e \sigma \left(T_g{}^4 - T_d{}^4\right) \qquad [1a]$$

when the x axis is in the direction of motion of the ribbon, and the radiative flux is determined entirely by the temperatures of the duct and ribbon at station x alone—the temperature changes along ribbon and duct is ignored in computing the grey body radiation here. The "effective emissivity" ε_e is given by:

$$\varepsilon_e = \left(\frac{1}{\varepsilon_g} + \frac{1}{\varepsilon_d} - 1\right)^{-1}$$

for infinite plane-parallel grey isothermal surfaces. The fluid in the duct then obeys:

$$\pm \dot{M}_d c_d \frac{\partial T_d}{\partial x} = \varepsilon_e \sigma \left(T_g{}^4 - T_d{}^4\right) \qquad [1b]$$

where the + sign indicates fluid flowing in the same direction as the ribbon moves, while the − sign indicates counterflow. It follows immediately that the temperature gradients in glass and duct are proportional, with constant of proportionality given by the parameter a, the ratio of advected heat capacities (per unit width):

$$a = \mp (\dot{M}_g c_g)/ (2\dot{M}_d c_d)$$

This means that $T_d(x)$ can be eliminated as a first integral; in dimensionless form:

$$\theta_d = \theta_{do} + a\left(\theta - 1\right) \qquad [2a]$$

where $\theta_d = T_d(x)/T_{go}$ and $\theta = T_g(x)/T_{go}$ are dimensionless values for the absolute (K) temperatures, scaled by the initial glass ribbon temperature T_{go}. For convenience, let this be written as $\theta_d = a\theta + b$ where $b = \theta_{do} - a$ is a known constant since a and the initial duct temperature are prescribed.

An inherent length scale $\hat{L}_o$ can be defined from the data as:

$$\hat{L}_o = (\dot{M}_g c_g)/ (2\varepsilon_e \sigma T_{go}{}^3)$$

Now, the energy balance equation reduces to the ordinary differential equation

$$-\hat{L}_o \frac{d\theta}{dx} = \left(\theta^4 - [\theta_{do} + a(\theta - 1)]^4\right) = P_4\left(\theta; \theta_{do}, a\right)$$

Closed-form quadrature can be carried out on this expression; for the following two cases:

(Case 1: general solution) The result is the cumbersome but explicit form of the solution, including its initial conditions:

$$\frac{(x - x_o)}{\hat{L}_o} = \frac{1 + a^2}{2b^3} \, F(\theta, a, \theta_{do}) \qquad\qquad [2b]$$

where

$$F(\theta, a, \theta_{do}) = -\ln\left[\frac{\theta - \theta_d}{1 - \theta_{do}} \frac{1 + \theta_{do}}{\theta + \theta_d}\right]^{1/2} + \left\{\frac{1 - a^2}{1 + a^2} \tan^{-1}\left[\frac{\theta\theta_{do} - \theta_d}{\theta + \theta_{do}\theta_d}\right]\right\} +$$
$$+ \frac{a}{1 + a^2} \; \ln \frac{\left(1 + \theta_{do}^2\right)}{\left(\theta^2 + \theta_d^2\right)} \frac{\left(\theta^2 - \theta_d^2\right)}{\left(1 - \theta_{do}^2\right)}$$

The right hand side depends only on the arguments of $F(\theta, a, \theta_{do})$, because $b = \theta_{do} - a$. That is, the lehr aim point, namely, the glass temperature at the exit, has the dimensionless value θ , while the lehr control settings for (1) flow in the ducts, a, and for (2) the temperature of the duct fluid, θ_{do}, at the station x_o, are the other two arguments.

For counterflow in the ducts, a is positive; it is negative for parallel flow. In the counterflow case, the value of the dimensionless parameter θ_{do} is not usually known; rather, the temperature of the fluid at the inflow end of the duct at station x is known. If we denote the inflow temperature of the duct fluid by θ_{din} regardless of whether it occurs at station x or at station x_o, then the function $F(\theta, a, \theta_{do})$ can be written as $F(\theta, a, \theta_{din})$ with the understanding that θ_{din} means θ_{do} when a is negative, and means θ_d when a is positive.

(Case 2: b=0 in counterflow) Putting b = 0 makes the [2b] singular, but also makes the duct absolute temperature a multiple of the glass temperature, allowing a trivial quadrature:

$$x - x_o = \hat{L}_o \frac{1}{3(1 - a^4)} \left(\frac{1}{\theta^3} - 1\right) \qquad\qquad [2c]$$

Note that a cannot be unity in this case, or the duct and ribbon are at the same temperature everywhere, since $b = 0$. Further, because $b = \theta_{do} - a = 0$ here, the initial duct temperature θ_{do} is simply a.

When b is small, evaluation of [2b] by finite arithmetic is inaccurate, so it is necessary to expand the solution in powers of b. However, the most natural expansion parameter turns out to be $e = b/(1 - a^4)$ rather than simply b.

The solution given by eqs.[2] above is of the form $\ell = \hat{F}(\theta; a, \theta_{do})$ in terms of the dimensionless distance $\ell = (x - x_o)/\hat{L}_o$ as dependent variable, with independent variable being θ , and the duct settings a and θ_{do} as parameters. Since any value of θ can be used in the right hand sides of eqs.[2], the first step in evaluating the solution must be to select the physically meaningful domain of θ , for the given values of a and θ_{do}.

By inspection of eq.[2b], it is clear that $\theta = \theta_d$ and $\theta = -\theta_d$ are both singular, and produce an infinite value for ℓ. Substitution into eq.[2a] and solution result in two values: $\theta_c = \dfrac{b}{1-a}$ and $\theta_o = -\dfrac{b}{1+a}$. The the ribbon and duct temperature converge to value θ_c, given infinite length to accomplish this asymptotic behavior, as seen in Fig. 2(a) for parallel flow. The θ_o value is an asymptote approached by the glass while the duct approaches $-\theta_o$. Since one or the other of θ_o or $-\theta_o$ must be negative, this infinite length branch must be nonphysical because these are absolute temperature ratios. For positive θ_o, the solution must have been cut off when $\theta_d = 0$, at $\ell = \ell_{ext}$, an extremum of ℓ. This length corresponds to $\theta * = -\dfrac{b}{a}$. Similarly, for a negative θ_o value, the cutoff must be imposed where $\theta = 0$ (where $\theta_d = b$); in either case, ℓ_{ext} is given by:

$$\ell_{ext} = \frac{1+a^2}{2b^3} \left\{ \ln \left| \frac{1-\theta_{do}}{1+\theta_{do}} \right|^{\frac{1}{2}} + \frac{1-a^2}{1+a^2} \tan^{-1}\left(s_o \theta_{do}^{s_o}\right) + \frac{a}{1+a^2} \ln \left| \frac{1+\theta_{do}^2}{1-\theta_{do}^2} \right| \right\} \qquad [3]$$

where s_o is +1 when θ_o is positive, and is -1 when θ_o is negative, so that the argument of the arctan is θ_{do} and $-1/\theta_{do}$ respectively in these cases. The physical solution branch can now be fully characterized by analysis of the relative sizes of $\theta_c, \theta_o, \theta *$ in relation to 0, 1, and θ_{do} values.

To compare to Chui's numerical solutions for the variation of temperature with distance requires a function $\theta = f(\ell; a, \theta_{do})$, that is, the inverse of the function $\hat{F}(\theta; a, \theta_{do})$. This is numerically evaluated by bisection to locate the appropriate value of ℓ for the given a and θ_{do}. Results using input parameters derived from Chui[1], are shown in Fig. 2 below, for both parallel and counterflow in the ducts. The excellent agreement was obtained by using $\hat{L}_o = 66.7$ m instead of the value 29.85 m which his parameters would have predicted; see the Discussion section below.

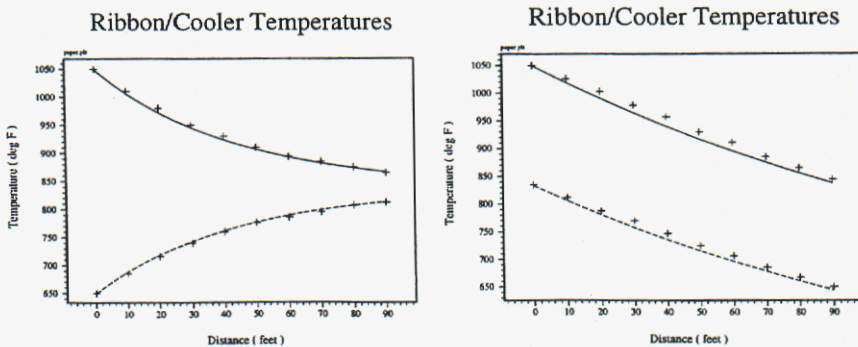| Ribbon/Cooler Temperatures | Ribbon/Cooler Temperatures |

Figure 2. (a, to left) Duct flow is parallel to the glass ribbon motion, and duct fluid is cooling the glass. Parameters (a, θ_{do}) are taken from Ref.[1], Fig. 8(A) (plot symbols +), but $\hat{L}_o$ is the best fit of the closed form solution (continuous curves). (b, to right) Counterflow solution for same parameters, Fig. 8(B) of Ref.[1].
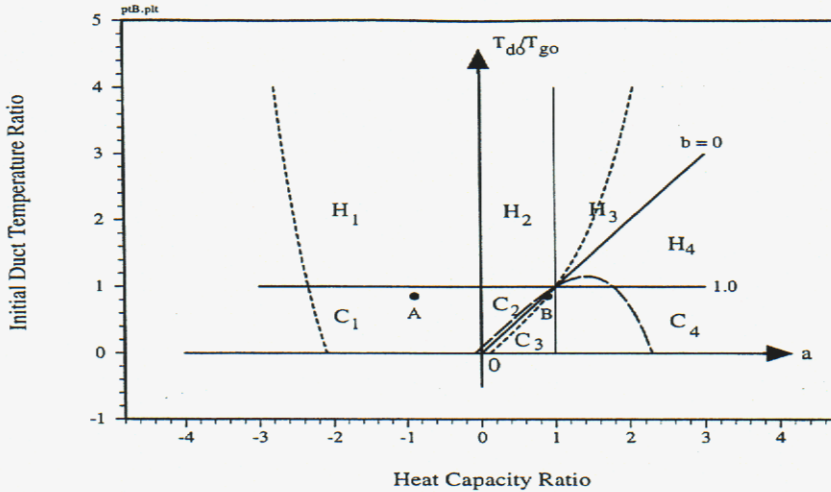
General Classification of Lehr Solutions

Figure 3. Subdomains of the (a, θ_{do}) plane with distinct solution types for plane parallel infinite glass ribbons and duct surfaces. Chui solutions in Figs. 2 (a) and (b) correspond to the points A,B with the filled circle plot symbols. All solutions with $\theta_{do} > 1$ have ducts heating the glass, and are labelled "H"; those with $\theta_{do} < 1$ are glass cooling, "C". In each subdomain, the order of the glass temperature values θ given as θ_o, θ_c are different and are in different orders relative to 0, 1 or θ_{do}. Asymptotic form eq. [2c] is used between the dashed curves, which includes all weak duct flow cases (large | a |); values depicted are $e_{min} = -0.115$ and $e_{max} = 0.086$. The infinite duct capacity solution [2d] applies to all points along the vertical axis.

The (a, θ_{do}) plane of Fig. 3 further subdivides because the parameter $b = \theta_{do} - a$ introduced in eq.[2a] vanishes on the 45-degree line through the origin; b is positive above and to the left of this line. Near this line, the power series with leading term eq.[2c] is evaluated whenever (a, θ_{do}) lies between the broken curves which converge at (1,1); outside this region, eq.[2b] is evaluated directly to determine ℓ. At these dashed curves, numerically evaluated ℓ may be discontinuous because of this switch between [2b] and [2c].

In summary, the solutions given in eqs. [2] have physically meaningful values when the glass temperature aim point θ is between unity and θ_c for the regions C1,C2, H1 and H2; for C3 and C4, θ must lie between $\theta* = -\dfrac{b}{a}$ and unity, while H3 and H4 can take on any θ value from unity to infinity.

FINITE WIDTH, LENGTH and HEADROOM

The 'infinitely wide' approximation treated in the previous section, and that the flux can be computed from $\left(T_g^{\,4} - T_d^{\,4}\right)$ evaluated only at x, would both be true if the headroom between ribbon and ducts were zero. Lehr designs approach this ideal situation by using low headroom, well-insulated sidewalls, etc. However, finite headroom means that viewfactors of the duct surfaces to

the side and along the axis are between 0 and 1, which motivated the numerical work by Chui [1] and later by Gardon [3]. The ability of the appoximation to reproduce the numerical solutions can be understood by considering the effect of axial temperature variations quantitatively.

Expanding the ribbon temperature $T_g(x)$ as a Taylor series about x_1 and raising it to the fourth power introduces a factor:

$$1 + \left[2\frac{\partial^2 T_g}{T_g \partial x^2} + 6\left(\frac{\partial T_g}{T_g \partial x}\right)^2\right](x-x_1)^2 + ...$$

into the integrand for the flux at a given point on the duct surface. The odd powers of $(x-x_1)$ are omitted since they will not contribute to an integral with symmetric limits. Evaluating the square bracket term at the axial midpoint of the solution shown in Fig. 2 indicates that its magnitude is about 0.023, so neglect of axial temperature variations should not introduce larger errors. This same expression can be used as an a posteriori error estimate when applying eqs. [2].

Because the practical control problem includes maintaining a desired centerline-to-edge temperature profile on the ribbon, the ducts are operated at different temperatures, and their finite widths must be taken into account when computing viewfactors. Fortunately, the lehr is predominately made up of plane elements, so its walls, ends, and ducts can all be represented as planar rectangles arranged so as to make up the enclosure.(Fig. 1). Therefore, the ability to calculate the viewfactors of two rectangles at arbitrary distance and arbitrary orientation to each other is the most difficult calculation required. This can be carried out in closed form by application of 'viewfactor algebra' relations, Ref. [4].

If rollers are included in the radiative calculation, consistency demands that they be given contact conductive boundary conditions as well. However, the possible conditions of contact are so varied that there is no unique model for this effect. Here, we expect to parameterize the contact, compare simulated surface temperatures of the ribbon to measured values, and fix the model parameters for the industrial site at which the lehr models are to be applied, Ref. [5].

HEAT TRANSFER WITHIN THE RIBBON

The heat transfer effects discussed above include only radiative transfer at the surface of the ribbon, and at the surface of the duct. This presumes the glass is isothermal through the actual ribbon thickness t_g; because it is moving at velocity V_g which has a typical Peclet number based on thickness of 10, the through-thickness temperature profile is determined; Ref. [6]. However, at lehr temperatures, the blackbody spectrum contains a significant fraction of its energy in the wavelengths at which glass is semitransparent, so the glass should be treated as a participating medium; Ref. [2].

DISCUSSION

At this point, the elements of a simple quasisteady model of the radiative energy exchange between the ribbon and enclosure elements has been presented and comparied with Chui's results, Ref. [1]. That comparison, it must be stressed, used a fitted value of the length scale $\hat{L}_o$, namely, 66.7 m instead of the value 29.85 m = $\hat{L}_o = (\dot{M}_g c_g)/(2\varepsilon_e \sigma T_{go}^3)$ using the values in his Table I. This is a multiplier of 2.2, which suggests that perhaps the factor 2 in his eq.[1] was omitted from the numerical calculations he reported. Similarly, Chui's Fig.9 "centerline " case can be approximated

by Eqs. [2] with input a = 0.8943, θ =0.8678 (850 deg F exit glass temperature), and ℓ_{oa} =90 ft (27.4 m)/ $\hat{L}_o$; the returned duct input temperature is θ_{din} =0.7426 (676 deg F) with θ_{din} =0.8707 (855 deg F). This is true so long as the $\hat{L}_o$ value fitted in Fig. 2(a) is used. The fact that both his Fig. 8(B) and Fig.9 results are essentially reproduced with $\hat{L}_o$ =66.7 m reinforces the likelihood that this value was misreported in Ref. [1].

The plane parallel thermal solution should prove useful in several applications, including realtime control and automated meshing of numerical computations for the whole enclosure. In numerical use, it would also generate an approximate initial solution for counterflow, to minimize the number of times it would be necessary to iterate a "shooting" boundary value problem solver.

In real time control, the controller will change settings at some time interval Δt. During that time, the ribbon will have advanced by $V_g \Delta t$, which can only be useful control when this distance is less than the distance between sensor and actuator . Typically, V_g = 0.2 m/sec, so a useful solution must be computationally fast.

The actual goal of the lehr is to manage stresses, and so the complete model based control would connect the lehr settings with the residual stresses in the glass as it reaches the cutting station. Simulation of the stresses due to thermal strains can be done in a "Strength of Materials" sense by use of one-dimensional calculations of fiber strains as outlined in Ref. [7].

REFERENCES:

1. Chui, G,K., "Heat Transfer and Temperature Control in an Annealing Lehr for Float Glass", *J. Amer. Ceram. Soc. 60*, 477. (1977)

2. Houf, W. ,"Lagrangian Thermal Model of Annealing Lehr Glass Ribbon as Radiatively Participating Medium (Tentative Title)". To appear, Sandia National Laboratories. (2001)

3. Gardon, R. "Modelling Annealing Lehrs for Flat Glass", *J. Amer. Ceram. Soc. 65*,372. (1982)

4. Brewster, M.Q., *Thermal Radiative Transfer and Properties*, John Wiley & Sons, New York (1991)

5. Bertram, L. A., "Elements for Real Time Steady Simulation for Flat Glass Lehr Control" *SAND2001-8001*, Sandia National Laboratories. (2001)

6. Adams, LH and Williamson, ED, "Annealing of Glass", *J. Franklin Inst. 190*, 597-631 and 835-870. (1920)

7. Gardon, R and Narayanaswamy, OS, "Stress and Volume Relaxation in Annealing Flat Glass", *J. Amer. Ceram. Soc. 53*, 380. (1970)

Intentional Left Blank

Appendix B

TEST PLAN FOR THE NO$_X$ CONTROL EXPERIMENTS

Robert G. Hillaire, * *Yu Jiao,† David Hanekamp,† and John J. Connors†*

**Sandia National Laboratories*
Livermore, CA

†Glass Technology Center
PPG Industries, Inc., Pittsburgh, PA

1. Furnace Off Control Test (Cap Test, Open-Loop Benchmark)

This test will indicate the amount of variance we can expect in NO$_X$ production when not changing any process controls. We simply set the process controls at constant values and monitor the process for several cycles.

- Experiment setup:
    - NO$_X$ loop off, Crown temperature loop off, Air/Gas ratio at a fixed setpoint
- Test duration:
    - Two hours
- Measurements:
    - NO$_X$ measurement
    - Crown temperatures (All crowns)
    - Regenerator temperatures (Rider Arch and Regenerator crowns)
    - Combustion air flow
    - Individual port gas flow
    - Melter pressure
    - Actual Combustion actual air flow and gas flow

2. NO$_x$ Source Identification Test

The objective of this test is to identify sources of NO$_x$ production and its relationship among other measured process variables. The hypothesis of this test is that the main source of the NO$_x$ generated in the 14-2 furnace is from improper fuel distribution and the majority of the NO$_x$ is generated in the down-tank area of the furnace. To verify this hypothesis and identify potential gas distribution improvements, we would conduct the following test:

- Experiment procedure:
    - Beginning on the downstream port on the left side, reduce the gas flow 4000 cfh on each port, one port at a time, for one firing cycle.
    - Wait several firing cycles after completing each port before moving upstream to the next port.
    - Complete all of the left ports before moving to the right side ports.
    - The experiment should be conducted twice: once while producing GL20 and once on any other product.
- Experiment setup:
    - NO$_x$ loop off control, crown temperature loop off control
    - Fixed combustion air flow (Total gas flow will change because of the port gas reduction)
- Measurements:
    - NO$_x$ sensor, Crown temperatures (All crowns), Combustion air flow, Port gas flows, Melter pressure, Regenerator temperatures, Existing Oxygen sensors, ENERAC measurement at the center of connecting flue for NO$_x$ and other parameters
- Duration:
    - Two days, one day for each side.

3. Existing NO$_X$ control loop magnitude test (static test) (zeroth order test)

The objective of this test is to verify the magnitude of NO$_X$ production related to the current NO$_X$ control scheme for the purpose of future improvements to the NO$_X$ control loop. This test will show how NO$_X$ is affected by a static change in the control value. We will also be able to determine to what extent the control setting from the previous firing cycle and the previous reversal has on NO$_X$ production. The prescribed firing order will allow us to determine the affects of the previous cycle and the preceding two cycles in several combinations. The duration of the test is sufficiently long so that parasitic perturbations in the process may be filtered out of the results.

- Experiment procedure
  - Alternate the NO$_X$ control loop's output in a predefined pattern as follows:

Firing Cycle	Left Control Effort (%)	Right Control Effort (%)
1	0	0
2	100	0
3	0	100
4	100	100
5	0	0
6	100	0
7	0	100
8	100	100
9	0	0
10	100	0
11	0	100
12	100	100

  - Maintain a constant control value for the entire firing cycle. Each firing cycle will have either a "high" setting or "low" setting in a prescribed order. The prescribed order will exercise several combinations that change the previous cycle conditions.
- Experiment setup:
  - NO$_X$ loop in Manual, Crown temperature loop off control (Fixed total gas flow
- Measurements:
  - NO$_X$ sensor, Crown temperatures, Combustion air flow, Total gas flow, Regenerator temperatures, Melter pressure
- Duration:
  - One firing cycle per step. Entire experiment will take about 6 hours.

4. NO$_X$ Control Trend Test (first order test, reaction curve)

The objective of this test is to verify the controllability of NO$_X$ using the current control scheme. The test will determine if there are "irrevocable" process characteristics that cannot be manipulated once the firing sequence has begun (i.e. once NO$_X$ production passes a certain level, it will not come back down during this cycle regardless of the changes in control). The test sequence also exposes any non-linear effects in NO$_X$ production. The prescribed cycles will exercise several combinations of conditions to expose not only the single cycle conditions, but also whether the previous cycle firing conditions affect NO$_X$ production.

- Experiment procedure:
    - The control setting for each firing cycle will be either "high" or "low" at the beginning of the cycle, then at the halfway point, the control setting will be changed to its complement.
    - Change the NO$_X$ control loop's output in a predefined pattern as follows:

Firing Cycle	Left Control Effort (%)	Right Control Effort (%)
0-½	50	0
½-1	50	100
1-1½	50	0
1½-2	50	100
2-2 ½	50	100
2½-3	50	0
3-3 ½	50	100
3½-4	50	0
4-4 ½	50	0
4½-5	50	100
5-5½	50	100
5½-6	50	0
6-6 ½	50	0
6½-7	50	100
7-7 ½	50	100
7½-8	50	0

Firing Cycle	Left Control Effort (%)	Right Control Effort (%)
0-½	0	50
½-1	100	50
1-1½	0	50
1½-2	100	50
2-2 ½	100	50
2½-3	0	50
3-3 ½	100	50
3½-4	0	50
4-4 ½	0	50
4½-5	100	50
5-5½	100	50
5½-6	0	50
6-6 ½	0	50
6½-7	100	50
7-7 ½	100	50
7½-8	0	50

- Experiment setup:
    - Crown temperature loop in Auto, Melter pressure loop in Auto
- Measurements:
    - NO$_X$ sensor, Crown temperatures, Combustion air flow, Total gas flow, Regenerator temperatures, Melter pressure
- Duration:
    - The length of experiment will be a total of 32 firing cycles, about 8 hours.

Appendix C

FULL FURNACE SIMULATION RESULTS:
Comparison of Oxygen Mole Fractions at the Glass Surface and Crown

Padmabhushana R. Desam and Philip J. Smith
Combustion and Reaction Simulations (CRSIM) Research Group
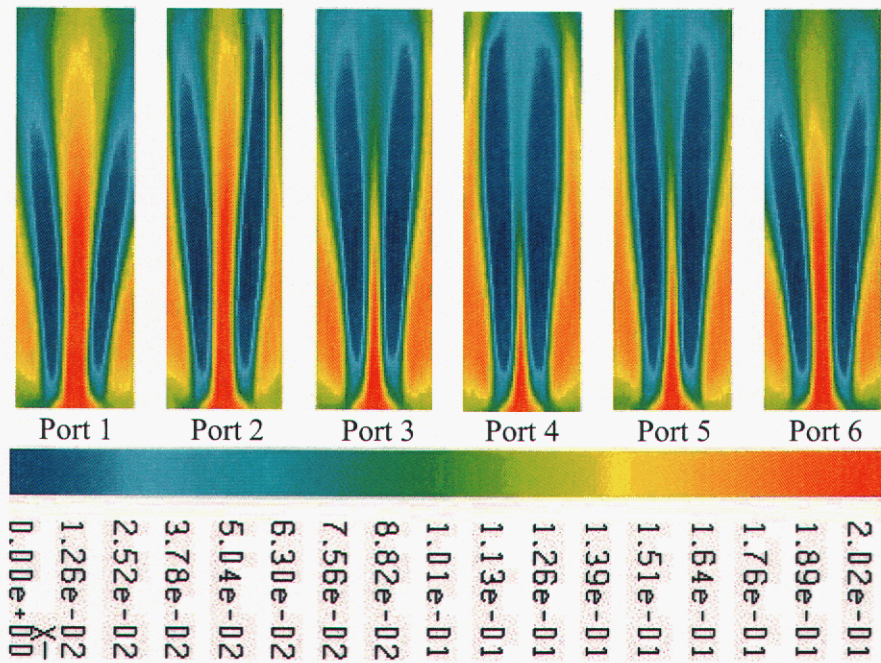*The University of Utah, Salt Lake City, UT*

Figure C-1. Mole fractions of oxygen at the glass surface from the full furnace model.
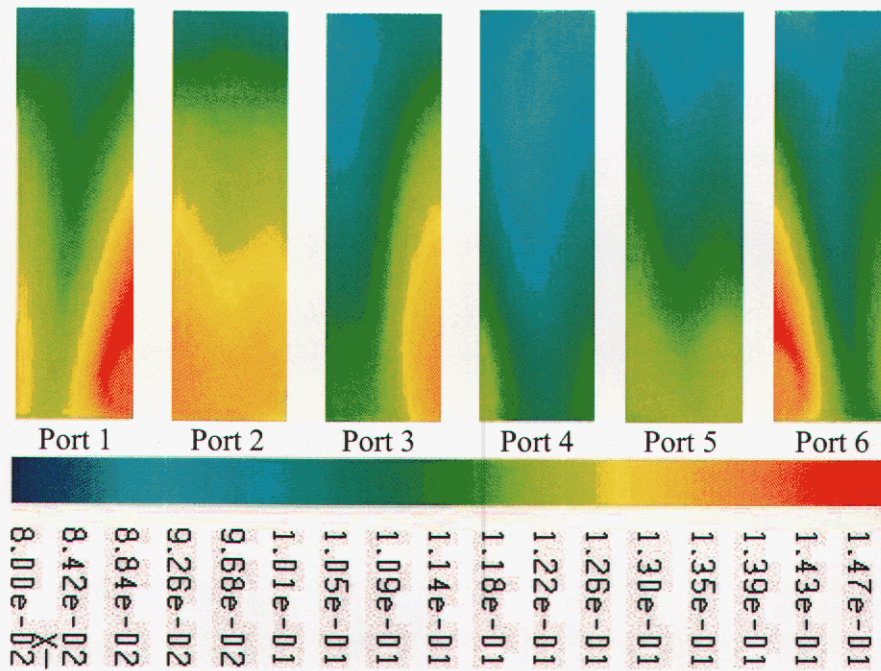
Figure C-2. Mole fractions of oxygen at the crown from the full furnace model.

Table C-1. Mole fractions of oxygen from the full furnace model.

Oxygen levels	Port 1	Port 2	Port 3	Port 4	Port 5	Port 6
Crown Average	0.1263	0.1283	0.1180	0.1074	0.1160	0.1192
Glass Average	0.1097	0.1089	0.1044	0.1019	0.0995	0.1037
Crown Center[a]	0.1166	0.1249	0.1148	0.0970	0.1100	0.1068
Glass Center[b]	0.1939	0.1962	0.1457	0.0800	0.1312	0.1783

a. Crown center: value at the geometrical center of the crown for the particular port.
b. Glass center: value at the geometrical center of the glass surface for the particular port.

Distribution:

Gideon M. Varga
Elliott P. Levine

U.S. Department of Energy
EE-2F
1000 Independence Ave, SW
Washington, DC 20585

Mehran Arbab
John J. Connors
David Hanekamp
Kevin Hill
Yu Jiao
Kwaku K. Koram
Raymond M. Mayer
Rajiv Tiwary

PPG Industries, Inc.
Glass Technology Center
Guys Run Road
Harmar Township, PA 15238-1305

Bruce W. Binion
Mark A. DeYoung
Craig Dodge
Alan J. Miller

PPG Industries, Inc.
Works No. 14
P.O. Box R
Elwin - Mt. Zion Road
Mt. Zion, IL 62549

Arthur R. Farrar
William F. Haley

PPG Industries, Inc.
Works No. 4
7400 Central Freeway North
Wichita Falls, TX 76305-6656

Craig P. Gowin
PPG Industries, Inc.
1020 Olympic Drive
Batavia, IL 60510-1329

John F. McConnell
JFM Consulting, Inc.
20 Perity Lane
Pittsburgh, PA 15220

Richard W. Michael
PPG Industries, Inc.
120 Otis Drive
Lincoln, AL 35096

Peter M. Walsh (3 copies)
University of Alabama at Birmingham Department
of Mechanical Engineering
BEC 257
1530 3rd Avenue South
Birmingham, AL 35294-4461

Padmabhushana R. Desam
Philip J. Smith

University of Utah
380 Intermountain Network and Scientific
Computing Center
Salt Lake City, UT 84112

Central Technical Files, MS 9018 3 copies

Technical Library, MS 0899

Classification Office, MS 9021

Willard R. Bolton, Jr., Org. 8116, MS 9104

Robert J. Gallagher, Org. 08367, MS 9052

Donald R. Hardesty, Org. 08360, MS 9054

Robert G. Hillaire, Org. 08116, MS 9104

William G. Houf, Org. 08752, MS 9042

Jay O. Keller, Org. 08367, MS 9052

William J. McLean, Org.08300, MS 9054

Christopher D. Moen, Org.08752, MS 9042

Donald A. Sheaffer, Jr., Org. 08235, MS 9102

James C. F. Wang, Org. 08773, MS 9403